

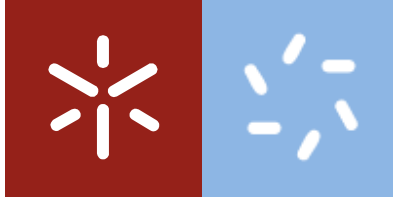


SEARCH FOR VECTOR-LIKE QUARKS WITH THE ATLAS EXPERIMENT

Tiago Dias do Vale

Universidade do Minho
Escola de Ciências





Universidade do Minho

Escola de Ciências

Tiago Dias do Vale

**SEARCH FOR VECTOR-LIKE QUARKS WITH THE
ATLAS EXPERIMENT**

Dissertação de Mestrado
Mestrado em Física - Física Aplicada

Trabalho efetuado sob a orientação do
Professor Doutor Nuno Filipe da Silva Fernandes de Castro

DECLARAÇÃO

Nome: Tiago Dias do Vale

E-mail: tiago.vale@cern.ch

Telefone: +351964946489

Número de Cartão de Cidadão: 14020611

Título da Tese: Search for vector-like quarks with the ATLAS experiment

Orientador: Doutor Nuno Filipe da Silva Fernandes de Castro

Ano de Conclusão: 2016

Designação do Mestrado: Mestrado em Física Aplicada

É AUTORIZADA A REPRODUÇÃO INTEGRAL DESTA TESE APENAS PARA EFEITOS DE INVESTIGAÇÃO, MEDIANTE DECLARAÇÃO ESCRITA DO INTERESSADO, QUE A TAL SE COMPROMETE;

Universidade do Minho, 29/08/2016

Assinatura:

Tiago Dias do Vale

SEARCH FOR VECTOR-LIKE QUARKS WITH THE
ATLAS EXPERIMENT

Tese de Mestrado
Mestrado em Física - Física Aplicada

Trabalho efectuado sob orientação do
Professor Doutor Nuno Filipe da Silva Fernandes de Castro

Agosto de 2016

Acknowledgments

There is a big number of people to which I owe my gratitude for all the support and for all the knowledge they shared with me.

I would like to start by thanking Nuno Castro, not only for his supervision, but also for the opportunities he gave me throughout this time. It was a pleasure to which I will always be thankful.

My closest colleagues in the LIP-Minho team are a great part of this work. Thank you Juanpe for all the help you gave me through the whole year, and for teaching me so much about programming and all that goes with it. Thank you Ana and Zé for all the moments we shared and for always supporting each other.

I also thank the whole LIP team, and the Portuguese ATLAS team in particular, as well as the Heavy Quarks and Tops ATLAS subgroup. I want to thank the Z-tag team, the TU Dortmund group in particular for their hospitality, and a special thanks to Johannes Erdmann, for being so helpful the whole time.

Thank you mother and father for all your love and support. Thank you for making all of this possible. Thank you Ana for being there. Thank you for every single thing that I can not even begin to enumerate. We both know things would be much darker if it wasn't for you.

I thank LIP (Laboratório de Instrumentação e física experimental de Partículas), FCT/MEC (Fundação Ciência e Tecnologia / Ministério da Educação e da Ciência), FEDER (Fundo Europeu de Desenvolvimento Regional) for funding my activities this past year, as established by the partnership PT2020 partnership with COMPETE2020 (Autoridade de Gestão do Programa Operacional Competitividade e Internacionalização), by providing me with a research scholarship (Reference LIP/BI - 25/2015).

FCT

Fundação para a Ciência e a Tecnologia
MINISTÉRIO DA CIÊNCIA, TECNOLOGIA E ENSINO SUPERIOR



Abstract

In the present thesis, data originated from proton-proton collisions at the Large Hadron Collider and collected by the ATLAS experiment in 2015 was used for the search of pair-produced vector-like quarks T and B decaying to a Z boson and a third generation quark, focusing on the dilepton channel.

A strategy built upon the 8 TeV analysis was further developed. Control regions were defined in order to model the Monte Carlo simulation of the background. The data in the considered signal region is not yet unblinded by the ATLAS collaboration and, therefore, the expected sensitivity of the search was evaluated using pseudo-data built under the background only hypothesis. The vector-like B has 95% confidence level expected mass limits of 766 GeV for the singlet hypothesis and 873 GeV for the doublet hypothesis. The vector-like T singlet and doublet hypotheses have expected limits of 687 GeV and 797 GeV, respectively, representing an encouraging improvement with respect to the currently published mass limits.

This text is complementary to the dilepton boosted topology analysis being developed by a group at the TU Dortmund, Germany, and the trilepton channel being developed by a group at the University of Arizona, USA. Orthogonality between the analysis presented in the present thesis and the trilepton analysis is ensured by definition, but with the boosted topology analysis it has to be constructed. The first steps in that direction are described at the end of this text, based on the multiplicity of large-R jets.

Resumo

Nesta tese, dados originados em colisões de próton-próton no Large Hadron Collider e coletados pela experiência ATLAS em 2015 foram usados para a pesquisa de quarks vetoriais T e B , produzidos em pares, decaindo para um bóson Z e um quark de terceira geração, com foco no canal dileptónico.

Um estratégia construída a partir da análise a 8 TeV foi desenvolvida. Regiões de controlo foram definidas, por forma a modular a simulação de Monte Carlo do fundo. Os dados na região de sinal considerada ainda estão ocultados pela colaboração de ATLAS, e, portanto, a sensibilidade esperada para esta pesquisa foi avaliada usando pseudo-dados gerados a partir da hipótese da existência de apenas fundo. O quark vectorial B , num limite de confiança de 95%, tem limites esperados de 766 GeV para o caso em que é singleto, e 873 GeV para doubleto. O quark vectorial T , singleto e doubleto, têm limites esperados de 687 GeV e 797 GeV, respectivamente, o que representa uma melhoria encorajadora em relação aos limites de massa atualmente publicados.

Esta tese é complementar com a topologia dileptónica *boosted* que está a ser desenvolvida por um grupo na TU Dortmund, Alemanha, e com o canal trileptónico, que está a ser desenvolvido por um grupo na Universidade do Arizona, EUA. A ortogonalidade entre a análise aqui apresentada e a análise trileptónica está assegurada por definição, mas no caso da topologia *boosted* esta tem de ser construída. Os primeiros passos nessa direcção são descritos no final deste texto, com base na multiplicidade de jatos com largo raio.

Contents

1	Introduction	1
2	Theoretical Overview	3
2.1	The Standard Model	3
2.1.1	Quantum Electrodynamics	5
2.1.2	Quantum Chromodynamics	6
2.1.3	Electroweak Interactions	7
2.1.4	The Brout-Englert-Higgs Mechanism	9
2.1.5	Experimental Tests and Limitations	12
2.2	Vector Like Quarks	14
2.2.1	Motivation	14
2.2.2	Phenomenology	15
3	Experimental Setup	21
3.1	The LHC	21
3.2	The ATLAS Detector	23
3.2.1	Inner Detector	24
3.2.2	Calorimeter System	26
3.2.3	Muon Spectrometer	28
3.2.4	Magnetic System	29
3.2.5	Trigger and Data Acquisition	30
4	Search for Vector Like Quarks	33
4.1	Samples	34

4.1.1	Signal Samples	34
4.1.2	Background Samples	34
4.2	Analysis Strategy	35
4.2.1	Objects Definition	35
4.2.2	Signal Region Selection	38
4.2.3	Selection Optimization	43
4.2.4	Control Regions Definition	47
4.3	Results	63
4.4	Complementarity with boosted topologies and trilepton channel	74
5	Conclusions	77

List of Figures

2.1	The Brout-Englert-Higgs potential.	10
2.2	Data/theory ratio of several SM cross section measurements. .	13
2.3	Cross section of hadron production for two, three and four neu- trino families.	14
2.4	Feynman diagram examples for single and pair produced VLQ.	16
2.5	VLQ production cross-section as a function of the mass.	17
2.6	Branching Ratio as a function of the VLQ mass.	17
2.7	Mass of the Zb system for singlet and doublet hypotheses. . .	18
2.8	Summary of pair produced VLQ mass limits.	19
3.1	Schematic representation of the different LHC accelerators. .	22
3.2	Cut-away view of the ATLAS detector layout.	23
3.3	Schematic representation of the ATLAS Inner Detector.	25
3.4	Schematic view of the ATLAS Calorimeter System.	27
3.5	Schematic representation of the ATLAS Muon Spectrometer. .	29
3.6	Cumulative luminosity versus time delivered by the ATLAS detector.	32
4.1	b -tagging efficiency of the mv2c20 tagging algorithm as a func- tion of jet p_T	36
4.2	Multiplicity of leptons and b -tagged jets, p_T of Z candidate and H_T of jets.	39

4.3	The mass of the Zb system with distributions normalized to unity is shown. At least 2 jets and a pair of OS-SF leptons were required.	41
4.4	Distribution of leading and sub-leading jets p_T	42
4.5	The distribution of leading and sub-leading leptons p_T	43
4.6	Distribution of leading and sub-leading jets η	44
4.7	Distribution of leading and sub-leading leptons η	45
4.8	Distribution of leading and sub-leading jets ϕ	46
4.9	Distribution of leading and sub-leading leptons ϕ	47
4.10	Mass of the Z boson candidate inside and outside the resonance.	48
4.11	Distribution of Z candidate p_T and H_T of jets.	49
4.12	Mass of the Zb system.	50
4.13	Expected mass limits for each pair of Z candidate p_T and H_T of jets cuts.	51
4.14	Multiplicity of jets and b -tagged jets in the $t\bar{t}$ control region.	53
4.15	Leading and sub-leading jets p_T in the $t\bar{t}$ control region.	54
4.16	Leading and sub-leading leptons p_T in the $t\bar{t}$ control region.	55
4.17	Leading and sub-leading jets η in the $t\bar{t}$ control region.	56
4.18	Leading and sub-leading leptons η in the $t\bar{t}$ control region.	57
4.19	Leading and sub-leading jets ϕ in the $t\bar{t}$ control region.	58
4.20	Leading and sub-leading leptons ϕ in the $t\bar{t}$ control region.	59
4.21	Mass of the Zb system in the $t\bar{t}$ control region.	60
4.22	Mass of the Z candidate outside the resonance.	60
4.23	Missing Transverse Energy in the $Z + bb$ control region.	61
4.24	ΔR between Z candidate leptons before and after a boost to the Z candidate center of mass.	62
4.25	Multiplicity of jets and b -tagged jets in the $Z + bb$ control region.	63
4.26	Leading and sub-leading jets p_T in the $Z + bb$ control region.	64
4.27	Leading and sub-leading leptons p_T in the $Z + bb$ control region.	65
4.28	Leading and sub-leading jets η in the $Z + bb$ control region.	66
4.29	Leading and sub-leading leptons η in the $Z + bb$ control region.	67

4.30	Leading and sub-leading jets ϕ in the $Z + bb$ control region. . .	68
4.31	Leading and sub-leading leptons η in the $Z + bb$ control region.	69
4.32	Mass of the Z candidate in the $Z + bb$ control region.	70
4.33	Mass of the Zb in the $Z + bb$ control region.	70
4.34	m_{V2c20} distribution for the leading and sub-leading jets. . . .	71
4.35	Expected VLQ mass limits at 95% CL for the singlet and doublet hypotheses.	72
4.36	Expected mass limits as a function of the W and H BR, at 95% CL.	73
4.37	Multiplicity of large-R jets in the signal region.	74
5.1	Cumulative luminosity by the day delivered to the ATLAS detector.	79

List of Tables

2.1	SM particle generations, with their masses and electric charges, weak isospin and hypercharge (defined in Section 2.1.3). Values collected from Particle Data Group. [1]	4
2.2	SM gauge bosons with their masses and electric charges. Values collected from Particle Data Group. [1]	4
2.3	VLQ multiplets allowed by SM symmetries.	16
4.1	Signal region selection.	48
4.2	$t\bar{t}$ control region selection.	50
4.3	Yields for $t\bar{t}$ control region after all the selection is applied. Uncertainties are statistics only.	52
4.4	$Z + b\bar{b}$ control region selection.	53
4.5	Yields for $Z + bb$ control region after all the selection is applied. Uncertainties are statistics only.	61
4.6	Expected mass limits at 95% C.L. for vector-like T and B , for the singlet and doublet hypothesis, comparing current results with results from the first phase of operation of the LHC. . . .	71
4.7	Expected mass limits for the different large-R jet multiplicities and p_T thresholds. For each p_T threshold, limits with exactly 0 large-R jets is on the left and less than 2 on the right.	75

Glossary

ALICE A Large Ion Collider Experiment. vii, 19

ATLAS A Toroidal LHC ApparatuS. vii, 19, 21, 26

BEH Mechanism Brout-Englert-Higgs Mechanism. vii, 15

BR Branching Ratio. vii, 17, 18, 31, 32

CERN European Organization for Nuclear Research. vii, 19, 28

CMS Compact Muon Solenoid. vii, 19

CS Calorimeter System. vii, 24, 25, 28

FCNC Flavor-Changing Neutral Currents. vii, 15

HLT High Level Trigger. vii, 28, 33

ID Inner Detector. vii, 22, 23, 27, 34

LHC Large Hadron Collider. vii, 19–21

LHCb Large Hadron Collider beauty. vii, 19

MC Monte Carlo. vii, 29, 33, 37, 39, 42, 51

. vii, 28, 45

MS Muon Spectrometer. vii, 26–28, 34

OS-SF Opposite Sign, Same Flavor. iv, vii, 31, 35, 40, 41, 43, 44

QCD Quantum Chromodynamics. vii, 4, 7, 12, 15

QED Quantum Electrodynamics. vii, 5, 6, 24

SM Standard Model of Particle Physics. vii, 3, 4, 8, 11–16

VLQ Vector-Like Quarks. vii, 13, 15–18, 31, 32, 35–38, 53

WLCG Worldwide LHC Computing Grid. vii, 28, 29

Chapter 1

Introduction

Particle Physics studies the fundamental particles and its interactions. The understanding of Particle Physics is summed up in the Standard Model of Particle Physics (SM), that is shortly outlined in Section 2.1 of this text. This model is able to describe fundamental particles and its interactions in good agreement with experimental data, but it leaves many unanswered questions. To tackle these issues, many models were theorized, and in some of these models, Vector-Like Quarks (VLQ) are predicted. These new heavy quarks are described in this text in Section 2.2.

In order to test the SM and to probe the new physics needed to answer these open questions, experiments are built. These experiments generally consist of particle accelerators, in which these particles collide so that high energies are reached and data from these collisions can be studied. The Large Hadron Collider (LHC) is the biggest particle accelerator ever built, in which particles collide at record breaking energies. This data is collected by four detectors: Large Hadron Collider beauty (LHCb) and A Large Ion Collider Experiment (ALICE), with specific purposes; Compact Muon Solenoid (CMS) and A Toroidal LHC ApparatuS (ATLAS), two general purpose detectors. Data collected from the ATLAS experiment is used in this text. The LHC and ATLAS are described in Chapter 3.

With the data collected, a search for VLQ was made. This search is de-

scribed in Chapter 4 of this text. The samples used in the present thesis are described in Section 4.1, and with them a strategy was defined. All the steps taken to arrive at the search strategy are detailed in Section 4.2. These include the definition of the objects used in this analysis, the selection that makes the signal region and its optimization, and the analogous for control regions, in order to better study the backgrounds of this analysis. After that, the results obtained are presented in Section 4.3. In it, the expected mass limits obtained are presented, as well as how they were calculated. This chapter ends with a description of how this analysis fits with other complementary analysis in this search. This is done in Section 4.4.

It is important to state that at the time this text was written, this analysis was still blinded, i.e. all data in the signal region is not presented, in order to avoid any bias that may arise (a more lengthy description of the ATLAS blinding policy is done in Subsection 4.2.2). Most of the steps needed to unblind the analysis and obtain results with the data collected, in order to know if an excess from the SM expectation is found, are included in this text. The definition of the analysis strategy, built upon what was done at the first phase of operation of the LHC; the optimization of signal and control regions, in order to make sure the Monte Carlo (MC) correctly models the background; the assembly of the limit setting machinery; the complementation with the other topologies are the basis of this text.

Chapter 2

Theoretical Overview

2.1 The Standard Model

The SM is our best attempt of describing Nature at the most fundamental level. It tells us that there is three known generations of matter particles, which interact with each other via three¹ interactions mediated by gauge bosons. These matter particles are called fermions, particles with spin 1/2, and are divided by quarks and leptons. Leptons only interact via electroweak forces, but quarks are affected by strong interactions as well. Quarks are further subdivided by their electric charge, as the up type quarks (up, charm and top) have $2/3$ of the positron charge (e), and the down type (down, strange and bottom) quarks have charge $-1/3e$. Leptons are also divided by those with electric charge (electron, muon and tau) and their neutral counterparts, the neutrinos. All these particles, with their respective masses and electric charges, are described in Table 2.1.

¹Gravity is the known fourth interaction, but, as it is several orders of magnitude weaker than the other interactions, it doesn't influence the structure of matter. It is not regarded in the SM as there is not yet a satisfactory quantum field theory description of gravity.

1st Generation	2nd Generation	3rd Generation	Charge	I_W^3	Y			
$\begin{pmatrix} u \\ d \end{pmatrix}$	2.3 MeV 4.8 MeV	$\begin{pmatrix} c \\ s \end{pmatrix}$	1.3 GeV 95 MeV	$\begin{pmatrix} t \\ b \end{pmatrix}$	173.1 GeV 4.7 GeV	+2/3e -1/3e	1/2 -1/2	1/3 1/3
$\begin{pmatrix} \nu_e \\ e \end{pmatrix}$	< 2 eV 0.5 MeV	$\begin{pmatrix} \nu_\mu \\ \mu \end{pmatrix}$	< 2 eV 105.7 MeV	$\begin{pmatrix} \nu_\tau \\ \tau \end{pmatrix}$	< 2 eV 1.8 GeV	0 -e	1/2 -1/2	-1 -1

Table 2.1: SM particle generations, with their masses and electric charges, weak isospin and hypercharge (defined in Section 2.1.3). Values collected from Particle Data Group. [1]

The interactions between these matter particles are mediated by gauge bosons. They consist on Quantum Chromodynamics (QCD) [2–4] and on the electromagnetic and weak forces unified in the electroweak interactions [5–7]. The gauge bosons, their masses and electric charges, are detailed in Table 2.2.

Mediator	Interaction	Mass [GeV]	Charge
<i>Gluon</i> ($\times 8$) (g)	Strong	0	0
<i>Photon</i> (γ)	Electromagnetic	0	0
Z	Weak	91.19	0
W^\pm	Weak	80.39	$\pm e$

Table 2.2: SM gauge bosons with their masses and electric charges. Values collected from Particle Data Group. [1]

Besides these gauge bosons, the SM also includes a scalar boson, the Higgs boson, whose field is responsible for the mechanism [8–10] that gives every SM particle its mass.

In the sections below, a brief description of these interactions in their Lagrangian formalism will be given.

2.1.1 Quantum Electrodynamics

Electromagnetism is described by the Maxwell equations

$$\partial_\alpha F_{\beta\gamma} + \partial_\beta F_{\gamma\alpha} + \partial_\gamma F_{\alpha\beta} = 0 \quad (2.1)$$

$$\partial_\mu F^{\mu\nu} = j^\nu \quad (2.2)$$

where ∂ is a partial derivative and $F_{\mu\nu}$ denotes the electromagnetic field tensor, defined by $F_{\mu\nu} = \partial_\mu A_\nu - \partial_\nu A_\mu$, with A being the electromagnetic four-potential. One can see that these equations are invariant to gauge transformations of $A_\mu \rightarrow A_\mu - \partial_\mu \alpha$, with α being a scalar. A free fermion is described by the Dirac Lagrangian density

$$\mathcal{L} = \bar{\Psi}(i\gamma^\mu \partial_\mu - m)\Psi \quad (2.3)$$

with γ_μ being the Dirac matrices defined by the Clifford algebra $\{\gamma^\mu, \gamma^\nu\} = 2\eta^{\mu\nu}$, where $\eta^{\mu\nu}$ is the Minkowski metric. One can also see that this Lagrangian is invariant under global unitary transformations of the form $\Psi \rightarrow e^{-ie\alpha}\Psi$ and $\bar{\Psi} \rightarrow \bar{\Psi}e^{ie\alpha}$. These transformations form a group called $U(1)$. However, if we require that these gauge invariance holds locally as well, i.e. $\Psi \rightarrow e^{-ie\alpha(x)}\Psi$ and $\bar{\Psi} \rightarrow \bar{\Psi}e^{ie\alpha(x)}$, we see that the Dirac Lagrangian density no longer is invariant, as the derivative produces an additional term $\bar{\Psi}\gamma_\mu \partial_\mu \alpha\Psi$.

To maintain local gauge invariance, we should recall the symmetries of Maxwell equations, and change the Lagrangian density of Equation 2.3 to compensate this additional term, by introducing a coupling between the A_μ field and the fermion, thus keeping $U(1)$ invariance:

$$\mathcal{L} = \bar{\Psi}[i\gamma^\mu(\partial_\mu - ieA_\mu) - m]\Psi \quad (2.4)$$

If we now add the free field terms to Equation 2.4 we arrive at the Lagrangian density for Quantum Electrodynamics (QED):

$$\mathcal{L}_{QED} = -\frac{1}{4}F^{\mu\nu}F_{\mu\nu} + \bar{\Psi}[i\gamma^\mu(\partial_\mu - ieA_\mu) - m]\Psi \quad (2.5)$$

This sets a standard way of deriving gauge theories: find the gauge group, make the Lagrangian density invariant and write the free field terms from

the fields that may arise from the imposition of local gauge invariance. The covariant derivative is defined as $D_\mu \equiv \partial_\mu - ieA_\mu$.

It is important to note that a term of the form $\frac{1}{2}m^2 A_\mu A^\mu$, that would be written in a free vector field Lagrangian density is not gauge invariant. This implies that the field mediating QED interactions must be massless. We know this to be the case, as this gauge boson is known to be the photon.

2.1.2 Quantum Chromodynamics

The compositeness of the proton was an indication given by deep inelastic scattering experiments. Also, with the discovery of baryons (qqq , $\bar{q}\bar{q}\bar{q}$) and mesons ($q\bar{q}$), came the idea that protons might be bound states of these quarks. But with the lack of evidence for qq or $\bar{q}\bar{q}$ states, as well as free quarks, came the necessity of introducing a new quantum number, color. The proposition is the following: there are three colors, red (R), blue (B) and green (G); a quark state has a color quantum number associated with it, and an anti-quark state has anti-color; a free particle can only exist as a color singlet state. This proposition can explain why only states with three quarks (making it a singlet, as it possesses the three colors) or quark anti-quark (and, therefore color anti-color, thus a singlet) were found. These states can be represented as vectors:

$$\psi_R = \begin{pmatrix} 1 \\ 0 \\ 0 \end{pmatrix}, \psi_B = \begin{pmatrix} 0 \\ 1 \\ 0 \end{pmatrix}, \psi_G = \begin{pmatrix} 0 \\ 0 \\ 1 \end{pmatrix} \quad (2.6)$$

These states can be rotated into each other by a group of matrices given by the SU(3) group. Local SU(3) transformations have the form $\Psi \rightarrow e^{i\alpha_\alpha T_\alpha} \Psi$, with T_α being the SU(3) generators. Imposing this local gauge invariance to our theory, in analogy to what was done for QED, we introduce the covariant derivative

$$D_\mu = \partial_\mu + ig_s T_\alpha G_\mu^\alpha, \quad (2.7)$$

where G_μ^a being the gluon fields, the gauge bosons that carry color. The coupling strength between gluons and quarks is g_s . The SU(3) generators obey the following commutation relations:

$$[T_a, T_b] = if_{abc}T_c. \quad (2.8)$$

In the fundamental representation of SU(3), T_α can be $\frac{\lambda_\alpha}{2}$, with λ_α being the Gell-Mann matrices.

One feature of QCD is the fact that the structure constants f_{abc} are non-zero, making it a non-abelian theory. With this comes the fact that gluon fields interact with each other. Therefore, the field strength tensor now has three terms (as opposed to its electromagnetic counterpart):

$$G_{\mu\nu}^a = \partial_\mu G_\nu^a - \partial_\nu G_\mu^a - g_s f^{abc} G_\mu^b G_\nu^c. \quad (2.9)$$

The final Lagrangian density then reads:

$$\mathcal{L}_{QCD} = \bar{\Psi}(i\gamma^\mu \partial_\mu - m)\Psi - g_s(\bar{\Psi}\gamma^\mu T_\alpha \Psi)G_\mu^\alpha - \frac{1}{4}G_{\mu\nu}^\alpha G^{\alpha,\mu\nu}. \quad (2.10)$$

This self-interaction feature of QCD leads to the coupling constant being dependent of the scale of the interaction, being higher for lower energy values, and smaller for higher energies. This makes QCD computable with perturbation theory in high energy physics experiments, and in the limit of very high energies, it leads to asymptotic freedom, where quarks propagate as if they were free. However, for lower energies, the coupling increases, reaching a divergence. This property is called confinement, and it is what prohibits quarks and gluons from being free, i.e. when a quark is separated from another, this coupling increases, and the potential energy reaches a point at which creating a quark-antiquark pair from vacuum is energetically favorable. With this, in high energy physics experiments, colored particles will manifest themselves as jets.

2.1.3 Electroweak Interactions

Since the discovery by Wu et al. [11] that weak processes violate parity, there was a need for a theory that would account for this coupling structure, and

move on from the Fermi theory of four-fermion interaction. This was later achieved by Weinberg [5], Glashow [6] and Salam [7], in a gauge theory with the group $SU(2)_L \otimes U(1)_Y$. The L subscript is a reference to the fact that only left-handed particles are affected by weak interactions, and the Y subscript denotes hypercharge, which is given by the Gell-Mann-Nishijima relation $Y = 2Q - 2T_3$, the conserved charge in this symmetry. This chiral structure leads us to writing down the SM fermions grouped as weak isospin multiplets:

$$\begin{aligned} f_L^i &= \begin{pmatrix} l_L^i \\ \nu_L^i \end{pmatrix}, \begin{pmatrix} u_L^i \\ d_L^i \end{pmatrix} \\ f_R^i &= l_R^i, u_R^i, d_R^i \end{aligned} \quad (2.11)$$

with $i=1,2,3$ being the family or generation.

To assemble a gauge theory we write down the covariant derivative, needed to keep gauge invariance:

$$D_\mu = \partial_\mu - ig\hat{T} \cdot \vec{W}_\mu - ig' \frac{Y}{2} B_\mu, \quad (2.12)$$

with g and g' being the $SU(2)_L$ and $U(1)_Y$ coupling constants, respectively, and \hat{T} being the $SU(2)$ generators. \vec{W}_μ are the $SU(2)_L$ gauge fields, B_μ is the $U(1)_Y$ gauge field. The Lagrangian density also needs the kinetic terms for the free fields:

$$\mathcal{L}_{gauge} = -\frac{1}{4}(W_{\mu\nu}^i W^{i,\mu\nu} + B_{\mu\nu} B^{\mu\nu}) \quad (2.13)$$

These field tensors are given by:

$$\begin{aligned} W_{\mu\nu}^i &= \partial_\mu W_\nu^i - \partial_\nu W_\mu^i - g\epsilon^{ijk} W_\mu^j W_\nu^k \\ B_{\mu\nu} &= \partial_\mu B_\nu - \partial_\nu B_\mu \end{aligned} \quad (2.14)$$

ϵ^{ijk} is the $SU(2)$ structure constant, given by the fully anti-symmetric Levi-Civita tensor, and is responsible for the non-abelian nature of the group.

With this, we can write down the final Lagrangian density for electroweak interactions:

$$\mathcal{L}_{EW} = \bar{f}i\gamma^\mu D_\mu f + \mathcal{L}_{gauge} \quad (2.15)$$

In order to keep gauge invariance, these gauge boson fields need to be massless. However, this is not in agreement with experimental evidence that there are massive vector fields [12, 13]. This problem is solved with the introduction of a spontaneous symmetry breaking mechanism that generates masses to these bosons, while keeping the Lagrangian density gauge invariant. This mechanism is described in the following section.

2.1.4 The Brout-Englert-Higgs Mechanism

In order to achieve the spontaneous symmetry breaking, we first need to introduce a doublet scalar field, the Higgs field:

$$\Phi = \begin{pmatrix} \phi^+ \\ \phi^0 \end{pmatrix} \quad (2.16)$$

that contains an electrically charged ϕ^+ and an electrically neutral ϕ^0 .

The Lagrangian density describing these fields, given by kinetic and potential terms is written in Equation 2.17:

$$\mathcal{L}_\Phi = (D_\mu \Phi)^\dagger (D^\mu \Phi) - V(\Phi). \quad (2.17)$$

D_μ is the covariant derivative described by Equation 2.12. The potential $V(\Phi)$ is given by Equation 2.18:

$$V(\Phi) = \mu^2 \Phi^\dagger \Phi - \lambda (\Phi^\dagger \Phi)^2 \quad (2.18)$$

with λ assumed to be positive, in order to give a stable minimum. If μ^2 is positive, the minimum is when $|\Phi| = 0$, and gives an expectation value for the vacuum equal to zero. On the other hand, if μ^2 is negative, the vacuum expectation value is no longer zero, but it is equal to $\frac{\mu^2}{2\lambda} \equiv v$. The plot for this potential is given in Figure 2.1. It can be seen that there are multiple values for the minimum, connected through $SU(2)_L \otimes U(1)_Y$ transformations. We can parametrize the fields around the vacuum expectation value, leaving them as in Equation 2.19:

$$\Phi \equiv \frac{1}{\sqrt{2}} \begin{pmatrix} 0 \\ v + H(x) \end{pmatrix} \quad (2.19)$$

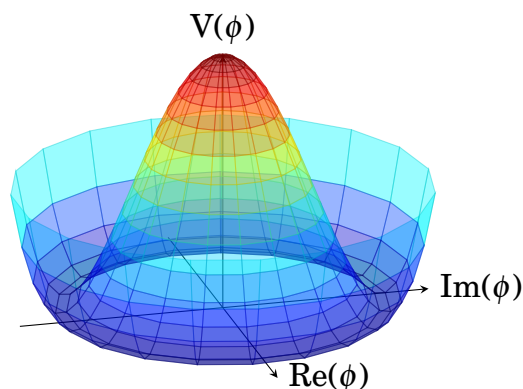


Figure 2.1: The Brout-Englert-Higgs potential.

This expansion around the minimum breaks the gauge symmetry, and with this we can now see how the gauge bosons obtain mass. From Equation 2.17, we write the relevant term:

$$|(-ig\hat{T}\vec{W}_\mu - ig'\frac{Y}{2}B_\mu)\Phi|^2 \quad (2.20)$$

Knowing that the SU(2) generators can be written with the Pauli matrices, this term can be expanded to:

$$\begin{aligned} &= \frac{1}{8} \left| \begin{pmatrix} gW_\mu^3 + g'B_\mu & g(W_\mu^1 - iW_\mu^2) \\ g(W_\mu^1 + iW_\mu^2) & -gW_\mu^3 + g'B_\mu \end{pmatrix} \begin{pmatrix} 0 \\ v \end{pmatrix} \right|^2 \\ &= \frac{1}{8} [v^2 g^2 [(W_\mu^1)^2 + (W_\mu^2)^2] + v^2 (g'B_\mu - gW_\mu^3)(g'B_\mu - gW_\mu^3)] \end{aligned} \quad (2.21)$$

From here it can be seen that:

$$m_W = \frac{1}{2}vg \quad (2.22)$$

Also, defining the mixing between W_μ^3 and B_μ and the physical Z_μ and A_μ , using the Weinberg angle θ_W :

$$\begin{pmatrix} Z_\mu \\ A_\mu \end{pmatrix} = \begin{pmatrix} \cos \theta_W & -\sin \theta_W \\ \sin \theta_W & \cos \theta_W \end{pmatrix} \begin{pmatrix} W_\mu^3 \\ A_\mu \end{pmatrix} \quad (2.23)$$

This leads to:

$$M_Z = \frac{1}{2}v\sqrt{g^2 + g'^2}, M_A = 0 \quad (2.24)$$

As expected, we obtain three massive gauge bosons, that intermediate weak interactions, and a massless boson for the electromagnetic interactions. The Weinberg angle can be obtain by $\cos \theta_W = M_W/M_Z$.

As for fermions, their fields can couple with the Higgs field via a Yukawa term of the form:

$$\mathcal{L}_Y = y_f [\bar{f}_L \Psi f_R + \bar{f}_R \bar{\Psi} f_L] \quad (2.25)$$

It can be seen that this term is gauge invariant. y_f are matrices with the couplings between the Higgs fields and the fermions. Expanding this term as was done with the gauge bosons leads to the following term for the mass of the fermions, at tree level:

$$m_f = y_f \frac{v}{\sqrt{2}} \quad (2.26)$$

From Equation 2.17 we can obtain the expression for the Higgs mass:

$$m_H = \sqrt{2\lambda} v \quad (2.27)$$

The value of g and g' can be obtained using θ_W , as $g \sin \theta_W = g' \cos \theta_W = e$. From Equation 2.22 we get that $v \approx 246$ GeV [1]. So, from Equation 2.27, we need to obtain the value of λ to determine the Higgs boson mass. This can only be done experimentally.

This model is able to explain all fundamental interactions (other than gravity), and fits experimental data very well, but has free parameters not predicted by the model, suggesting that there is a more fundamental theory that can explain these parameters to which the SM is a special case. The free parameters of the are:

- Six quark masses, or six Yukawa couplings to the Higgs field;
- Three charged lepton masses, or the corresponding Yukawa couplings;
- Four CKM matrix parameters: three mixing angles and a CP-violating phase;

- Two Higgs potential parameters, λ and μ , or m_H , m_W and m_Z ;
- Three couplings, given by the electromagnetic and strong coupling constants, and the Weinberg angle.

Given the discovery of neutrino oscillations [14–18], the inclusion of parameters to accommodate for their masses and couplings is necessary as well.

2.1.5 Experimental Tests and Limitations

The SM predictions are, so far, in excellent agreement with the experimental results, as can be seen in Figure 2.2. Among some of its most notable experimental corroborations are the discovery of the charm quark [19, 20] to confirm the GIM mechanism [21], as well as the prediction [22] and discovery [23] of the bottom quark, the tau [24] and its neutrino [25] to establish the existence a third fermion family; the discovery of the Electroweak gauge bosons [12, 13], the discovery of the top quark [26, 27], and most notably the discovery of the Higgs boson [28, 29], making the final coronation to the theory.

However, this cannot be a final theory, as it has many open problems, being often regarded as a low-energy approximation of a more complete model. Besides the mass of neutrinos, some of its problems are listed below:

- It can't make a prediction for the number of fermion families;
- Doesn't include a dark matter candidate [30];
- Doesn't explain the matter/anti-matter asymmetry [31];
- It doesn't provide a description of gravity;
- It has no mechanism that generates the Yukawa couplings of fermions, leaving the big diversity in fermion masses across generations unexplained;

- The extrapolation to higher energies, which has to be done if the SM is to be regarded as a complete theory, leads to a problem in the Higgs quadratic mass. It becomes divergent when loop corrections are accounted for, as it doesn't have any chiral or gauge symmetries to protect it. This problem can be solved if the corrections to the Higgs mass are fine-tuned up to several orders of magnitude. However possible, this doesn't seem to be very natural [32].

VLQ arise from various models that try to tackle this last problem, and they will be described in the following sections.

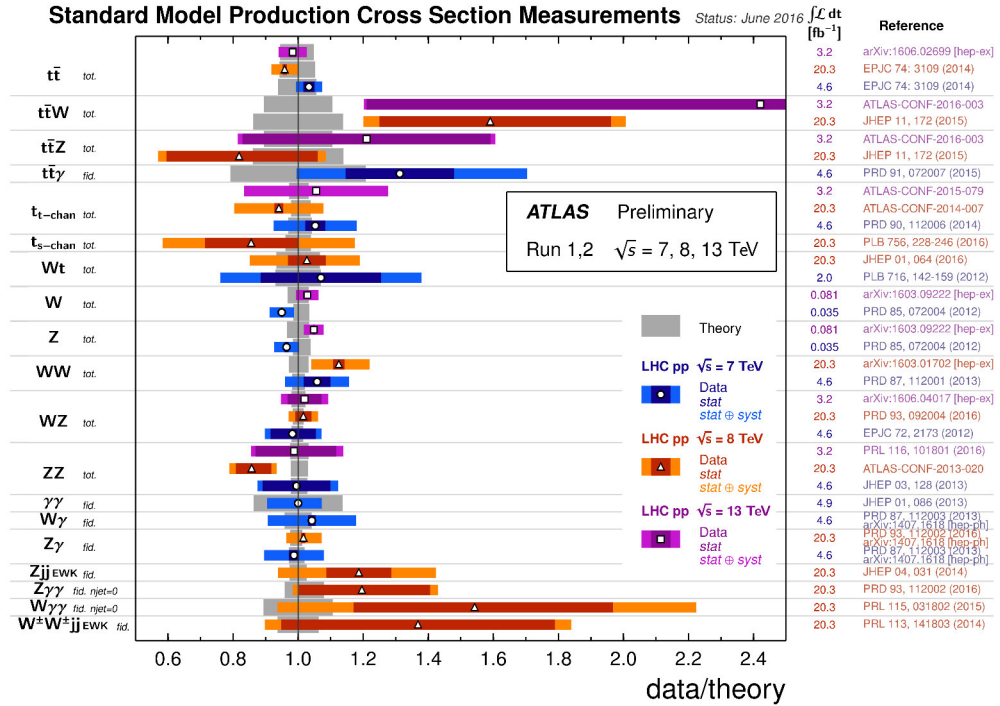


Figure 2.2: The data/theory ratio for several Standard Model total and fiducial production cross section measurements, corrected for leptonic branching fractions. All theoretical expectations were calculated at Next to Leading-Order or higher. [33]

2.2 Vector Like Quarks

2.2.1 Motivation

As the SM doesn't predict the number of fermion families, it is natural to consider a fourth generation. We know that the measurement of the number of neutrino families with a mass smaller than $m_Z/2$ is consistent with 3, as pointed out by the plot in Figure 2.3. However, a new lepton generation

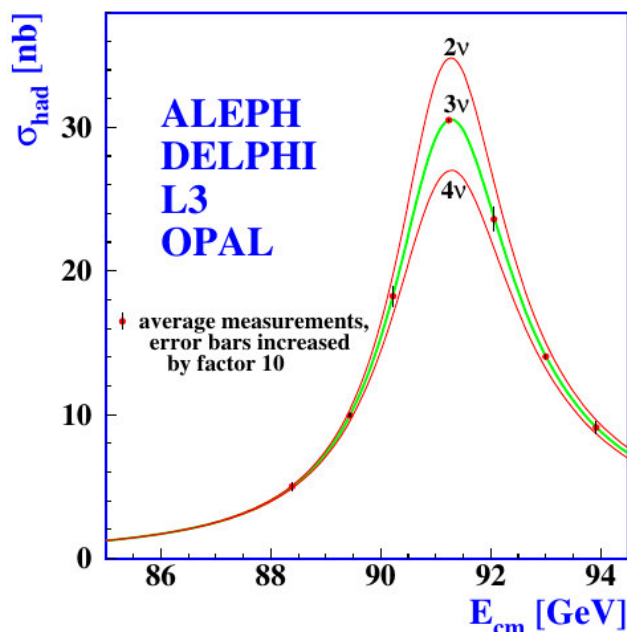


Figure 2.3: Cross section measurements for hadron production predicting two, three and four families of neutrinos with SM couplings and negligible mass. [34]

can have heavier neutrinos. Also, a new quark generation must have higher masses, out of reach from the center of mass energies that were dealt with in past experiments. But these quarks are most likely not chiral, as direct searches exclude them for masses up to 600 GeV [35], and, with the precise measurement of $H \rightarrow \gamma\gamma$ cross section [36], the existence of a sequential fourth generation of quarks is disfavored. [37–39]

On the other hand, if these new quarks were not chiral, but were to have the same left and right-hand charge under the $SU(2)_L \times U(1)_Y$ group, then they wouldn't need to acquire mass through the Brout-Englert-Higgs Mechanism (BEH Mechanism), as a term of the form $m\bar{\Psi}_L\Psi_R$ would be gauge invariant. They would have left-handed (V-A) and right-handed (V+A) charged currents, which is why they are called vector-like.

These quarks appear naturally in non-supersymmetric models that attempt a solution for the naturalness that arises from the hierarchy problem, such as Composite Higgs models [40, 41] and Little Higgs models. [42, 43]

2.2.2 Phenomenology

VLQ are spin 1/2 fermions, triplets under the $SU(3)_C$ gauge group, with the same left and right-hand charge under the $SU(2)_L \times U(1)_Y$ gauge group. They can have tree-level Flavor-Changing Neutral Currents (FCNC) [44], and mix with SM quarks [45, 46]. It is usually assumed that this mixing is predominantly made with the 3rd generation quarks. This mixing with the SM quarks, through Yukawa couplings, introduces a restriction to their possible quantum numbers [47]. Therefore, they can be isospin singlets, doublets or triplets. They can also have SM electric charges (T has $2/3e$ and B has $-1/3e$) or exotic charges (X with $5/3e$ and Y with $-4/3e$). These are summarized in Table 2.3.

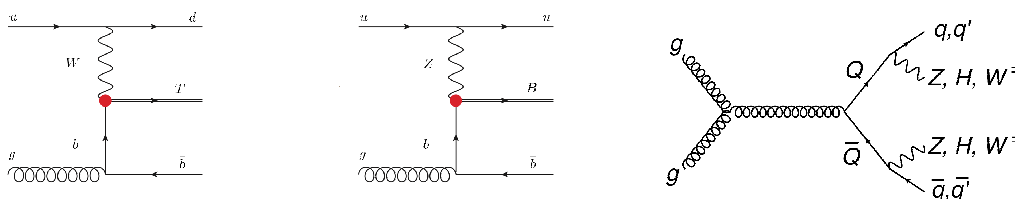
Vector-Like Quarks can be pair-produced via QCD, or singly-produced via electroweak interactions, in association with SM quarks. Figure 2.4 shows Leading-Order examples of Feynman diagrams for the different processes.

Pair production is the dominant mechanism of VLQ production until reaching high masses, where, due to phase-space restrictions, single production becomes dominant. This is illustrated in Figure 2.5.

These quark masses are expected to be almost degenerate, thus forbidding $T \rightarrow WB$ decays, leaving decays to SM quarks as the only available searches. The singlet T and B have the three expected electroweak decays. As for the (T, B) doublet, as their masses are almost equal, the decays depend

	Singlets		Doublets			Triplets	
Multiplets	T	B	$\begin{pmatrix} T \\ B \end{pmatrix}$	$\begin{pmatrix} X \\ T \end{pmatrix}$	$\begin{pmatrix} B \\ Y \end{pmatrix}$	$\begin{pmatrix} X \\ T \\ B \end{pmatrix}$	$\begin{pmatrix} Y \\ B \\ Y \end{pmatrix}$
Isopin	0	0	1/2	1/2	1/2	1	1
Hypercharge	2/3	-1/3	1/6	7/6	-5/6	2/3	-1/3

Table 2.3: VLQ multiplets allowed by SM symmetries.

Figure 2.4: Feynman diagrams for: Left: Single-produced vector-like T ; Center: Single-produced vector-like B ; Right: Pair-produced VLQ. [48]

heavily on the mixing factors in a mixing matrix (an extended CKM matrix that relates weak eigenstates to mass eigenstates). It is usually assumed that the SM top quark has a bigger coupling to the VLQ than the SM bottom quark, suppressing the $T \rightarrow Wb$ decay, as well as $B \rightarrow Hb$ and $B \rightarrow Zb$. This is due to the assumption that the mixing is proportional to m/M (m as the mass of the SM quark and M the mass of the VLQ) [49].

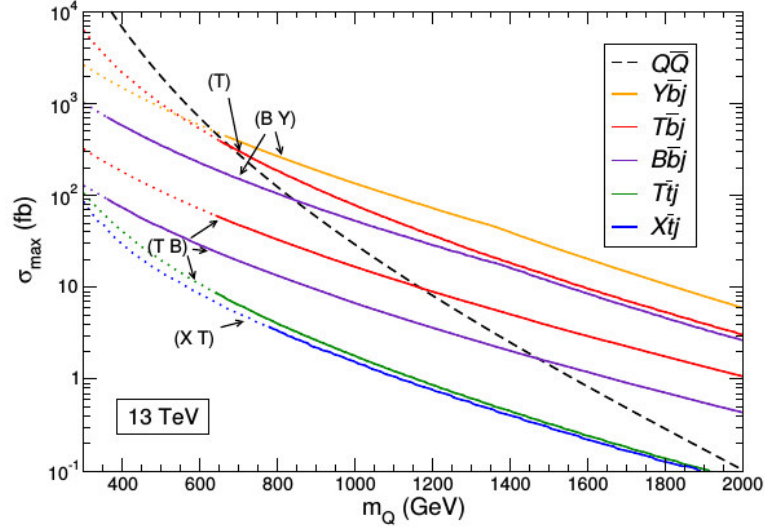


Figure 2.5: Cross-section as a function of the mass of the VLQ for the different production mechanisms. [47]

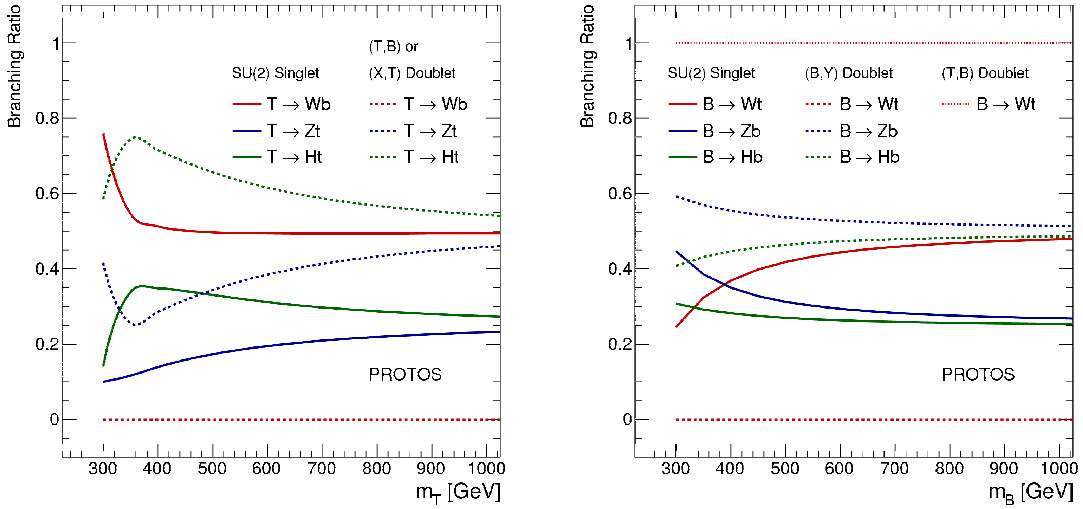


Figure 2.6: Branching Ratio as a function of the mass for vector-like T on the left, and vector-like B on the right. [48]

Current results with 13 TeV data show a 95% CL observed lower limits on pair-produced T quark mass between 700 and 900 GeV, depending on the possible VLQ Branching Ratio (BR). [50, 51] The first phase of opera-

tion of the LHC pair production results exclude masses ranging from about 650 GeV to 900 GeV, depending on the BR to which the corresponding analysis is more sensible. [48, 52–54]. These results assume: vector-like decays to the third generation only; that singlet and doublet kinematics don't change significantly, as can be seen in Figure 2.7. This is also supported by some studies with center-of-mass energy of 8 TeV, that show the differences in kinematics between singlets and doublets fade after the detector simulation [55]; it is also assumed that VLQ pair-production is mediated via SM QCD only (studies where VLQ are produced via other processes, such as heavy gluon fusion were made [56]).

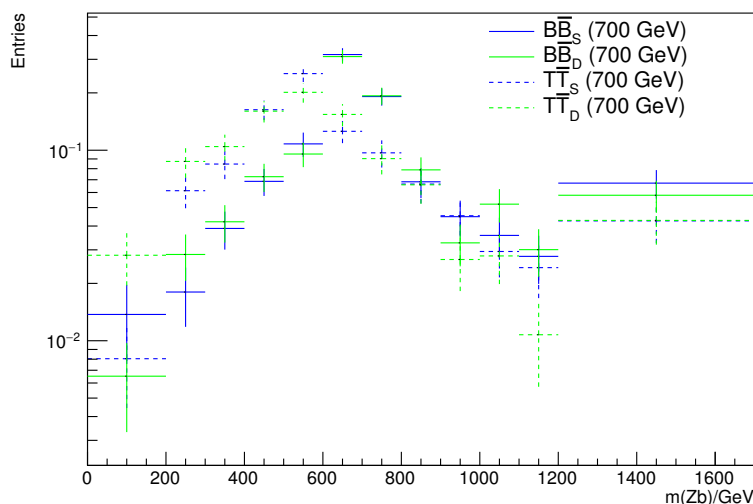


Figure 2.7: Mass of the Zb system for the singlet (blue) and doublet (green) hypothesis. The vector-like B is in full and vector-like T dashed lines. All VLQ masses are set to 700 GeV. At least 2 jets, 1 pair of OS-SF leptons, at least 2 b -tagged jets and p_T higher than 200 GeV and H_T of jets higher than 700 GeV is required

Single production of VLQ features results where cross sections times branching ratio limits are set, at 13 TeV [58, 59] and at the 8 TeV. [48, 60] After these results are obtained, an interpretation is made to infer values

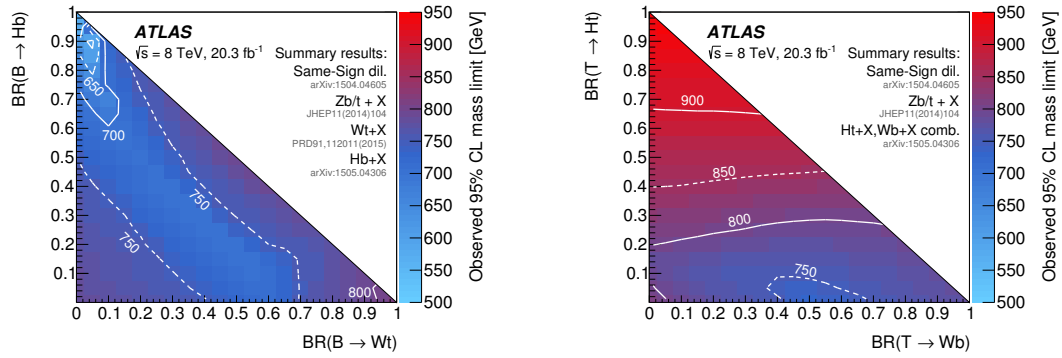


Figure 2.8: Summary of observed mass limits (95% CL) for pair production of vector-like B on the left and vector-like T on the right, with results from the first operation phase of the LHC. [57]

of the couplings as a function of the VLQ masses. These results assume SM Electroweak production only, and are more model dependent than the pair-production ones, because single-production relies on the coupling to the different Electroweak bosons.

Chapter 3

Experimental Setup

3.1 The LHC

The LHC [61] is the world's highest-energy particle accelerator, located at the European Organization for Nuclear Research (CERN), in Geneva, Switzerland. It is a circular accelerator, which is beneficial, for having the possibility of circulating the beams in loops until they reach the desired energy (something that can not be done in linear accelerators), but has the drawback of losing energy via synchrotron radiation, which is proportional to the inverse of the radius of the loop, and to the fourth power of the mass of the circulating particles [62]. This justifies the choice of colliding hadrons instead of electrons, as they are much heavier, as well as the desire to have accelerators with higher radius.

This collider is located in an underground tunnel with a circumference of 27 km, and depth ranging from 45 to 170 m. It has four detectors: ALICE [63], focusing on heavy-ion collision; LHCb [64], for the studies of B -hadrons; ATLAS [65] and CMS [66], that are multipurpose experiments. These are the four interaction points of the LHC, where the beams collide. Despite both protons and heavy ions being collided at the LHC, this text focuses on the collision of protons. These are accelerated at the LINAC2 linear accelerator, after being ionized from a hydrogen gas. After this first

boost to energies up to 50 MeV, these protons form bunches with the usage of magnetic quadrupoles. The Proton Synchrotron Booster (PSB) gets these bunches to the energy of 25 GeV, at which point they are transferred to the Super Proton Synchrotron (SPS), and accelerated to 450 GeV. At this stage they enter the LHC beam pipes, being boosted to their final energy (at Run 1 it was up to 4 TeV per beam, making the center-of-mass energy 8 TeV, but at Run 2 it goes up to 6.5 TeV per beam). These bunches are spaced by 25 ns, and contain $\approx 10^{11}$ protons. The beams are kept in orbit by superconducting magnetic dipoles, operating at 1.9 K, cooled by liquid helium, making a magnetic field, with the value of 8.3 T, in opposite directions.

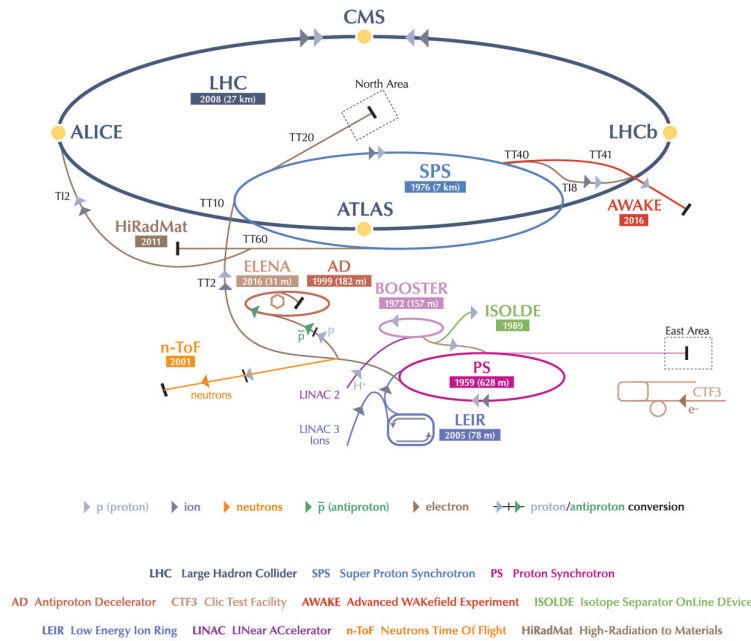


Figure 3.1: Schematic representation of the different LHC accelerators. [67]

3.2 The ATLAS Detector

The ATLAS detector is a general purpose experiment, designed to study proton-proton collisions of the LHC. It has height of 25 m, a length of 44 m and weights 7 kT. It consists of concentric, cylindrical sub-detectors, built around the beam pipe, as is shown in Figure 3.2.

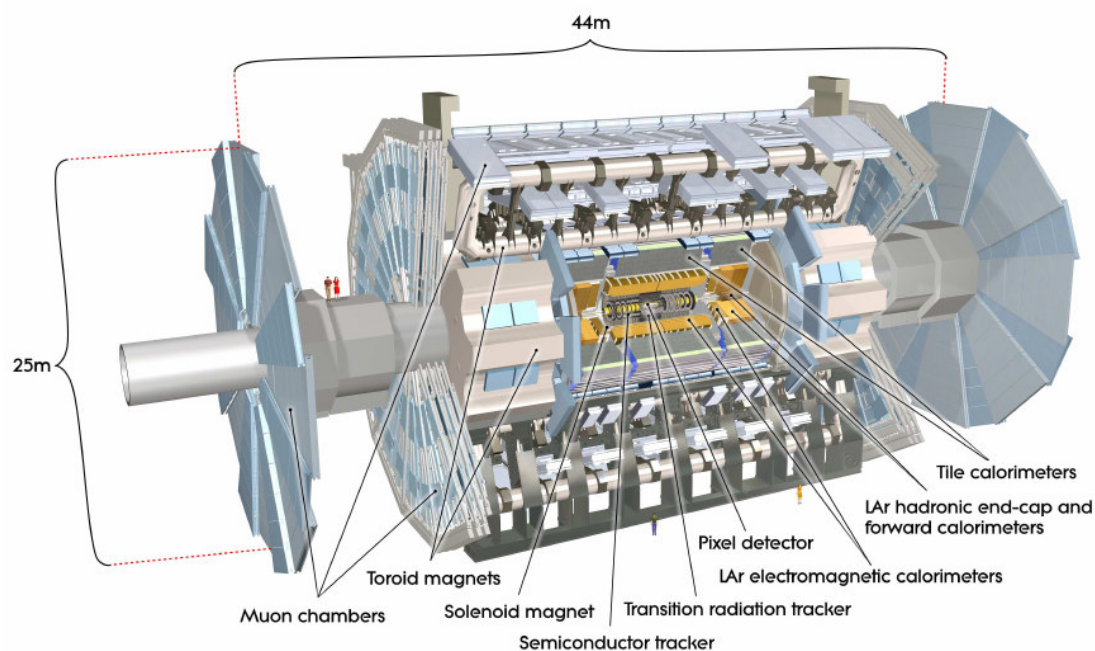


Figure 3.2: Cut-away view of the ATLAS detector layout. [65]

The coordinate system is a right-handed Cartesian one, with the origin at the center of the detector, the z-axis pointing along the beam pipe, the x-axis pointing towards the center of the LHC, and the y-axis pointing upwards. From this point forward, ϕ refers to the azimuthal angle and θ to the polar angle.

At this point it is relevant to define rapidity, given by:

$$y = \frac{1}{2} \ln \left(\frac{E + p_z}{E - p_z} \right) \quad (3.1)$$

with E being the particle energy and p_z being the z-component of its mo-

mentum. In a vanishing mass approximation it is also useful to define the pseudorapidity, given by:

$$\eta = -\ln\left(\tan\frac{\theta}{2}\right) \quad (3.2)$$

These quantities are boost-invariant along the z-direction, but pseudorapidity is used more often as it only requires the knowledge of the particle's polar angle, and because it increases slowly for the central values of the detector, while changing more rapidly when approaching the beam pipe, providing a better mapping of the detector's operational angles. ΔR will also be often used, and it is defined as $\sqrt{\Delta\phi^2 + \Delta\eta^2}$.

3.2.1 Inner Detector

The first sub-detector, closest to the interaction point, is the Inner Detector (ID). Its main purpose is to track charged particles that may arise from the proton collisions, allowing to measure its momentum, as well as making a vertex reconstruction in the range of $|\eta| < 2.5$ possible.

The ID is a cylinder with 6 m of length, with a transverse momentum¹ (p_T) resolution of $\sigma_{p_T}/p_T = 0.05\% p_T \oplus 1\%$. The design must include good resistance to radiation coming from the beam pipe; very fast electronics, to be able to process the large amount of collisions and particles resulting from these; and not degrade the energy resolution of the calorimeters.

The ID is composed of four independent sub-detectors that complement each other: the Insertable B-Layer, the Pixel detector, the Semiconductor tracker and the Transition Radiation Tracker. These four components will be individually described below.

Insertable B-Layer

The Insertable B-Layer (IBL) was an upgrade to the ID made in 2014. Since the original design of the pixel detector was made to a luminosity peak of

¹ $p_T = \sqrt{p_x^2 + p_y^2}$ is a useful variable, as it must always add up to zero, due to the collisions being aligned in the z-direction

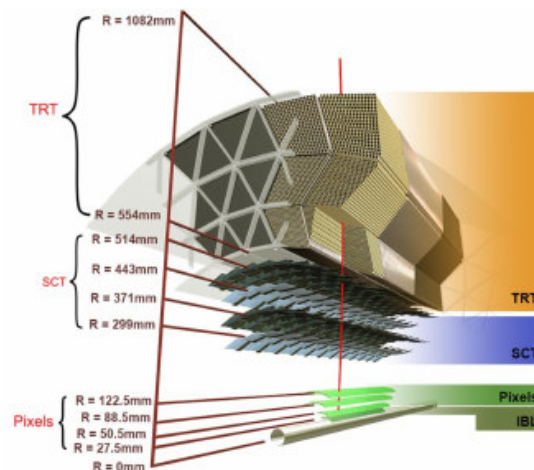


Figure 3.3: Schematic representation of the ATLAS Inner Detector. [68]

$1 \times 10^{34} \text{ cm}^{-2} \text{ s}^{-1}$, an upgrade was in order, to avoid degradation of tracking and vertex reconstruction of the ID.

The IBL consists of 14 staves, each 64 cm long, around the beam pipe with an average distance of 32.35 mm, covering $|\eta| \leq 2.9$. It has about 26880 pixels, each with $50 \times 250 \mu\text{m}^2$, organized in 80 columns and 336 rows.

Pixel detector

The pixel detector is composed of three cylindrical layers located between 5 and 12 cm in radial distance from the beam pipe. The innermost layer is a detector used for reconstructing the secondary vertex of b -hadron decays, crucial to b -tagging.

This component of the ID has ≈ 80 million pixels, each with $50 \times 400 \mu\text{m}^2$. It has a spatial resolution ranging from $10 \mu\text{m}$ to $115 \mu\text{m}$, depending on the plane it is operating on.

Semiconductor Tracker

The third layer of the ID is the Semiconductor Tracker. It provides a further position measurement of the charged particles. Containing four layers of

silicon micro-strip detectors and two endcaps with nine disks each, it covers the range of $|\eta| < 2.5$. The spatial resolution of the Semiconductor Tracker goes from 17 to 580 μm , depending on the plane in which the measurement is being made.

Transition Radiation Tracker

The Transition Radiation Tracker (TRT) is the outermost component of the ID. A TRT cell has a coaxial capacitor with 4 mm of diameter serving as the cathode and a gold plated wire in the middle serving as the anode, with the space in the middle being filled with plastic fibers with different refractive indices. These tubes are filled with a xenon-based gas mixture.

When a charged particle crosses a TRT cell, it ionizes the gas and produces radiation that is collected by the wire. The intensity of this radiation is proportional to E/m of the incoming particle. The drift time of the charge produce by the ionization of the gas can be used to measure the position of the particle. Combining this with the measurement of the radiation energy, it allows to discriminate between electrons and hadrons. The spatial resolution of the TRT is 130 μm .

3.2.2 Calorimeter System

The Calorimeter System (CS) provides an accurate measurement of the particles energy, by studying the deposition it leaves on the detector material as it progresses through it. This also provides some insight to the identity of the incoming particle, as electrons and photons interact differently than hadrons. The former group of particles have electromagnetic interactions with the atoms in the material, whereas hadrons mostly have strong interactions with the material's atoms.

Because of these two distinct forms of interactions, the CS has two components:

- Electromagnetic processes such as bremsstrahlung or electron-positron pair production go on when particles interact with the sub-detector material

as long as it is energetically viable. The Electromagnetic Calorimeter specializes in the measurement of electrons, positrons and photons energy via QED processes.

- The Hadronic Calorimeter looks at the particle production and nuclei excitations and ionizations resulting in particle showers.

For this, both calorimeters need to have good segmentation and cover space well. Segmentation in the longitudinal and azimuthal directions provide three-dimensional reconstructions, very useful for clusters of particles. The coverage of the CS is $|\eta| < 4.9$. Also, they need to account for stable and weakly interacting particles, such as neutrinos, by compensating for the missing energy.

A brief description of these two calorimeters will be provided in the section below.

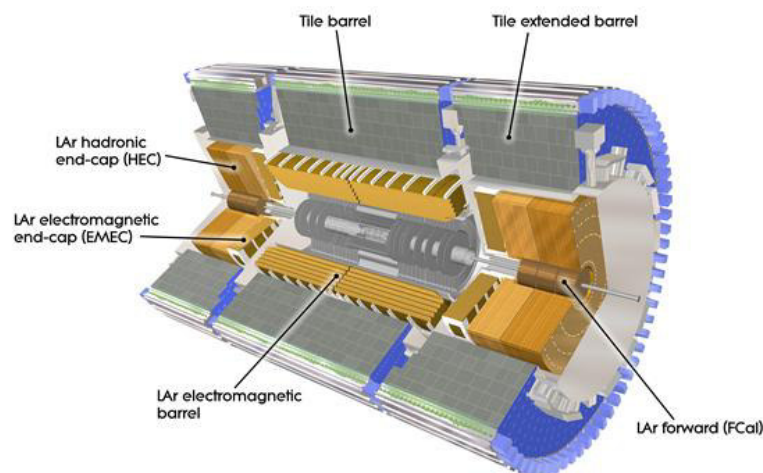


Figure 3.4: Schematic view of the ATLAS Calorimeter System. [69]

Electromagnetic Calorimeter

The Electromagnetic Calorimeter uses liquid Argon (LAr) as the active material and lead plates as the absorber. It is built with an accordion shape, oriented in the radial direction in order to have a symmetric coverage with-

out any cracks in the azimuthal direction. Between plates, high voltage is applied to collect the ionization of the liquid argon. The energy resolution of the Electromagnetic Calorimeter is $\sigma_E/E = 10\%/\sqrt{E} \oplus 0.7\%$ (E in GeV).

Hadronic Calorimeter

The Hadronic Calorimeter is divided into three components: the Tile Calorimeter (TileCal), the Hadronic End-Cap calorimeter (HEC) and the Forward Calorimeter (FCal).

The TileCal is composed of steel tiles as the absorber and plastic scintillators as the active material. Light produced in the TileCal is collected by photomultiplier tubes linked to readout channels, that are grouped into cells.

The HEC has two disks built with copper and LAr, acting as the absorber and the active material, respectively. Immersed in the LAr there are electrodes collecting ionization charges from the hadronic showers.

The FCal has a layer using copper as the absorber, and two other layers using tungsten. LAr is the active material for all the layers of the Fcal. This calorimeter is a combined electromagnetic (the copper layer) and hadronic (tungsten layers) calorimeter, and covers the forward region $3.1 < |\eta| < 4.9$.

The energy resolution of the Hadronic Calorimeter is $\sigma_E/E = 50\%\sqrt{E} \oplus 3\%$ (E in GeV).

3.2.3 Muon Spectrometer

The outermost part of the ATLAS detector is the Muon Spectrometer (MS). It contains various sub-detectors that are useful to both detect the muons and also to measure their momentum, in a range of 3 GeV to 1 TeV, for $|\eta| < 2.7$. It has a toroid magnet system that bends the muon traces, and trigger system active in the region of $|\eta| < 2.4$. It has a barrel, with three cylindrical layers parallel to the beam pipe and two endcaps with four wheels perpendicular to the beam pipe. The Monitored Drift Tubes (MDTs) provide

a measurement of the coordinates of the muon track and help reducing the fake tracks. The Cathode Strip Chambers (CSC) locates muon tracks for higher values of η ($2 < |\eta| < 2.7$). The Resistive Plate Chambers (RPC) are used as fast trigger detectors in the barrel region of the MS, and Thin Gap Chambers (TGCs) in the endcaps.

3.2.4 Magnetic System

The ID and the MS are immersed in a magnetic field, allowing them to measure the momentum of particles.

The ID is inside a superconducting solenoid aligned along the beam pipe, providing a magnetic field of 2 T at the interaction point, dropping in value as one moves further from the beam pipe. This solenoid has an inner radius of 2.46 m and an outer radius of 2.6 m, with a length of 5.3 m.

The MS has a magnetic system composed of a barrel and two endcap toroids. The barrel toroid is 25.3 m long, with an inner and outer radius of ≈ 5 and 10 m, respectively. It has eight superconducting coils. Each endcap toroid has an inner and outer radius of 0.8 and 5.4 m, respectively. The magnetic field in the MS varies from 0.15 and 2.5 T in the barrel magnet, and from 0.2 to 3.5 T in the endcap magnets.

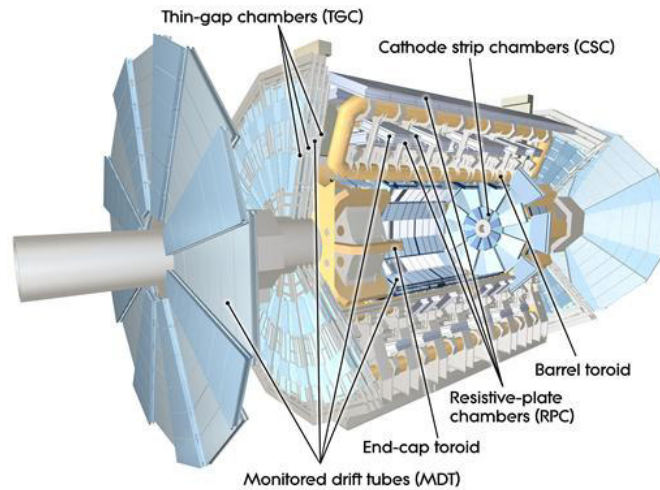


Figure 3.5: Schematic representation of the ATLAS Muon Spectrometer. [70]

3.2.5 Trigger and Data Acquisition

With a collision rate of 40 MHz, it is not possible to collect every event. Assuming an event size of about 1.5 MB, 60 TB/s of data would have to be processed and stored. As this is not doable, the trigger system selects interesting events that match predefined criteria, reducing the event rate to about 200 Hz.

The trigger system consists of three trigger levels: Level 1, the hardware trigger (L1); [71] the software trigger (L2) and the event filter (EF) being the final trigger level. [72]

The L1 trigger searches for event signatures such as high- p_T leptons, jets and photons, as well as Missing Transverse Energy (E_T^{miss}), using the CS and the MS. As it detects interesting events to be recorded, it saves the regions of interest (RoI) in η and ϕ coordinates. The raw event data is then sent to the next trigger level. At this stage, the event rate is lowered to 75 kHz.

The L2 trigger is a software based trigger. It takes about 40 ms to use complex reconstruction algorithms, making use of the RoI sent by the L1 trigger. This trigger trims down the event rate to 3.5 kHz.

Finally comes the EF, taking about 4s to use full precision information over the entire detector, and storing the accepted events to the storage system, with a now reduced rate of about 200 Hz. These stored events are arranged into different datasets by categories based on the reconstructed objects, and further processed by the first stage of the Worldwide LHC Computing Grid (WLCG). The combination of the L2 trigger with the EF is often called the High Level Trigger (HLT).

A period between the start and stop of data acquisition is denominated a Run. In each Run, the smallest data units taken are called luminosity blocks. The duration of each block depends on the luminosity, so that each block takes a comparable amount of data. Automated systems and dedicated shifters alike check the quality of each block, looking for defects in the detector. After this process, usable luminosity blocks are stored in a database called Good Run List that can be used for physics analysis.

After data acquisition, the WLCG is used to store data, process it, and make it available to CERN scientists. It is a distributed computing infrastructure, composed of four layers, formally denominated as tiers. The first tier, Tier-0, is the the CERN Data Center, located in Geneva, Switzerland and the Wigner Research Center for Physics, in Budapest, Hungary. These are linked by a 100 Gb/s connection through its 1200 km of distance. In this layer the raw data is kept, the first reconstructions are made and sent to Tier-1, the next layer of the WLCG. At Tier-1 there are 13 computer centers storing a share of the raw and reconstructed data, reprocessing it and distributing it to Tier-2, the second layer of the WLCG. Tier-0 and Tier-1 are connected through a 10 Gb/s connection to CERN called LHC Optical Private Network. The 13 Tier-1 computer centers are located in 13 different places: Canada, Germany, Spain, France, Italy, Nordic countries, Netherlands, Republic of Korea, Russia, Taiwan, United Kingdom and two in the United States of America. Tier-2 are mostly universities and other scientific institutes that store data and provide computing power for analysis tasks and MC generation. Around the globe there are about 160 Tier-2 sites. The individual scientists that access these sites through local computing resources constitute Tier-3, and have no formal engagement with WLCG.

In this text, 2015 data collected by the ATLAS detector was used, summing up to an integrated luminosity of 3.2 fb^{-1} .

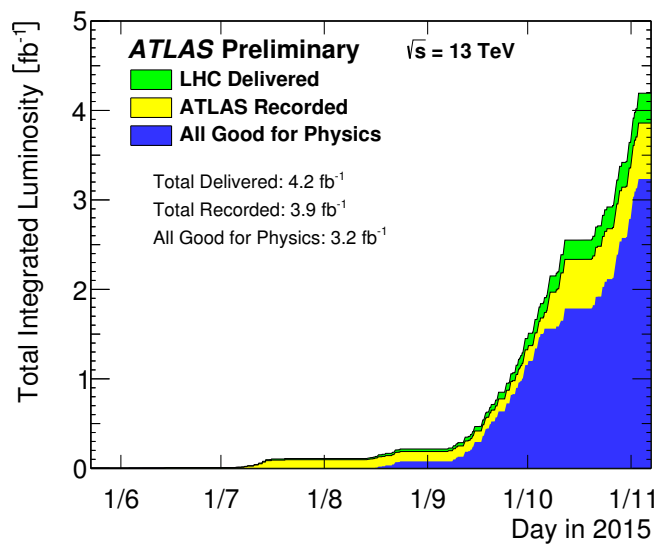


Figure 3.6: Cumulative luminosity versus time delivered by the ATLAS detector. [73]

Chapter 4

Search for Vector Like Quarks

This chapter describes the search for pair-produced VLQ decaying to a Z boson and a third-generation quark. In it we look for pairs of Opposite Sign, Same Flavor (OS-SF) leptons with mass compatible with the Z boson mass and high p_T , at least 2 b -tagged jets and high scalar sum of the selected jets p_T . This is built up from the strategy developed in the first phase of operation of the LHC. [48].

A description of the samples used in the present thesis will be provided, followed by the definition of the physics objects used, the strategy and optimization for isolation of signal, the control regions definitions. Then, the results obtained will be presented, and the complementarity of these with the other branches of this analysis (boosted topologies being done by the TU Dortmund group, and trilepton channel by the Arizona group) will be discussed, followed by a brief section with what the next steps for this analysis will probably be.

4.1 Samples

4.1.1 Signal Samples

The leading-order samples of $T\bar{T}$ and $B\bar{B}$ used were produced using `PROTOS` [74] and using `PYTHIA 8` [75] for hadronization and parton-shower simulation. In order for these samples to be general enough for every VLQ search in ATLAS, they were produced with a BR of 1/3 to each decay mode (Z, W and H). Then, at the analysis level, they are reweighted to the appropriate value. This is done knowing what the BR of each decay mode is to each mass point of the VLQ, also taking into account if it is a SU(2) singlet or doublet (as only vector-like T and vector-like B are considered in this text, SU(2) triplets will not be considered). Then, in each event, using particle level information to know what the VLQ decay modes are, the right weight is applied to correct for the BR.

Samples were generated from 500 to 1400 GeV in the SU(2) singlet hypothesis (with 50 GeV steps for lower mass points and 100 GeV for higher mass points), and 700, 900 and 1200 GeV for the SU(2) doublets hypothesis. They were produced using `GEANT4` [76] to fully simulate all the detector components.

4.1.2 Background Samples

The main irreducible backgrounds in this analysis are Z +bottom and $t\bar{t}$. Z +charm and Z +light are also important backgrounds, but can be reduced with the b -tagged jet requirement. Other important backgrounds include single top production, dibosons production, W +jets and $t\bar{t}+V$, with V being W and Z . When labeling backgrounds in the plots, Other Backgrounds will refer to single top production, dibosons production, W +jets and $t\bar{t}+V$.

It is important to point out that none of these samples were produced by the author of this text. They were produced by the ATLAS Monte Carlo team. Z +jets samples were produced with `SHERPA` [77]. A filter was used to

divide Z +jets into samples with a bottom hadron, a charm hadron and events with non of the two, in this text denominated as light jets. These samples were produced within slices of Z boson p_T , in order to maximize statistics (0-70, 70-140, 140-280, 280-500, 500-700, 700-1000, 1000-2000, >2000, in GeV). All these slices were made for Z decays to electrons, muons and taus. There was a production inclusive in all jets, produced with POWHEG BOX [78] and PYTHIA, but with a quick study it was determined that the SHERPA samples provided a better data/MC agreement and higher statistics in a cut by cut basis, and therefore are the only Z +jets samples considered in this text. The $t\bar{t}$ samples were produced with POWHEG BOX and PYTHIA, with 172.5 GeV as the top quark mass. The single top production samples were produced with POWHEG BOX, as were W +jets samples, both using PYTHIA for hadronization and parton-shower. The single top production samples include both the s and t channels, as well as Wt ; dibosons production samples were produced with SHERPA, and $t\bar{t}+V$ samples were produced with MadGraph5_aMC@NLO [79] and PYTHIA.

4.2 Analysis Strategy

4.2.1 Objects Definition

All jets and leptons are required to have a transverse momentum higher than 25 GeV and $|\eta|$ lower than 2.5. Small-R jets are reconstructed using the anti- k_t algorithm [80] with $\Delta R = 0.4$. A multivariate algorithm, designated mv2c20 [81], using the impact parameters of these jets is used to determine if a jet is originated from a B -hadron or not, with a 70% efficiency working point. This working point was calculated using the discriminating efficiency of the algorithm in $t\bar{t}$ samples. The 70% point is one of a set of four points that were studied and recommended by the algorithm team. A trade-off is made when choosing this value, as a higher working point means higher b -tagging efficiencies, but also means an increase in mistags by the algorithm.

The efficiency of the mv2c20 as function of jets p_T is shown in Figure 4.1.

Figure 4.1: The efficiency to tag b (green), c (blue) and light-flavor (red) jets for the mv2c20 tagging algorithm with the 70% operating point, as a function of the jet p_T . [81]

A single lepton trigger was applied. The single electron trigger used is HLT_e24_lhmedium_L1EM20VH, HLT_e60_lhmedium and HLT_e120_lhloose for Data, and for MC it is HLT_e24_lhmedium_L1EM18VH, HLT_e60_lhmedium and HLT_e120_lhloose. The single muon trigger that was used in this analysis is HLT_mu20_iloose_L1MU15 and HLT_mu50. Electron triggers have a p_T threshold of 24 or 60 GeV (an OR logical operator is used in order to maximize efficiency over a large range of p_T values), while single muon triggers have a p_T threshold of 20 or 50 GeV. The lepton triggers use the L1 trigger with signals from the EM and Hadronic Calorimeter and also the HLT.

To reconstruct an electron, first the EM Calorimeter is used, in which a cluster is searched, using a clustering algorithm [82] to remove duplicates, and is then reconstructed. Once that is done, there is a track reconstruc-

tion, that looks for three hits in different silicon detector layers within the EM Calorimeter region of interest. After that a fit is made within the hypothesis of it being an electron or a pion, and matched to the EM cluster parameters η and ϕ . The next step is to use a multivariate algorithms using track and cluster quantities in order to try to further verify that this object is indeed an electron and not another object capable of leaving a similar signature, such as a jet or a photon, and to do a likelihood fit with three parameters: *Loose*, *Medium* and *Tight*, in order of background rejection. These are subsets of each other, i.e. a *Medium* electron passes the *Loose* requirements, and a *Tight* electron passes the *Medium* requirements. An isolation test may be also applied to try to determine if the electron was originated from a heavy decay such as an electron produced in the decay of a vector boson, or if it is an electron coming from other processes such as a converted photon or an hadronization. This is done by looking at quantities such as the energy isolation of the cluster in the calorimeter, or the isolation of the track produced in the electron reconstruction. [83]

When reconstructing muons, both the ID and the MS are used, and then combined to form the track. At the MS, there is a search for hits in different layers of the MS, that then are fitted to reconstruct the track. When more than one track candidate arises from this, an overlap removal using a χ^2 test with various selection criteria is applied. In the ID, the reconstruction is done following steps analogous to those described previously for the electron reconstruction. Then four types of algorithms can be applied to combine MS and ID information. Similarly to what happens for electrons, muons also have *Loose*, *Medium* and *Tight* identification criteria. These include asking for at least 3 hits in at least two layers of the Monitored Drift Tubes of the MS except in the $|\eta| < 0.1$ region. There is also a compatibility check between quantities from the MS and the ID, such as the ratio between charge and momentum measured in the two sub-detectors. Then track and calorimeter isolation quantities can be used to determine if the muon was produced in a heavy decay or in another process in which it would be asso-

ciated with a jet or another particle. [84]

An overlap removal of leptons and jets is also done. If a small-R jet is within a cone of $\Delta R = 0.2$ from the electron, then the jet is rejected. After that, if the electron has any jet with a cone of $\Delta R = 0.4$, the electron is rejected. For muons the process is slightly different: the cone is p_T dependent, with its radius being defined as $\Delta R = 0.04 + 10 \text{ GeV}/p_T(\mu)$. If the jet outside this cone has at least 3 tracks with its origin in the primary vertex, it is kept.

4.2.2 Signal Region Selection

This text describes a search for pair-produced VLQ decaying to a Z boson and a third-generation quark. Because of the presence of a Z boson, every event must contain a Z boson candidate, i.e. a pair of OS-SF leptons (excluding taus), with invariant mass within 10 GeV of the Z boson mass, $m_Z = 91.18 \text{ GeV}$ [1] (in the case of more than one pair within the mass range, the pair with mass closest to m_Z is chosen). Also, only events with two leptons will be considered, leaving those with three or more leptons to the trilepton channel. This choice is motivated by the lepton multiplicity, displayed in a unit normalized plot in Figure 4.2, with all backgrounds added together, and considering the signal model of SU(2) singlets vector-like T and vector-like B with masses of 800 GeV. It is also important to refer the blinding policy used in ATLAS analysis, where, in order to avoid any possible bias in the analysis strategy, data is not shown until all the strategy is set up, and background modeling is well understood. However, data can be shown in control regions, where the selection applied to events is orthogonal to that applied in the signal region, and therefore will not reveal any potentially bias inducing information. From Figure 4.2 it can be seen that the dilepton channel contains most of the statistics, but a trilepton channel is interesting for its high signal purity. Instead of doing a search inclusive in all lepton multiplicity, a separation between the dilepton and trilepton search is done, and each analysis is optimized on its own, taking advantage of the different

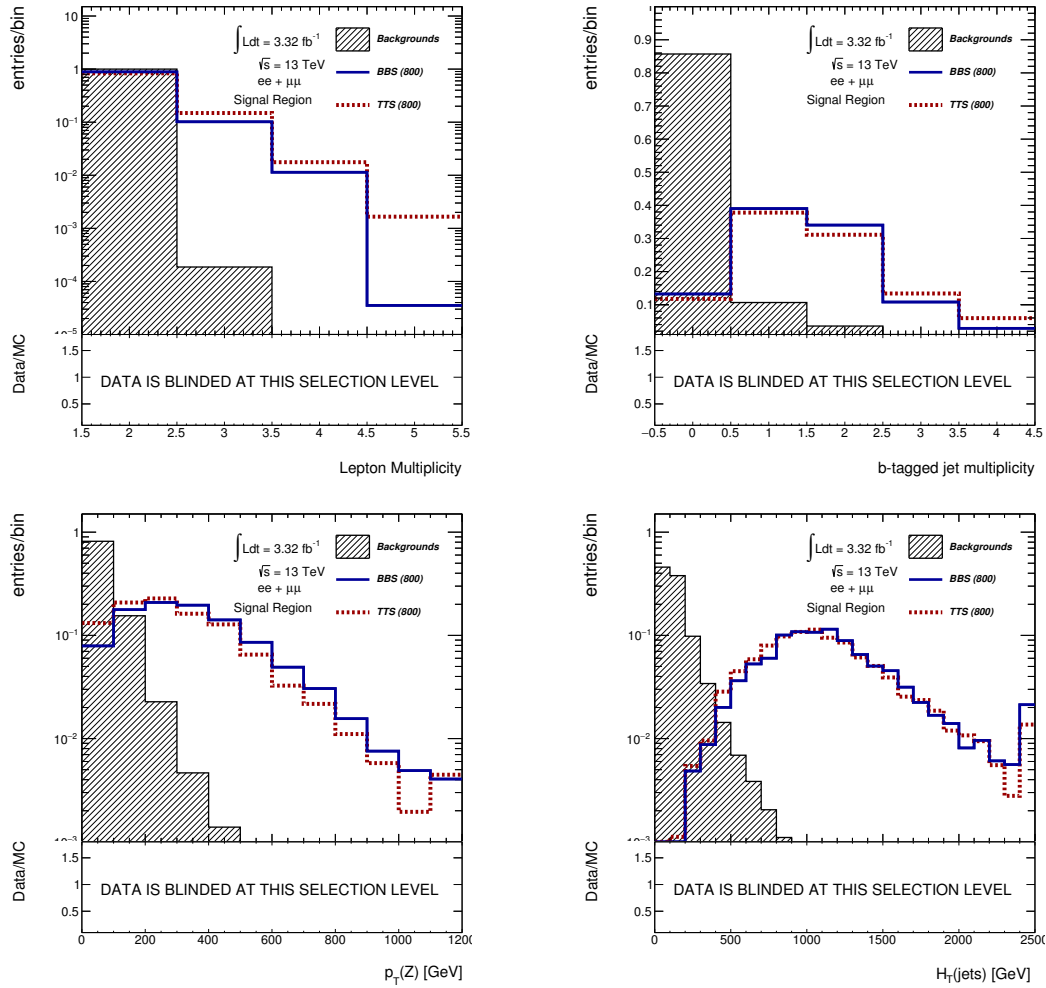


Figure 4.2: On the top the multiplicity of leptons is shown on the left and multiplicity of b -tagged jets on the right. On the bottom, the p_T of Z candidate is shown on the left and H_T of jets on the right. At least 2 jets and a pair of OS-SF were required, except on the multiplicity of lepton, where the requirement on the number of leptons was relaxed.

features of each channel. In the end, the results from both analysis will be combined.

Another interesting multiplicity to take into account in this analysis is that of b -tagged jets, shown in Figure 4.2. The plot from Figure 4.2 shows

that signal produces a higher multiplicity of b -tagged jets than background. This can be easily understood when taking into account that a VLQ decay, in the assumption of decays to third generation only, will always produce at least one b -tagged jet, assuming that a top quark will always decay to a b quark and a W boson (Section 2.2.2 in page 15 describes VLQ decays). Therefore, in this search, every event in the signal region is required to have at least 2 b -tagged jets.

Another difference in signal and background distributions in this search is the Z boson p_T , as it is expected that Z bosons produced via the decay of VLQ will have a harder spectrum than those produced by the background processes. This can be confirmed by Figure 4.2. With this in mind a cut at 200 GeV in the p_T of the Z boson candidate is applied. This value was obtained with an optimization that will be described in the next subsection.

Applying a similar thinking, the H_T of jets (scalar sum of all selected jets transverse momentum) is included in the selection, based on the expectation that the jets produced by VLQ decays will have harder p_T spectrum than those produced via background processes. This distribution is shown in Figure 4.2. In the same optimization that was done for p_T of the Z candidate, the value for the H_T cut was determined to be 700 GeV, to reduce background contamination.

As for the discriminant variable used in this analysis, the choice fell to the invariant mass of the Z boson candidate and the highest- p_T b -tagged jet system, as it is a good reconstruction of the vector-like B . Even though it is not a perfect reconstruction of the vector-like T , it was chosen as a good compromise between having sensitivity for the vector-like B and not dedicating an entire analysis to the vector-like T , to which the trilepton channel is expected to be more sensitive. The difference in shape for signal and background is shown in Figure 4.3, where the expected peak at 800 GeV for the vector-like B is visible.

Besides the unity normalized plots, that illustrate shape differences between signal and background, it is also important to see how our MC is

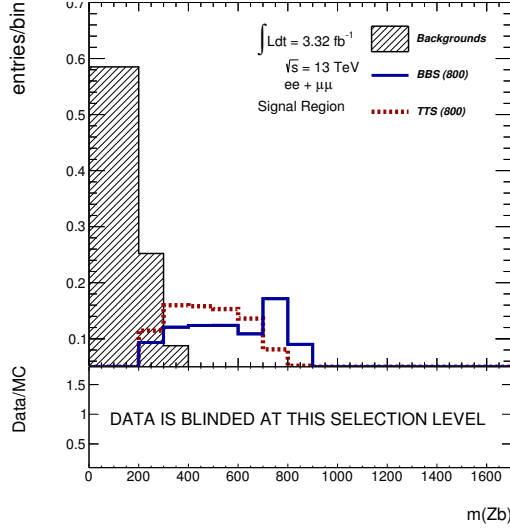


Figure 4.3: The mass of the Zb system with distributions normalized to unity is shown. At least 2 jets and a pair of OS-SF leptons were required.

shaped when normalized to luminosity. From Figure 4.4 we see that our signal jets have a harder p_T spectrum, as expected, even though we can also notice the big cross-section differences. A similar conclusion about signal leptons can be obtained from Figure 4.5. In Figure 4.6 we see the η distributions for jets, and Figure 4.7 for leptons, where the MC appears to be describing our data with no major problems being visible. The polar angle distributions can be seen in Figure 4.8 for jets and Figure 4.9 for leptons, where a fair agreement between data and MC in this angular distribution can be seen. Figure 4.9 has a bin with a big uncertainty, that is most likely due to a big weight event. Figure 4.10 shows the good MC description of the Z mass peak, a region of particular interest for this analysis. In the right plot of Figure 4.10, a lack of MC for low $m(\ell^+ + \ell^-)$ is evident. This is due to the lack of Drell-Yan simulated events in this kinematic region. For the current analysis this is not relevant since the focus will be on the $\ell^+ + \ell^-$ masses close to the Z boson mass.

Figure 4.11 shows the two last variables used in this analysis selection,

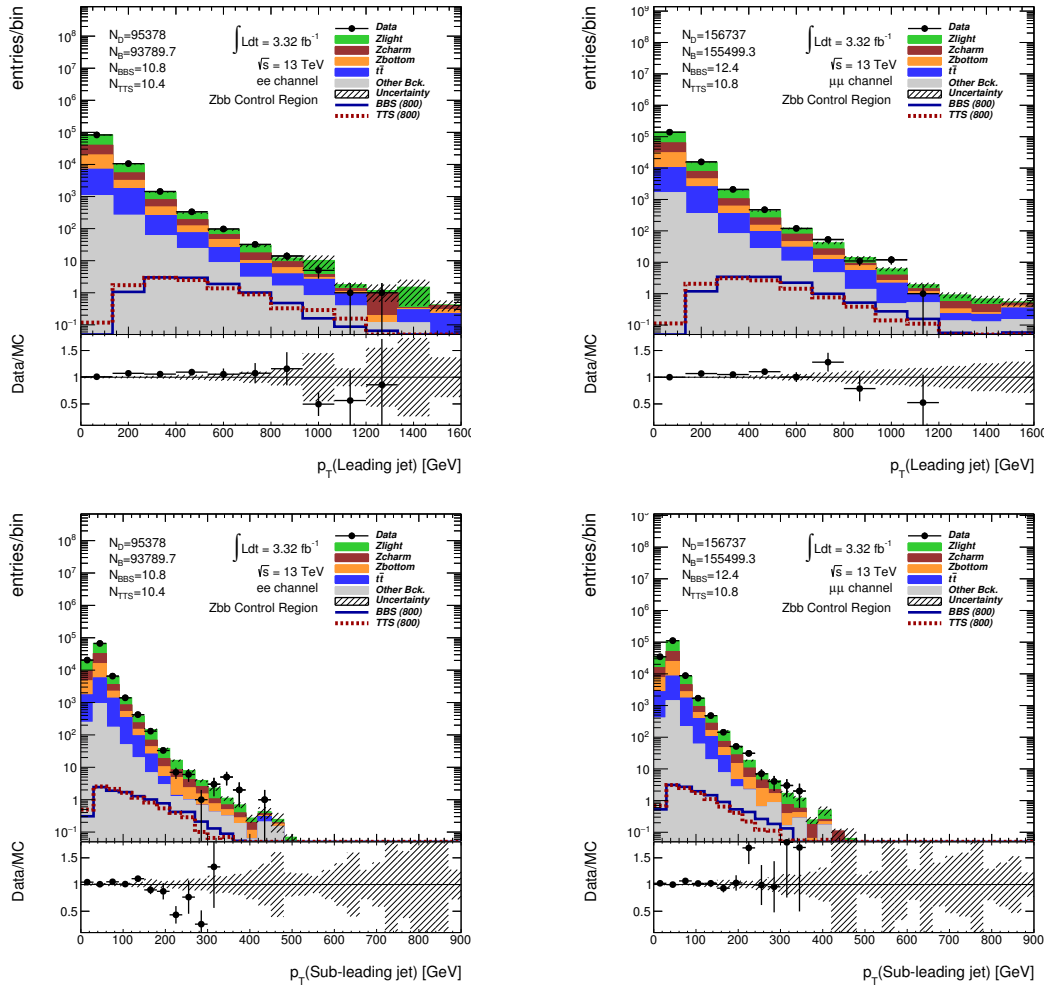


Figure 4.4: The distribution of the leading jet p_T is shown on top, and sub-leading jet p_T on the bottom. The electron channel is shown on the left, and the muon channel on the right. At least 2 jets and a pair of OS-SF leptons is required.

before their respective cut is applied. As was seen in the united normalized plots, signal and MC have different shapes, making this variables the choice for the signal region selection, even though in this luminosity normalized plots the differences in cross-section are more apparent. The discriminant variable in the signal region is shown in Figure 4.12, where the expected

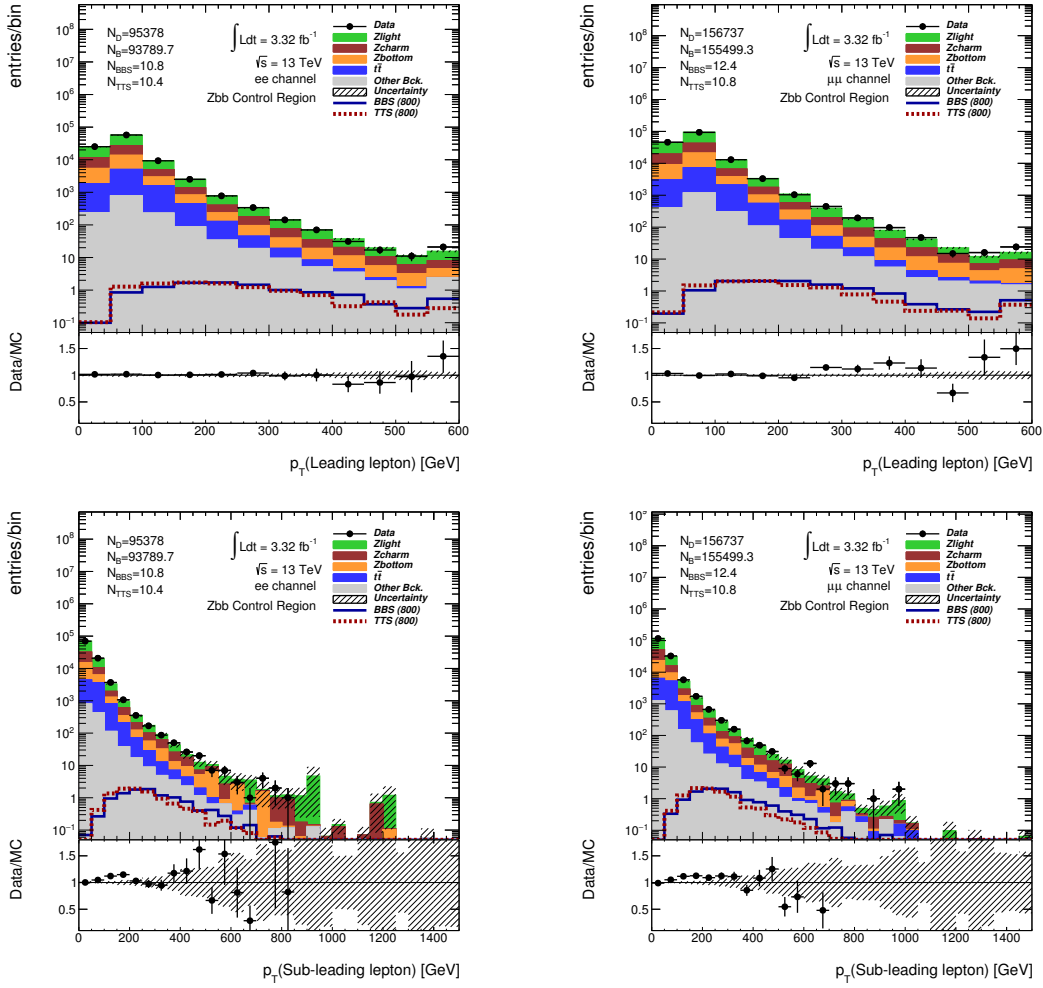


Figure 4.5: Distribution of the leading lepton p_T is shown on top, and sub-leading lepton p_T on the bottom. The electron channel is shown on the left, and the muon channel on the right. At least 2 jets and a pair of OS-SF leptons is required.

$B\bar{B}_S$ peak at around 800 GeV can be seen.

4.2.3 Selection Optimization

In the previous section, the benchmark selection for the signal region was described, and the choice of variables to use was illustrated based on their

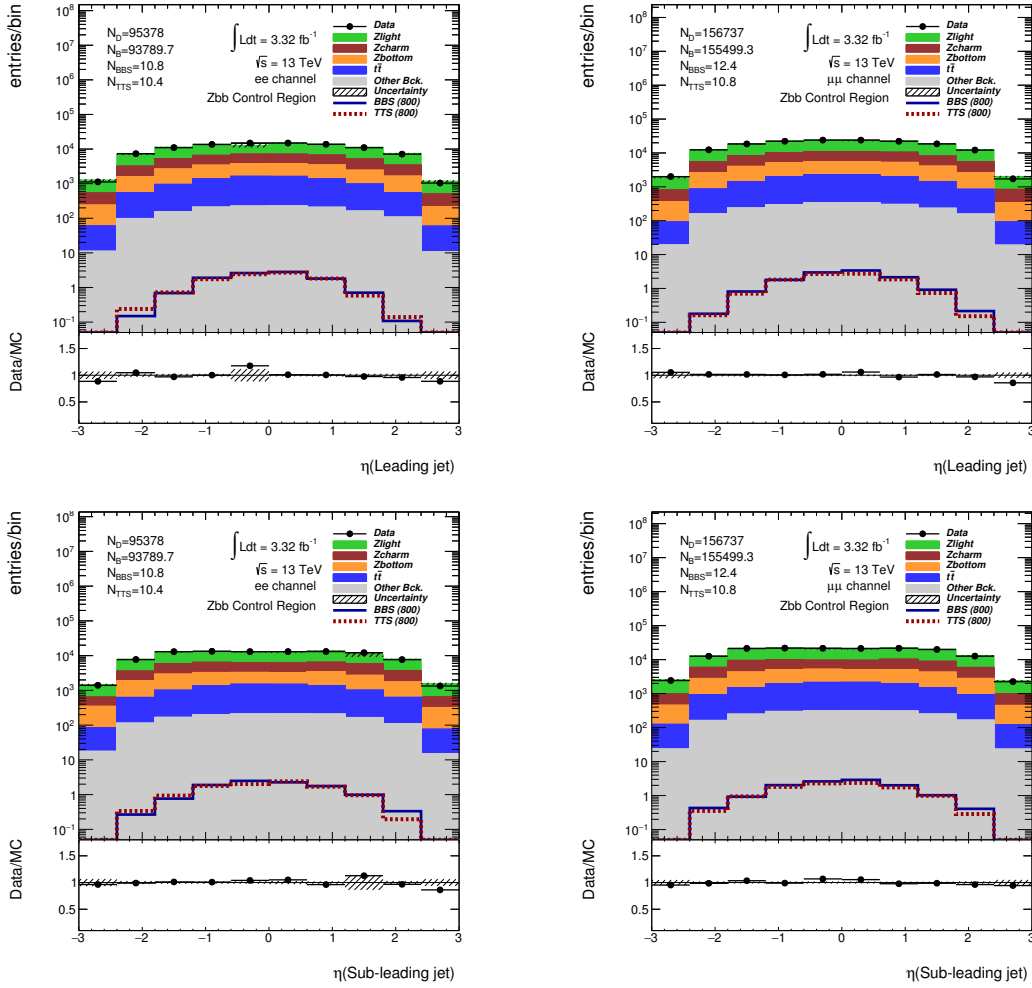


Figure 4.6: The distribution of the leading jet η is shown on top, and sub-leading jet η on the bottom. The electron channel is on the left, and muon channel on the right. At least 2 jets and a pair of OS-SF leptons is required.

shape, and how it differs between background and signal. However, to determine at which value the cuts are optimal, a study was performed based on how much each given pair of p_T of the Z candidate and H_T of jets cut values would improve our expected mass limits for the case of a $SU(2)$ singlet vector-like T and B . These limits were performed using TRexFitter [85], and do not include systematic uncertainties.

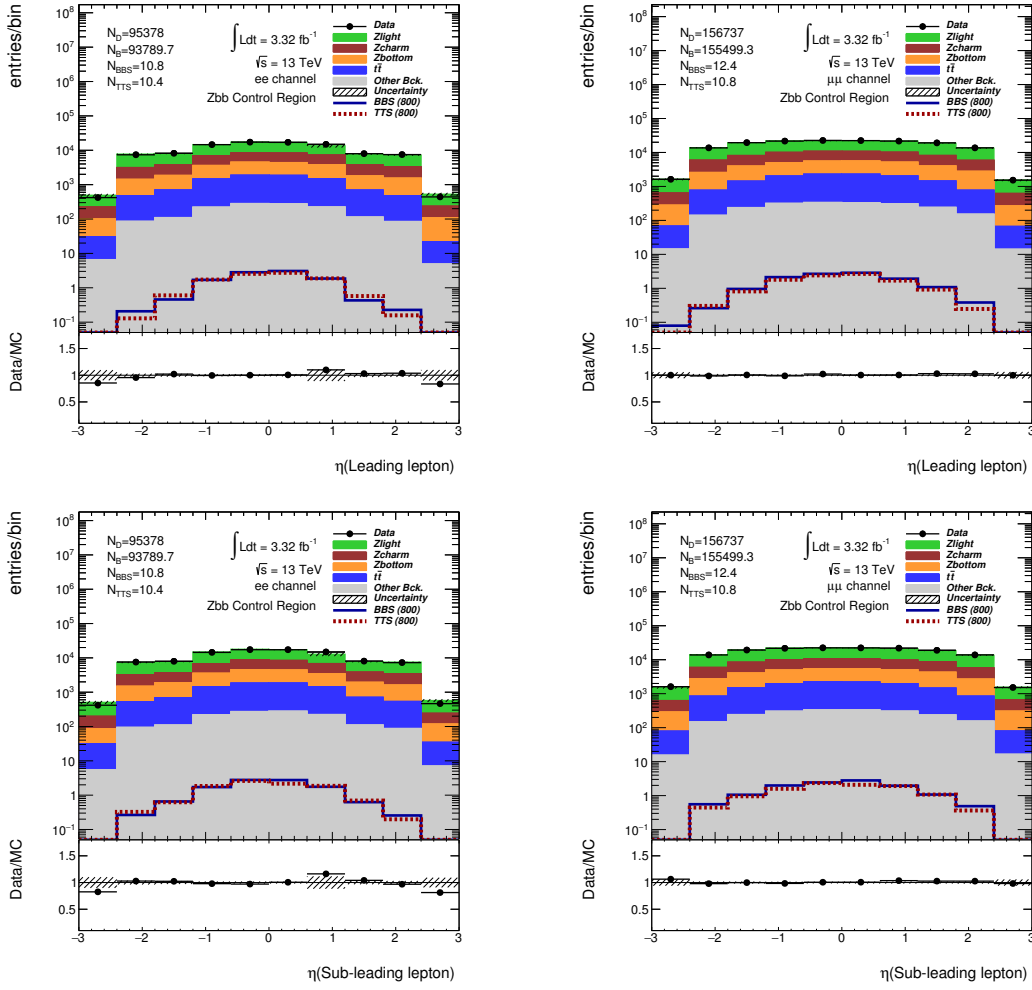


Figure 4.7: The distribution of the leading lepton η is shown on top, and sub-leading lepton η on the bottom. The electron channel is on the left, and muon channel on the right. At least 2 jets and a pair of OS-SF leptons is required.

The results for a SU(2) singlet VLQ are displayed in Figure 4.13, for a vector-like T on top, and vector-like B on the bottom. We see that the optimum values for vector-like T and vector-like B are not the same, so a compromise had to be made. The choice made was to cut on values lower than 200 GeV for the p_T of the Z candidate, and values lower than 700 GeV

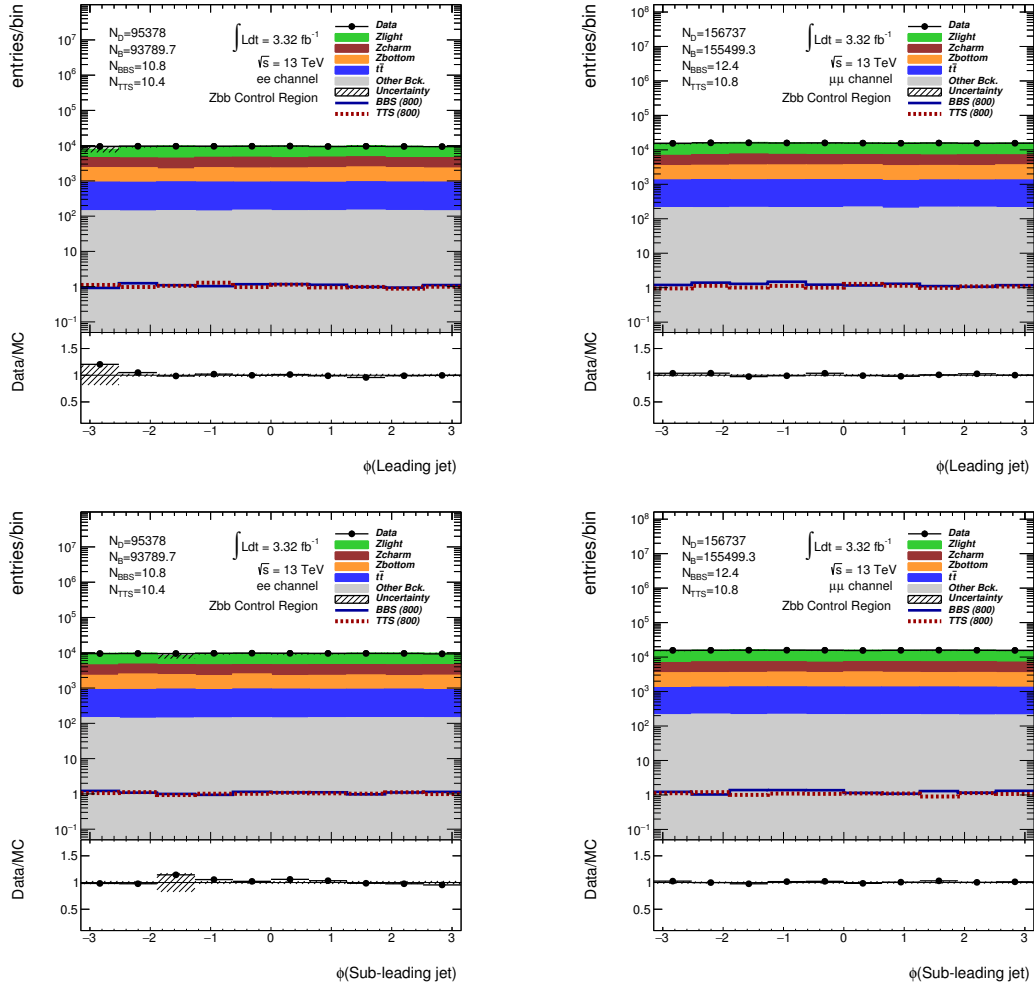


Figure 4.8: The distribution of the leading jet ϕ is shown on top, and sub-leading jet ϕ on the bottom. The electron channel is on the left, and muon channel on the right. At least 2 jets and a pair of OS-SF leptons is required.

for the H_T of jets. This is a conservative choice, due to the fact that the study doesn't incorporate systematic uncertainties. Also, when making the choice, preserving statistics was kept in mind. So, in summary, the selection for the signal region is presented in Table 4.1.

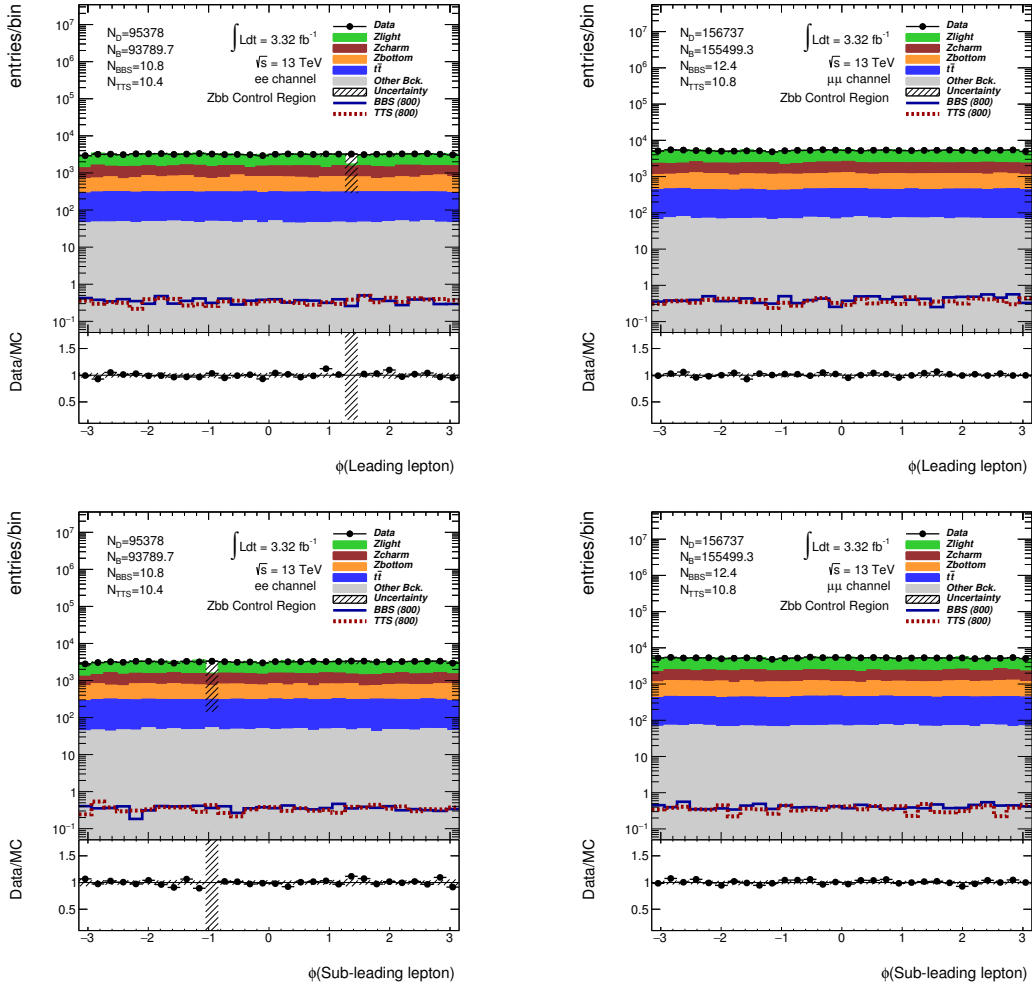


Figure 4.9: The distribution of the leading lepton ϕ is shown on top, and sub-leading lepton ϕ on the bottom. The electron channel is on the left, and muon channel on the right. At least 2 jets and a pair of OS-SF leptons is required.

4.2.4 Control Regions Definition

In order to know if we have a good background modeling with our MC, it is important to have control regions, where it is possible to check it against data and not be spoiling our signal region blinding. That is done by defining regions, via a benchmark selection, targeting a specific background process,

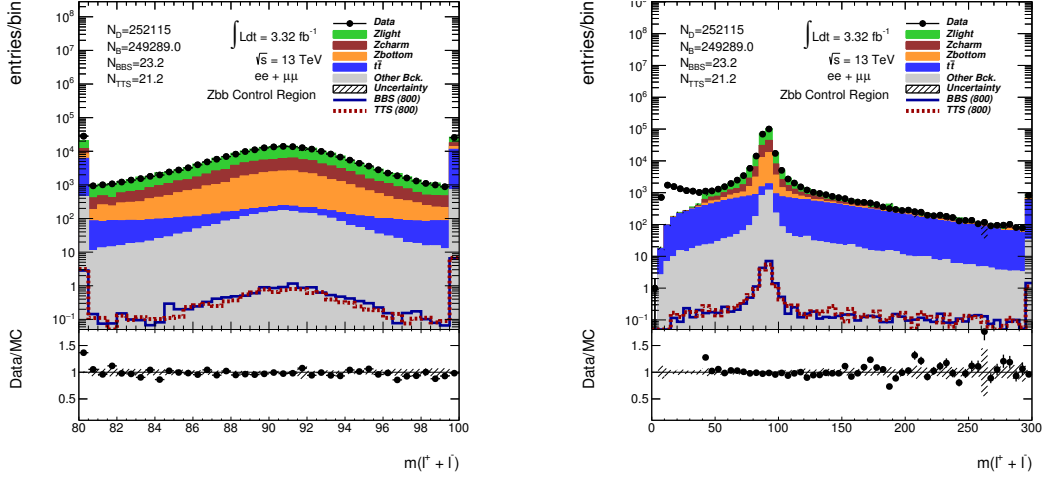


Figure 4.10: The mass of the Z boson candidate inside the resonance is shown on the left and outside the resonance on the right. At least 2 jets and a pair of OS-SF leptons is required.

Selection Level	Requirement
Level 1	≥ 2 jets, 2 OS-SF leptons
Level 2	≥ 2 b -tagged jets
Level 3	$ m_{\ell\ell} - m_Z < 10$ GeV
Level 4	p_T of the Z candidate > 200 GeV
Level 5	H_T of jets > 700 GeV

Table 4.1: Signal region selection.

but always keeping it orthogonal to the signal region.

In the case of this analysis, two control regions were defined, to control the two most important irreducible backgrounds: $Z+b\bar{b}$ and $t\bar{t}$. The selections were obtained targeting specific kinematic features of the background's final state, and how they differentiate from our signal region benchmark selection. For $t\bar{t}$ this is achieved by looking outside the Z mass peak, as we expect it to not be resonant (Z candidate reconstruction for $t\bar{t}$ is expected to be just combinatory of leptons, therefore no natural peak should arise around the

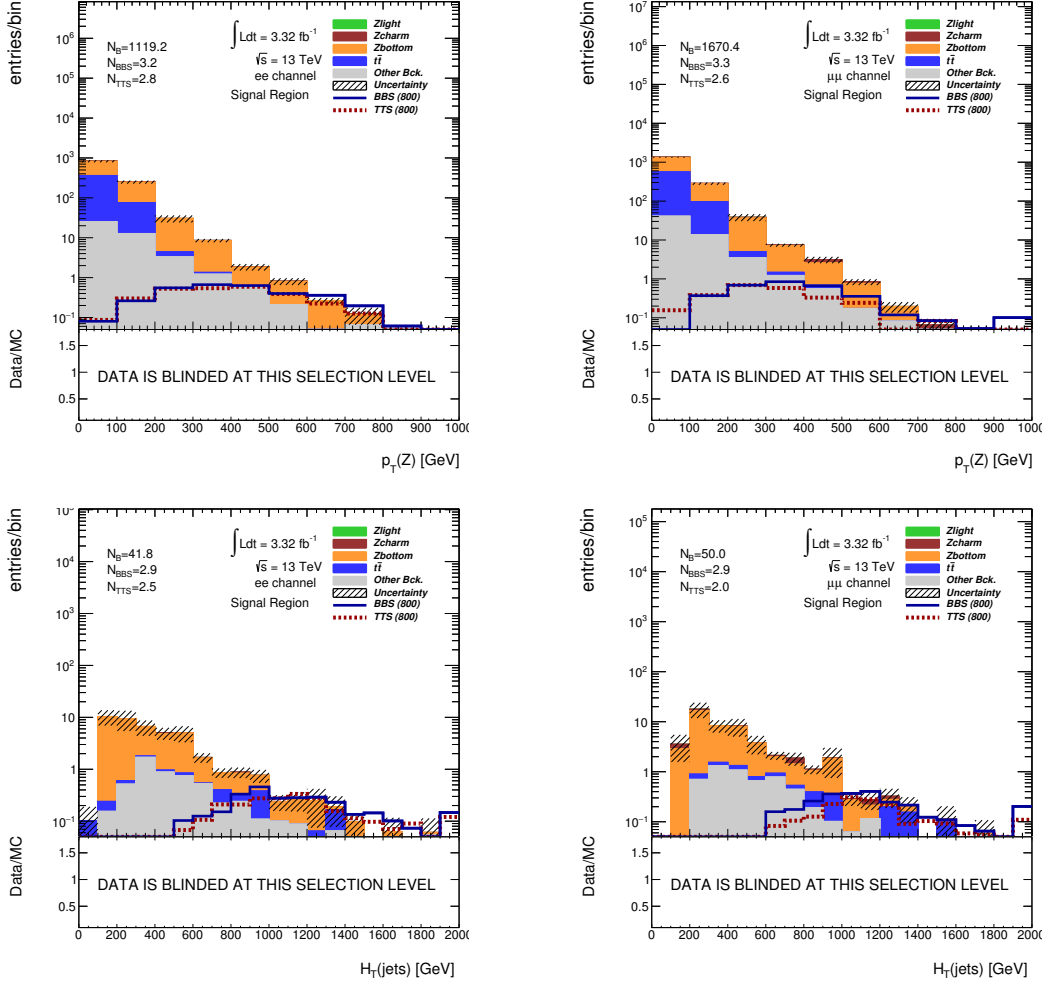


Figure 4.11: On top, the p_T of the Z candidate is shown, reconstructed with electrons on the left, and muons on the right. At least 2 jets, 1 pair of OS-SF leptons and at least 2 b -tagged jets were required.

On the bottom, the H_T of jets is shown, on the left in the electron channel, on the right in the muon channel. At least 2 jets, 1 pair of OS-SF leptons, at least 2 b -tagged jets and p_T higher than 200 GeV were required.

Z mass. This can be seen in Figure 4.22). For $Z + b\bar{b}$, this is done looking at values of p_T of the Z candidate lower than 200 GeV.

So, for the $t\bar{t}$ control region, the benchmark selection is presented in Ta-

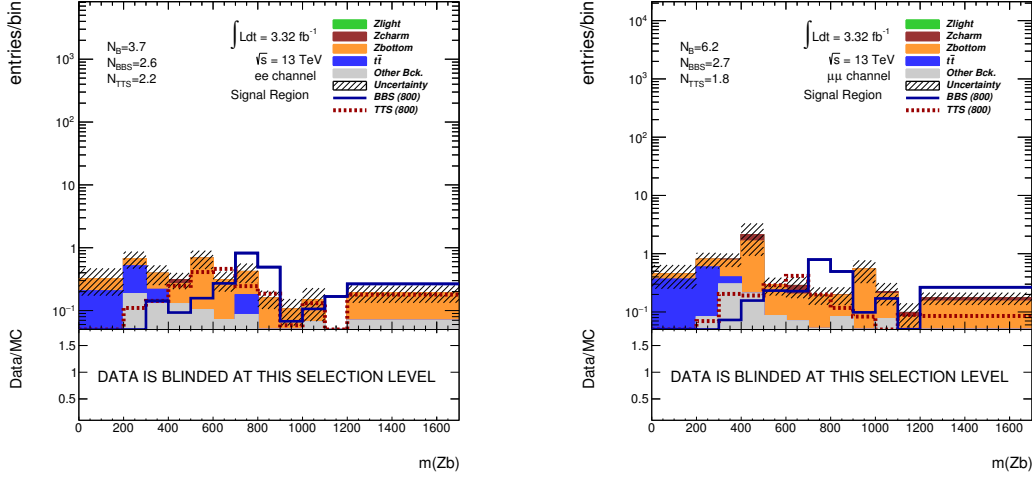


Figure 4.12: The mass of the Zb system is shown. The electron channel is on the left, the muon channel on the right. At least 2 jets, 1 pair of OS-SF leptons, at least 2 b -tagged jets and p_T higher than 200 GeV and H_T of jets higher than 700 GeV is required.

ble 4.2. Notice that the third cut, requiring that the reconstructed Z boson candidate mass is 10 GeV outside the Z mass peak makes this control region orthogonal with the signal region. The yields after applying the benchmark

Selection Level	Requirement
Level 1	≥ 2 jets, 2 OS-SF leptons
Level 2	≥ 2 b -tagged jets
Level 3	$ m_{\ell\ell} - m_Z > 10$ GeV

Table 4.2: $t\bar{t}$ control region selection.

selection are presented in Table 4.3. From Table 4.3 it can be seen that $t\bar{t}$ isolation is very high, with the yields ratio of $t\bar{t}$ and total background being 96%.

Figure 4.14 shows the multiplicity of jets and b -tagged jets. Data and MC do not agree perfectly, specially in the b -tagged multiplicity plot. The

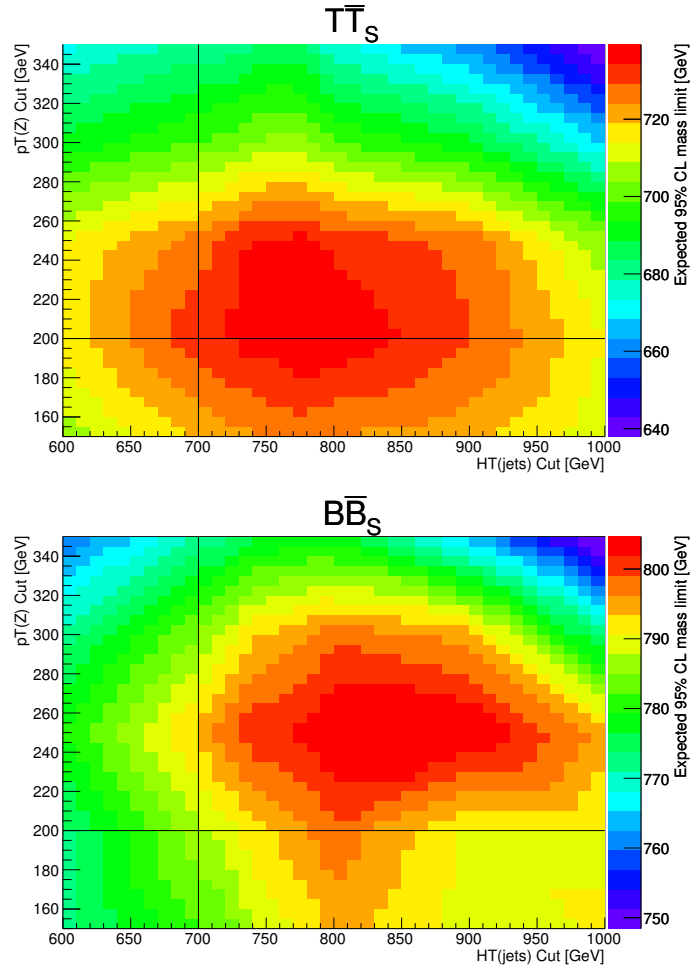


Figure 4.13: The expected mass limits for each cut pair, in a singlet model for vector-like T are shown on top, and vector-like B on the bottom. The line marks the chosen value for each cut.

b -tagged jet multiplicity is difficult to model, but we can see from the distribution that the 2 b -tags regions is fairly well defined, and globally it is well described enough for it not to be a major problem. Plus, systematic uncertainties are not yet implemented, so it is yet to be seen if the total uncertainty can cover the disagreement. Figure 4.15 shows the p_T of jets and Figure 4.16 show the p_T of leptons. Figure 4.17 and Figure 4.18 show the η of jets and leptons, respectively. The distributions of the angle ϕ of jets

	ee	$\mu\mu$
BBS (800)	1.9 ± 0.2	2.1 ± 0.2
TTS (800)	1.5 ± 0.1	1.7 ± 0.1
Z+light jets	0.0 ± 0.0	0.0 ± 0.0
$Z + bb$	19.4 ± 9.6	42.2 ± 8.8
$Z + cc$	3.3 ± 1.9	6.4 ± 4.0
$t\bar{t}$	1532.0 ± 11.3	2206.1 ± 13.8
Other Bck.	42.0 ± 0.9	58.8 ± 1.0
Total bkg.	1596.7 ± 15.0	2313.5 ± 16.9
Data	1693	2338

Table 4.3: Yields for $t\bar{t}$ control region after all the selection is applied. Uncertainties are statistics only.

and leptons are shown in Figure 4.19 and Figure 4.20, respectively. Figure 4.21 shows the discriminant variable after this control region selection is applied. Data and MC agreement in this control region seems to be fair, particularly in the angular distributions and in the mass of the Zb system, as the high p_T region lacks statistics and the MC does not seem to perfectly describe data. All plots show the decent $t\bar{t}$ isolation obtained after this control regions selection is applied, as was seen in Table 4.3.

As for the $Z + b\bar{b}$ control region, the benchmark selection is shown in Table 4.4. In this selection, orthogonality with the signal region is ensured by looking for low Z candidate p_T values. It also requires two b -tagged jets, as is expected when looking for $Z + b\bar{b}$, and looks inside the Z peak. The yields after this selection is applied are shown in Table 4.5.

Looking at Table 4.5 we can see that the ratio between $Z + b\bar{b}$ and total background events is not as high as it is in the $t\bar{t}$ control region. In this control region it is 57%, as $t\bar{t}$ contamination is significant. In order to amend this problem, various approaches were experimented. Cutting in values of

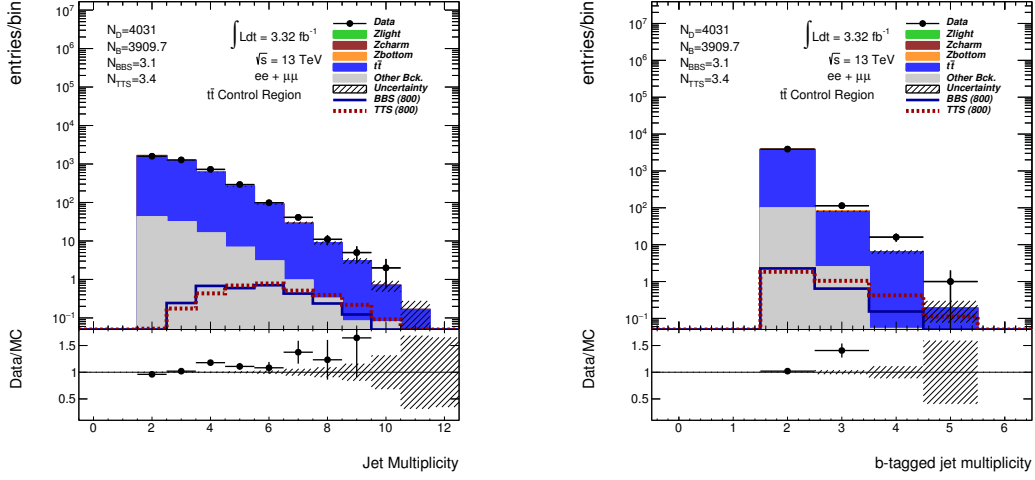


Figure 4.14: The multiplicity of jets is shown on the left, and the multiplicity of b -tagged jets is shown on the right. At least 2 jets, 1 pair of OS-SF leptons 10 GeV outside the Z mass, at least 2 b -tagged jets were required.

Selection Level	Requirement
Level 1	≥ 2 jets, 2 OS-SF leptons
Level 2	≥ 2 b -tagged jets
Level 3	$ m_{\ell\ell} - m_Z < 10$ GeV
Level 4	p_T (Z candidate) < 200 GeV

Table 4.4: $Z + b\bar{b}$ control region selection.

E_T^{miss} lower than 50 GeV would bring the $Z + b\bar{b}$ and total background ratio to 78%. However, bringing a variable to the benchmark selection that is not used in either the signal region nor the other control region is something rather cumbersome, and this idea was dropped. The next idea was to include a cut in the H_T of jets. Cutting values lower than 200 GeV would bring the ratio to 65%, and cutting values lower than 300 GeV would get the ratio at 61%. Even though this slightly improves the ratio, it has a toll in total event statistics, without significantly improving the control region. Other unsuccessful tries were made, such as using the ΔR between the Z candi-

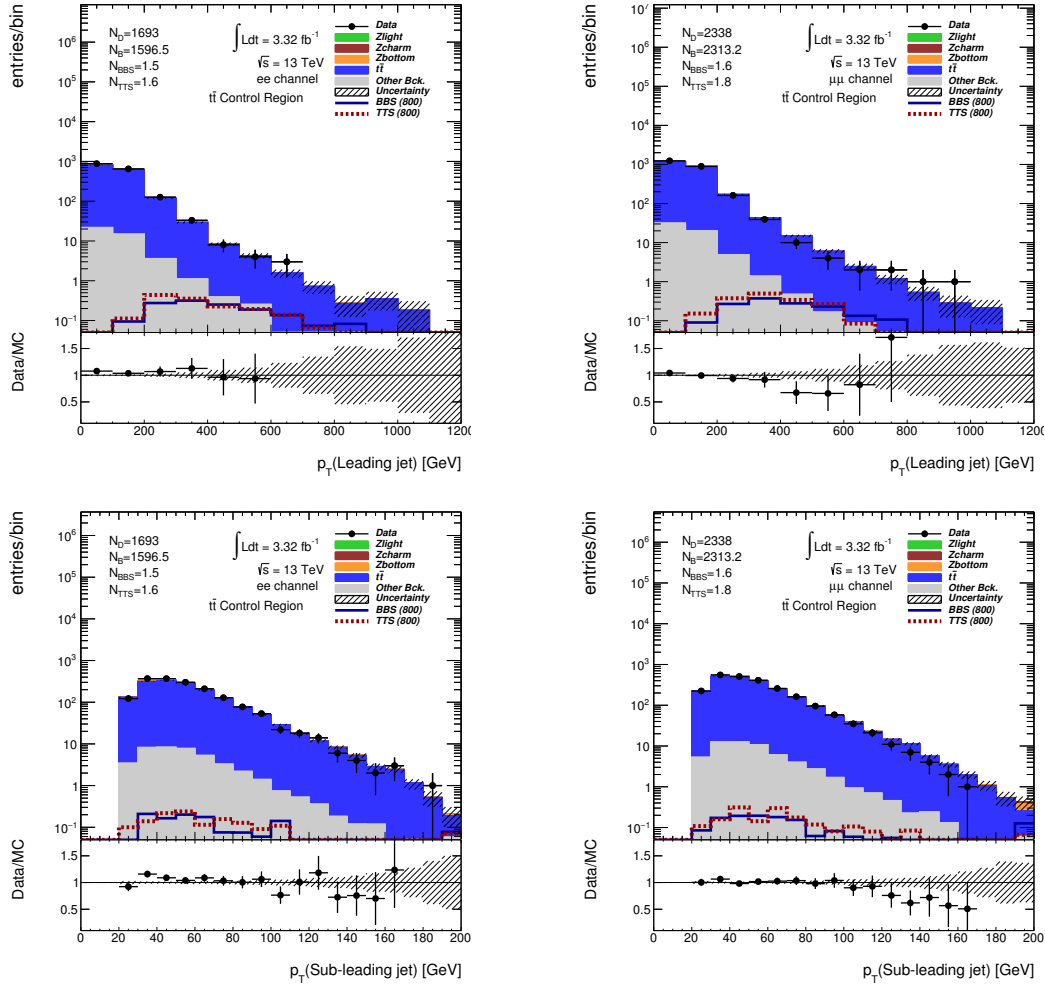


Figure 4.15: The distribution of the leading jet p_T is shown on top and sub-leading jet p_T on the bottom. The electron channel is on the left and muon channel on the right. At least 2 jets, 1 pair of OS-SF leptons 10 GeV outside the Z mass, at least 2 b -tagged jets were required.

date leptons, expecting that they would be closer together when coming from $Z + b\bar{b}$ events than from $t\bar{t}$ events. No significant differences between backgrounds were found, even when boosting to the Z candidate center of mass (These distributions can be seen in Figure 4.24). So the decision was to rely on the good $t\bar{t}$ isolation on its respective control region, and keep the $Z + b\bar{b}$

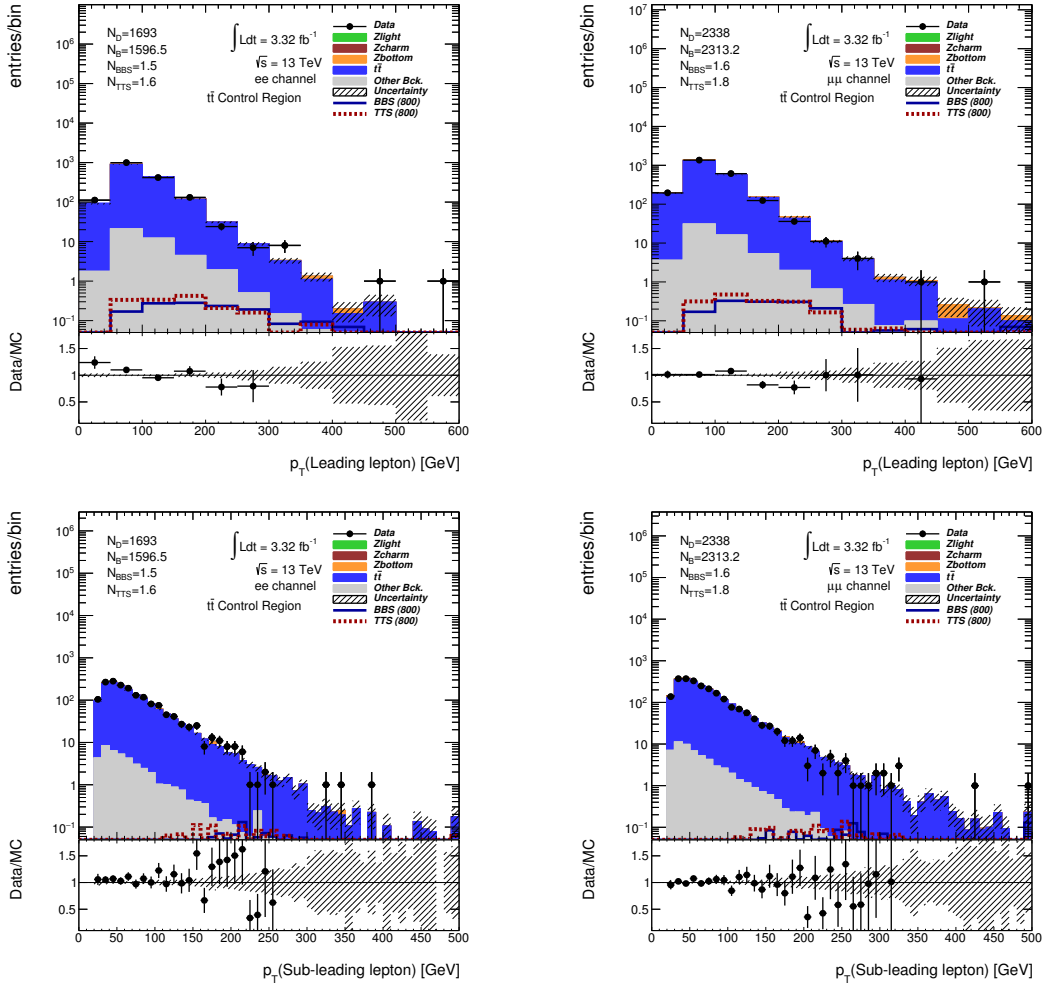


Figure 4.16: The distribution of the leading jet p_T is shown on top and sub-leading jet p_T on the bottom. The electron channel is on the left and muon channel on the right. At least 2 jets, 1 pair of OS-SF leptons 10 GeV outside the Z mass, at least 2 b -tagged jets were required.

control region benchmark as it is.

It is important to point out that the differences seen in the low E_T^{miss} region from Figure 4.23, and the low ΔR between Z boson candidate leptons in the laboratory frame of reference seen in Figure 4.24 are probably due to non-prompt or fake leptons. Most fake electrons are originated from

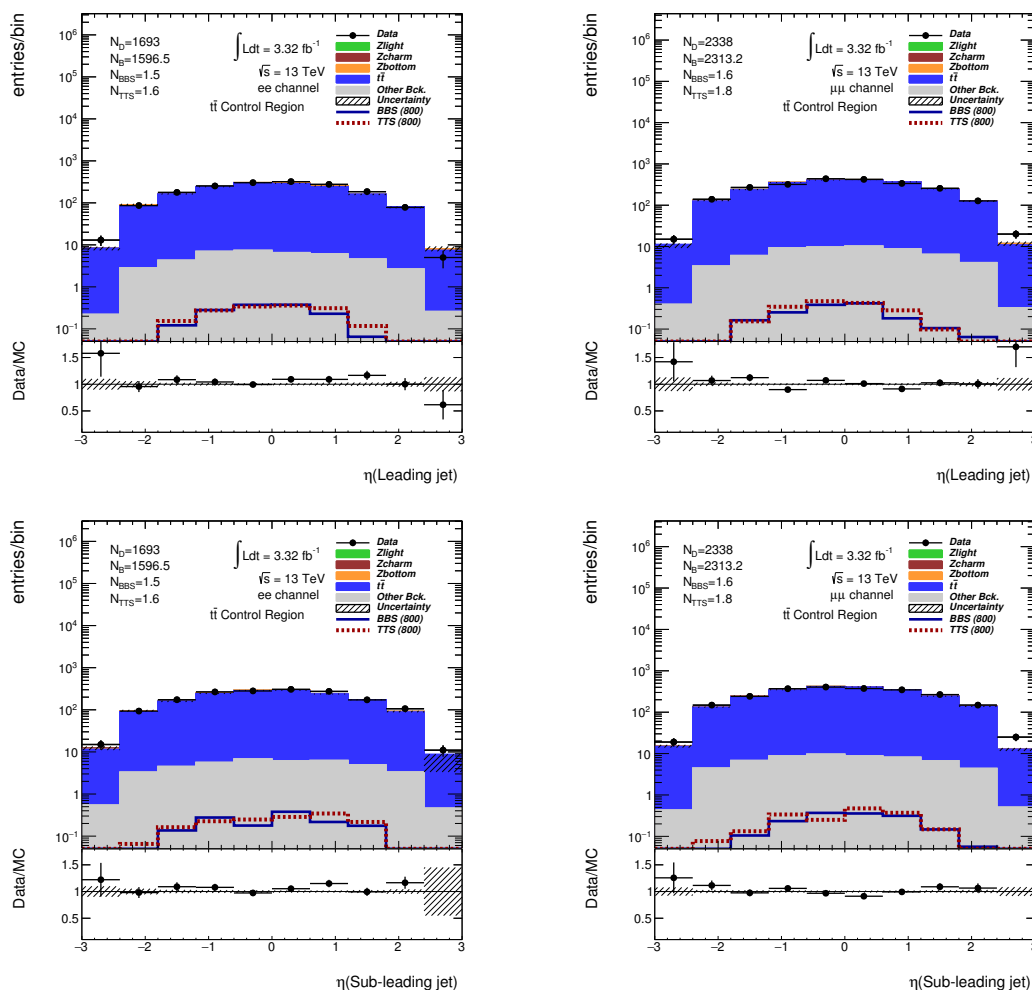


Figure 4.17: The distribution of the leading jet η is shown on top and sub-leading jet η on the bottom. Electron channel is on the left and muon channel on the right. At least 2 jets, 1 pair of OS-SF leptons 10 GeV outside the Z mass, at least 2 b -tagged jets were required.

semileptonic decays of b and c quarks, from photon conversions and jets with large electromagnetic energy. Fake muons are mostly originated also from c and b quarks decaying semileptonically, but also from charged hadrons and punch-through particles (particles that transverse detector parts) coming from high-energy hadronic showers reaching the MS. [86]

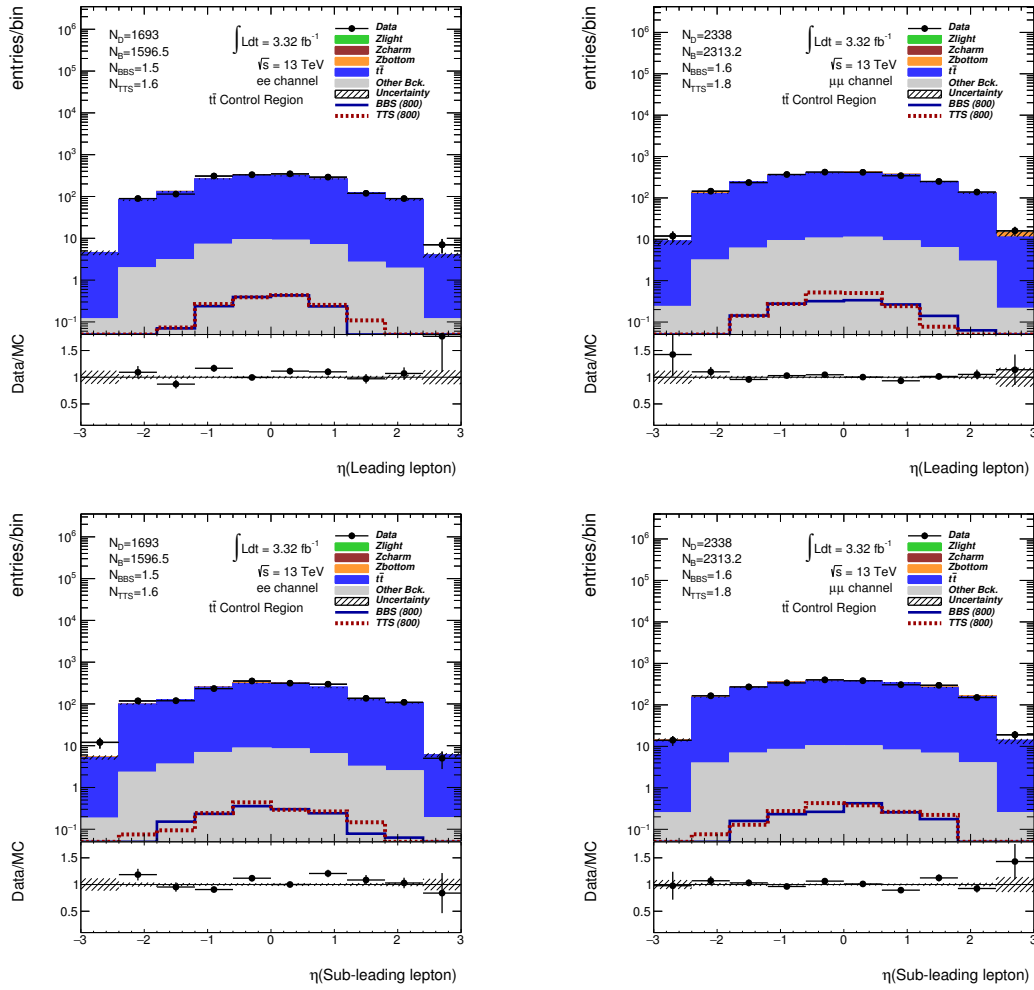


Figure 4.18: The distribution of the leading lepton η is shown on top and sub-leading lepton η on the bottom. The electron channel is on the left and muon channel on the right. At least 2 jets, 1 pair of OS-SF leptons 10 GeV outside the Z mass, at least 2 b -tagged jets were required.

Multiplicity of jets and b -tagged jets is shown in Figure 4.25. MC doesn't seem to perfectly describe data, the b -tagged jet multiplicity distribution in particular, as was seen in the $t\bar{t}$ control region. The same statement made when presenting this distribution in the $t\bar{t}$ control region can be made for the $Z + b\bar{b}$ control region. Figure 4.26 and Figure 4.29 show the p_T distribution

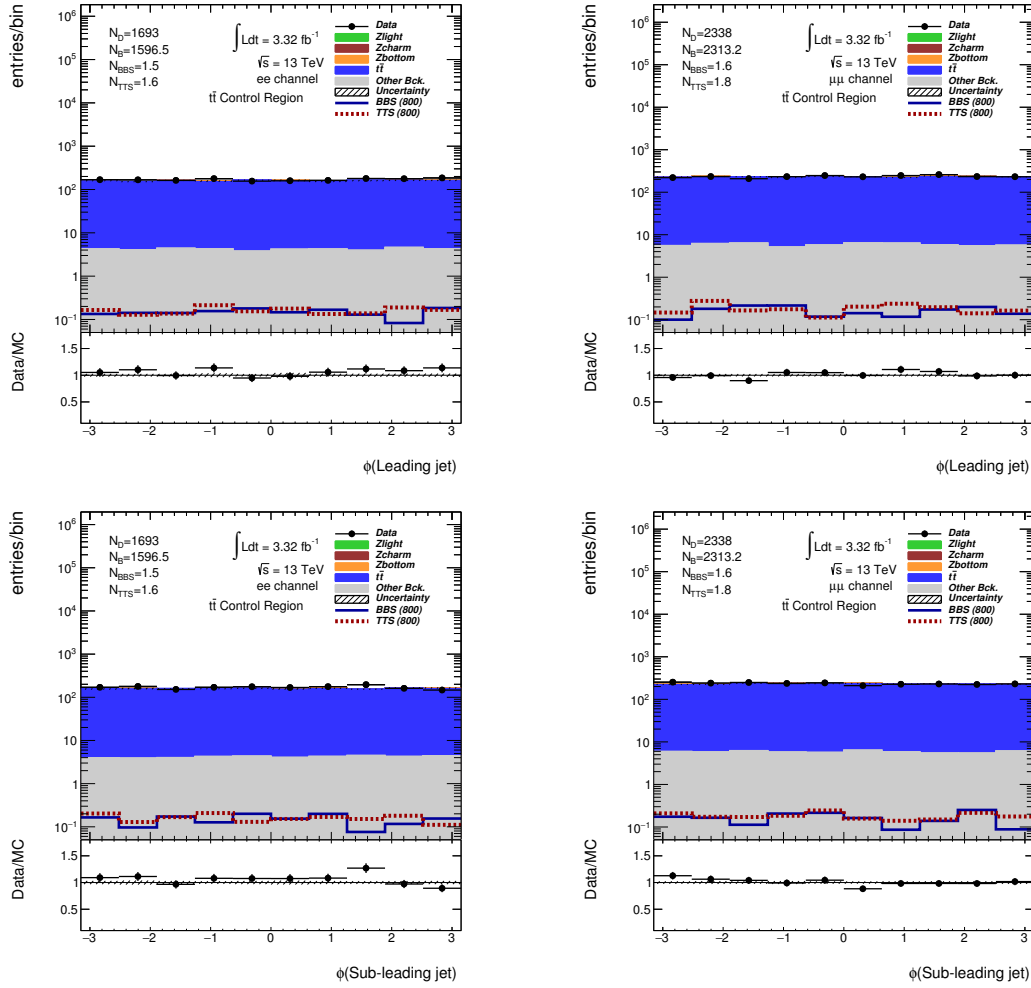


Figure 4.19: The distribution of the leading jet ϕ is shown on top and sub-leading jet ϕ on the bottom. The electron channel is on the left and muon channel on the right. At least 2 jets, 1 pair of OS-SF leptons 10 GeV outside the Z mass, at least 2 b -tagged jets were required.

of jets and leptons respectively. High p_T values have low statistics and the agreement between data and MC is not as good as in the lower values. The distributions of jets and leptons η are shown, respectively, in Figure 4.28 and 4.29. Figure 4.8 and 4.9 show the ϕ distributions of jets and leptons, respectively. This angular distributions have fair data and MC agreement.

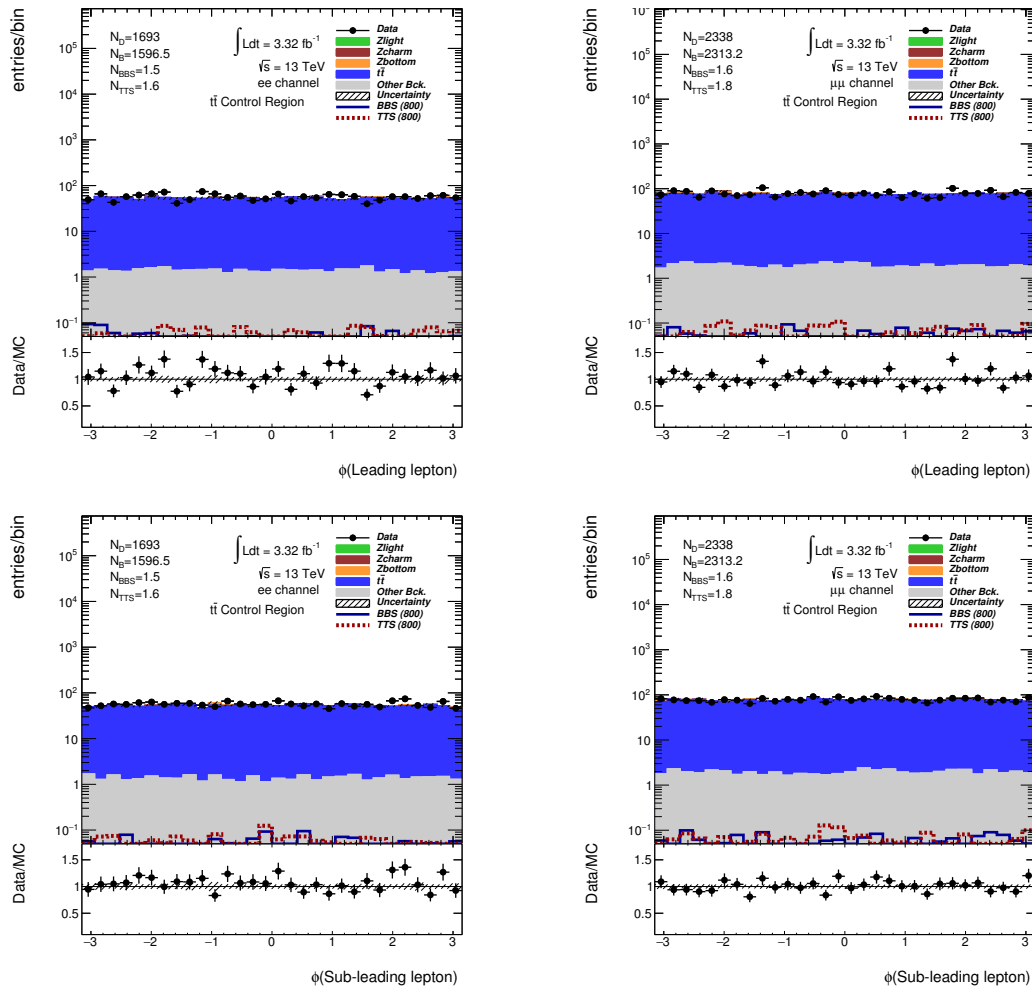


Figure 4.20: The distribution of the leading lepton ϕ is shown on top and sub-leading lepton ϕ on the bottom. The electron channel is on the left and muon channel on the right. At least 2 jets, 1 pair of OS-SF leptons 10 GeV outside the Z mass, at least 2 b -tagged jets were required.

The Z candidate mass distribution can be seen in Figure 4.32, where MC seems to do a fair description of data. Figure 4.33 shows the discriminant variable after this control region selection is applied. The slight issue with normalization seen in this distribution is probably going to be softened by the fit, due to the nature of our discriminant variable. As we are looking

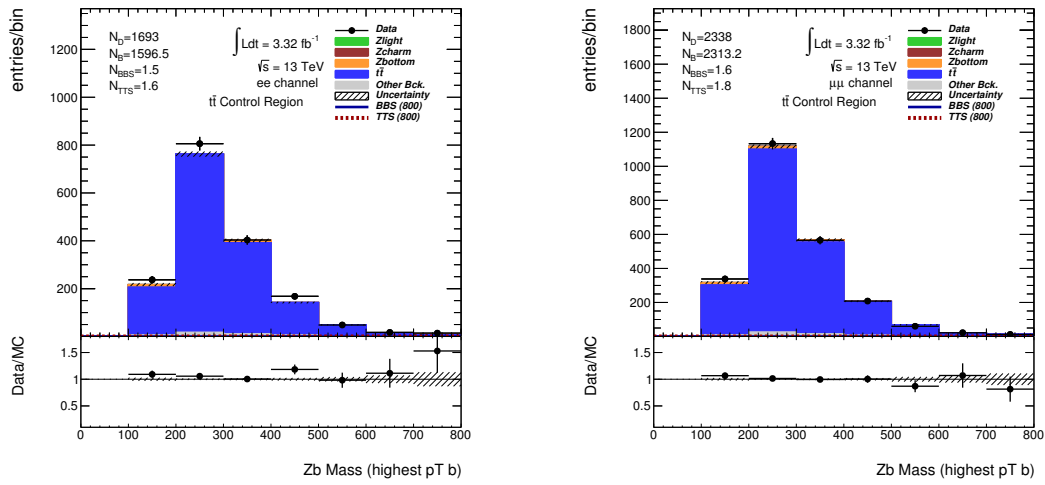


Figure 4.21: The mass of the Zb system in the electron channel is shown on the left, and the muon channel on the right. At least 2 jets, a pair of OS-SF leptons, at least 2 b -tagged jets and $|m_{\ell\ell} - m_Z|$ higher than 10 GeV were required.

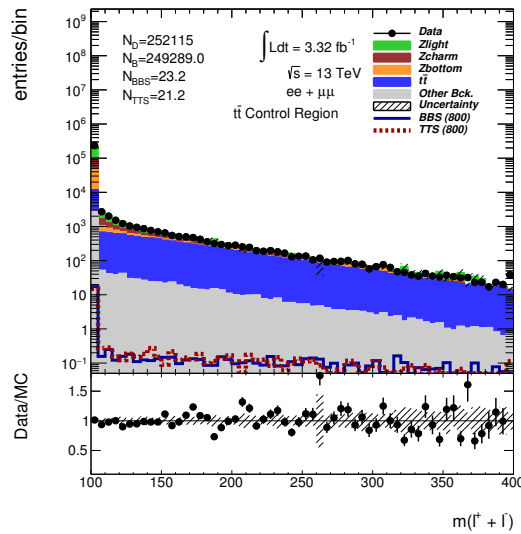


Figure 4.22: The mass of the Z candidate outside the peak is shown, where the $t\bar{t}$ control region is defined.

	ee	$\mu\mu$
BBS (800)	0.3 ± 0.0	0.3 ± 0.1
TTS (800)	0.3 ± 0.0	0.3 ± 0.0
Z+light jets	0.0 ± 0.0	-1.3 ± 1.9
$Z + bb$	620.4 ± 54.9	924.3 ± 38.3
$Z + cc$	21.8 ± 9.4	41.7 ± 11.2
$t\bar{t}$	397.4 ± 5.7	601.4 ± 7.2
Other Bck.	37.9 ± 1.9	54.4 ± 2.5
Total bkg.	1077.5 ± 56.0	1620.6 ± 40.7
Data	1254	1930

Table 4.5: Yields for $Z + bb$ control region after all the selection is applied. Uncertainties are statistics only.

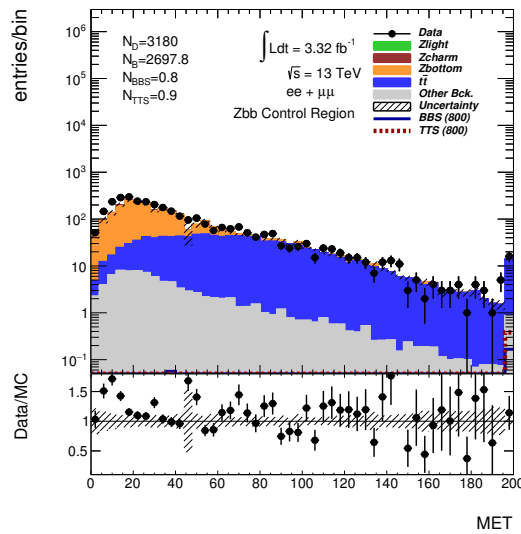


Figure 4.23: The Missing Transverse Energy in $Z + bb$ control region is shown. At least 2 jets, 1 pair of OS-SF leptons within 10 GeV of Z mass, at least 2 b -tagged jets and p_T of Z candidate lower than 200 GeV required.

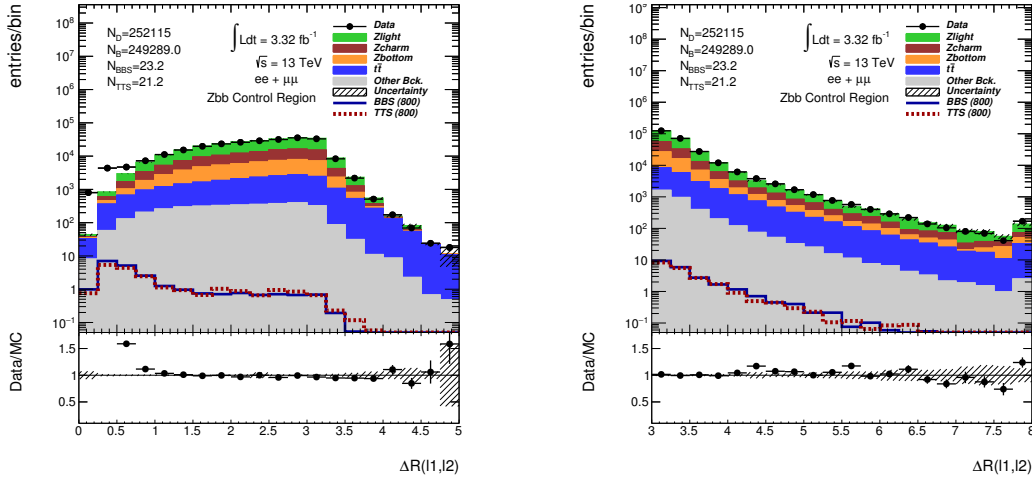


Figure 4.24: The distribution of ΔR between the Z candidate leptons, before the boost to the Z center of mass is shown on the left, and after the boost is shown on the right. At least 2 jets and a pair of OS-SF leptons required.

for a resonance, the fit will rely on shape differences, making normalization differences as those seen in Figure 4.33 less problematic after the fit is done. All plots show the not so good $Z + b\bar{b}$ isolation, as seen in Table 4.5.

In order to see if we have a good heavy flavor description given by our MC, we look at the $mv2c20$, the variable used to determine if a jet is b -tagged or not. This variable should behave differently for the different jet flavors, and therefore is a good variable to check. The plot for the leading and sub-leading jet is shown in Figure 4.34. A fair data/MC agreement is seen, and no obvious problem with our heavy flavor description is seen. Even though this is not a definitive test, it is a good check to determine if there is an obvious problem with the MC description of the heavy flavor component of the background in the analysis. However, this test would be more powerful if a continuous calibration was used.

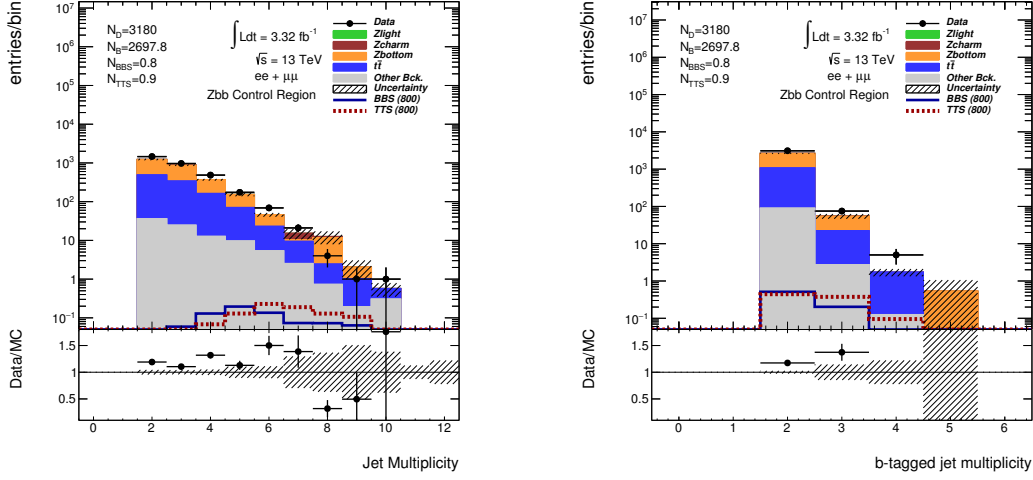


Figure 4.25: The multiplicity of jets is shown on the left, and the multiplicity of b -tagged jets is shown on the right. At least 2 jets, a pair of OS-SF leptons, at least 2 b -tagged jets, $|m_{\ell\ell} - m_Z|$ lower than 10 GeV and p_T of the Z candidate lower than 200 GeV were required.

4.3 Results

Having defined the signal and control regions, expected 95% C.L. upper limits on VLQ mass where set using the CL_S method [87, 88]. Defining two statistical hypothesis: background-only (the null-hypothesis) and signal plus background (the test-hypothesis), we can define a parameter μ , the signal strength modifier, that varies between 0 and 1, with 0 recovering the null-hypothesis and 1 recovering the test-hypothesis. In the context of this analysis, the null-hypothesis is SM only, and the test-hypothesis includes VLQ as signal. With that, we can use p_μ as the p-value¹ of a given signal strength μ . This p-value can be converted to Gaussian significance. The particle physics convention is to exclude $p_\mu < 0.05$, which is referred as 95% C.L.

¹p-value is the probability of finding a given test statistics equally likely or more extreme than the test-statistics(q_μ) being used. It is given by $p_\mu = \int_{q_{\mu,obs}}^{\infty} f(q_\mu|\mu)dq_\mu$, with $q_{\mu,obs}$ being the observed value with data of the test-statistics.

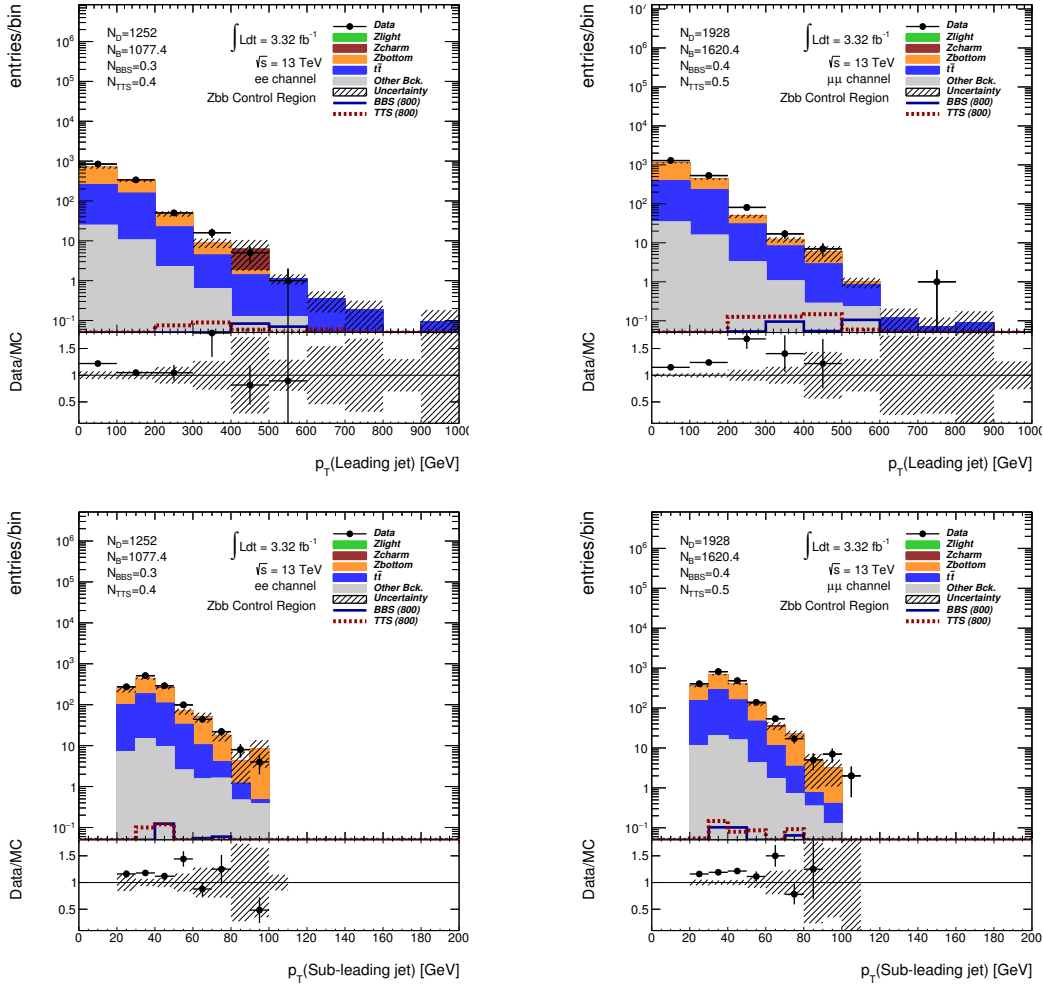


Figure 4.26: The distribution of the leading jet p_T is shown on top and sub-leading jet p_T on the bottom. The electron channel is on the left and muon channel on the right. At least 2 jets, a pair of OS-SF leptons, at least 2 b -tagged jets, $|m_{\ell\ell} - m_Z|$ lower than 10 GeV and p_T of the Z candidate lower than 200 GeV were required.

Given the p_μ , the CL_S value is defined as:

$$CL_S \equiv \frac{P_\mu}{1 - p_0}, \quad (4.1)$$

with p_0 being the background-only hypothesis p-value. This prevents the exclusion of signal in a downward fluctuation, given that $1-p_0$ will also be

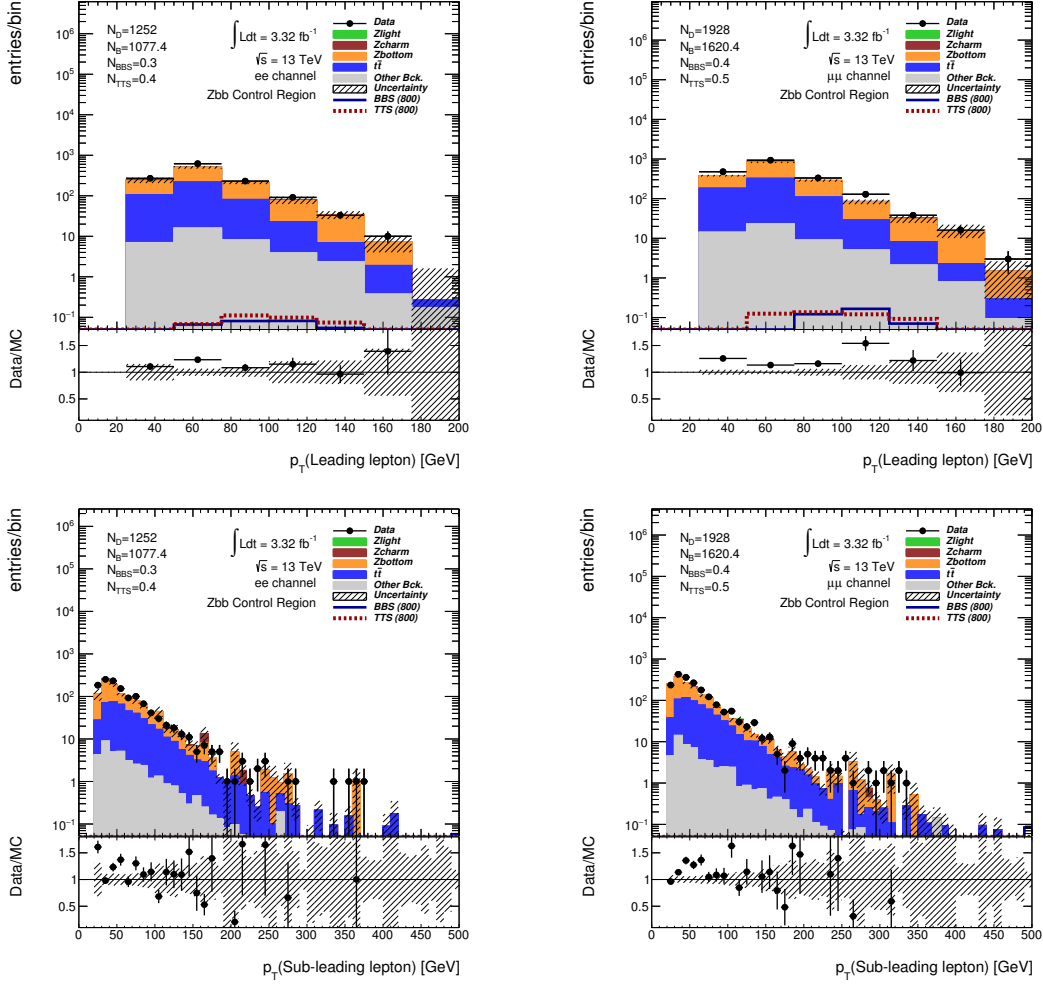


Figure 4.27: The distribution of the leading lepton p_T is shown on top and sub-leading lepton p_T on the bottom. The electron channel is on the left and muon channel on the right. At least 2 jets, a pair of OS-SF leptons, at least 2 b -tagged jets, $|m_{\ell\ell} - m_Z|$ lower than 10 GeV and p_T of the Z candidate lower than 200 GeV were required.

small, thus creating a conservative method. The test-statistics used is a log-likelihood ration, given by $-2\ln\lambda(\mu)$, with $\lambda(\mu)$ being the significance, given by:

$$\lambda(\mu) = \frac{\mathcal{L}(\mu, \theta_\mu)}{\mathcal{L}(\hat{\mu}, \hat{\lambda})}. \quad (4.2)$$

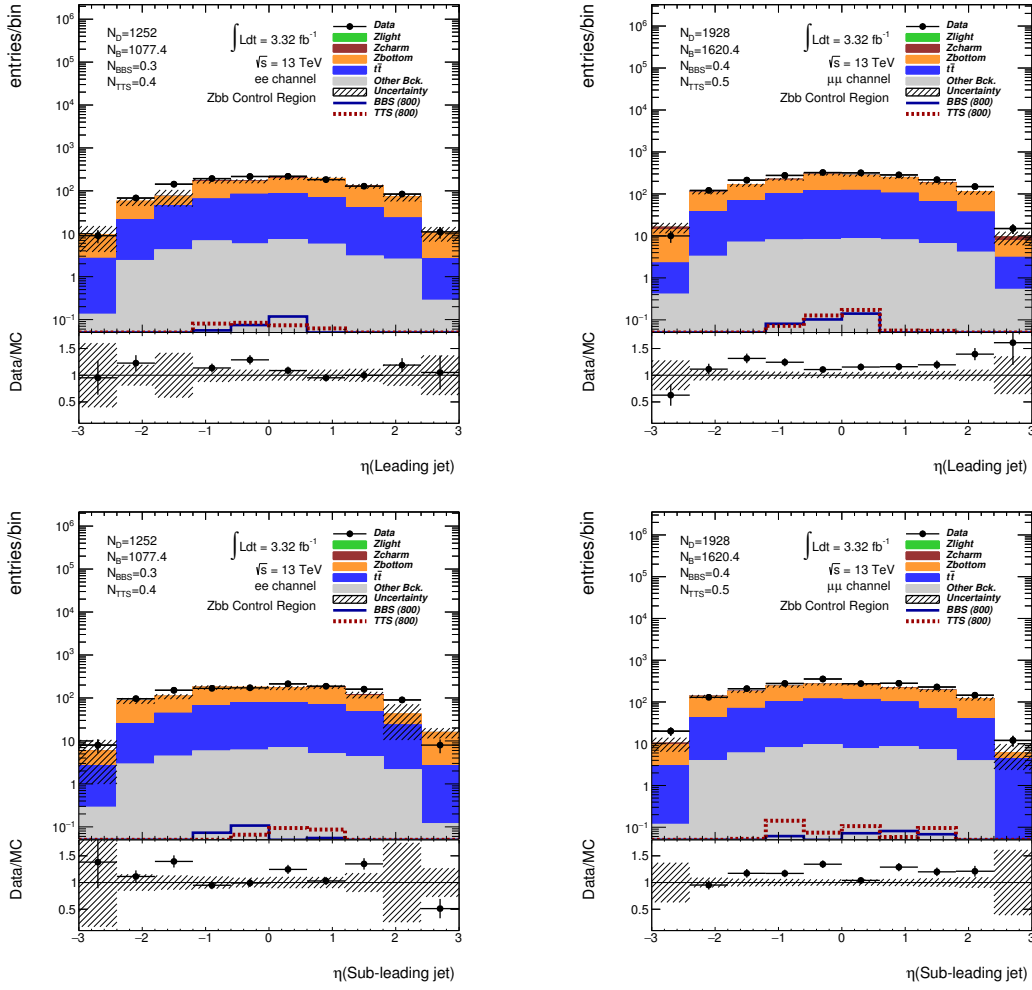


Figure 4.28: The distribution of the leading jet η is shown on top and sub-leading jet η on the bottom. The electron channel is on the left and muon channel on the right. At least 2 jets, a pair of OS-SF leptons, at least 2 b -tagged jets, $|m_{\ell\ell} - m_Z|$ lower than 10 GeV and p_T of the Z candidate lower than 200 GeV were required.

In this case, θ are the nuisance parameters of the test-statistics, and \mathcal{L} is the likelihood, that in this case is a function of Poissonian distributions, and a Probability Density Function for the nuisance parameters. The ratio of the conditional likelihood, for a given μ and the globally maximized likelihood,

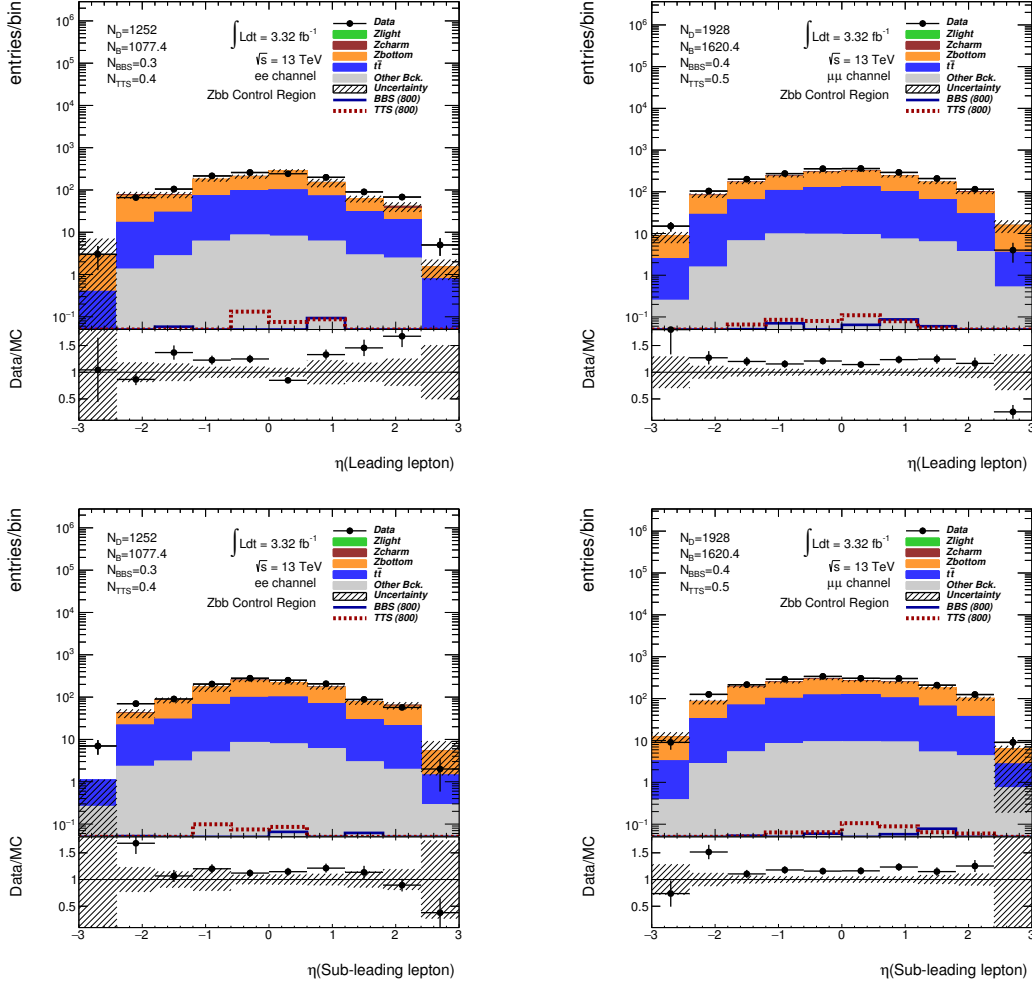


Figure 4.29: The distribution of the leading lepton η is shown on top and sub-leading lepton η on the bottom. The electron channel is on the left and muon channel on the right. At least 2 jets, a pair of OS-SF leptons, at least 2 b -tagged jets, $|m_{\ell\ell} - m_Z|$ lower than 10 GeV and p_T of the Z candidate lower than 200 GeV were required.

defines the significance that serves as the test-statistics for the limit setting machinery.

Figure 4.35 shows the cross-section upper limits as a function of the VLQ mass. The green and yellow bands represent 1 and 2σ uncertainties, respec-

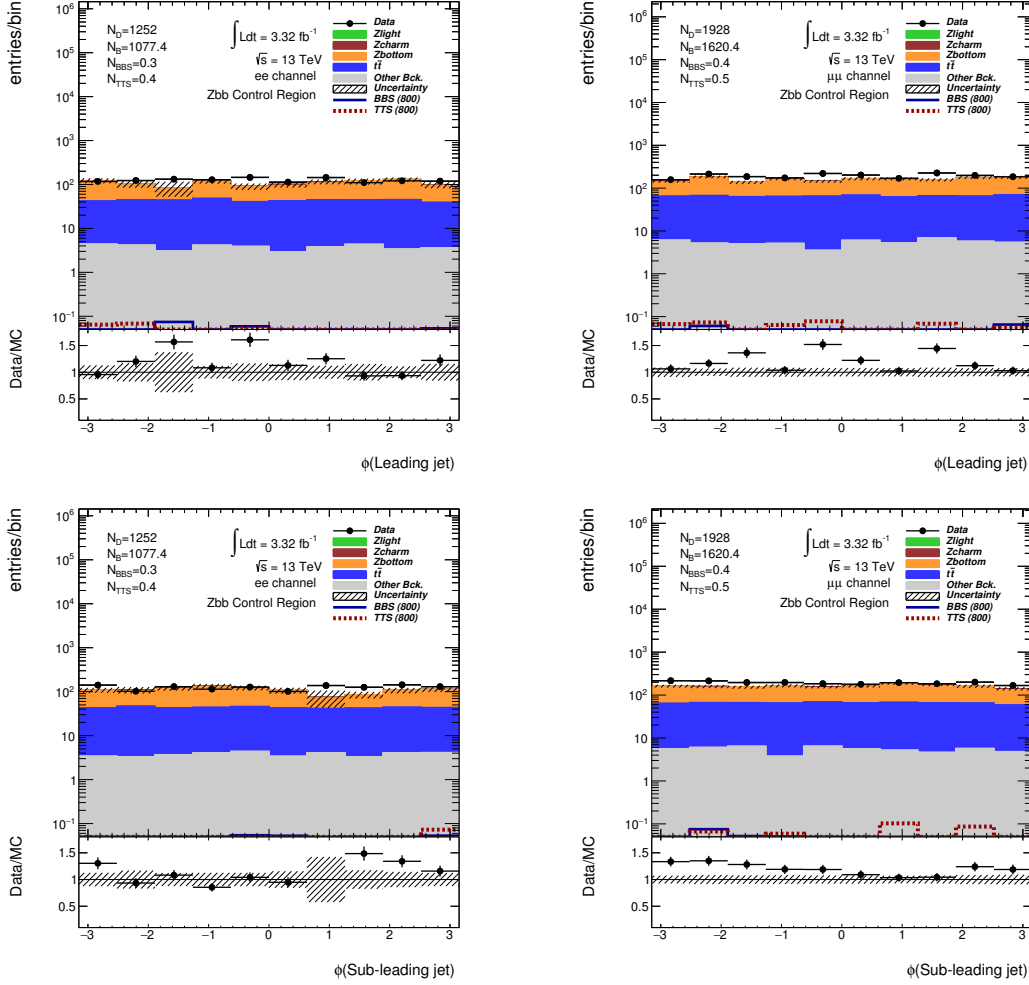


Figure 4.30: The distribution of the leading jet ϕ is shown on top and sub-leading jet ϕ on the bottom. The electron channel is on the left and muon channel on the right. At least 2 jets, a pair of OS-SF leptons, at least 2 b -tagged jets, $|m_{\ell\ell} - m_Z|$ lower than 10 GeV and p_T of the Z candidate lower than 200 GeV were required.

tively. The theoretical cross-section is represented by the red band. Limits are derived for vector-like B and T , for singlet and doublet hypothesis. For the vector-like T , the doublet considered is (T, B) and for the vector-like B the doublet considered is (B, Y) , because the neutral decay of the vector-like B in

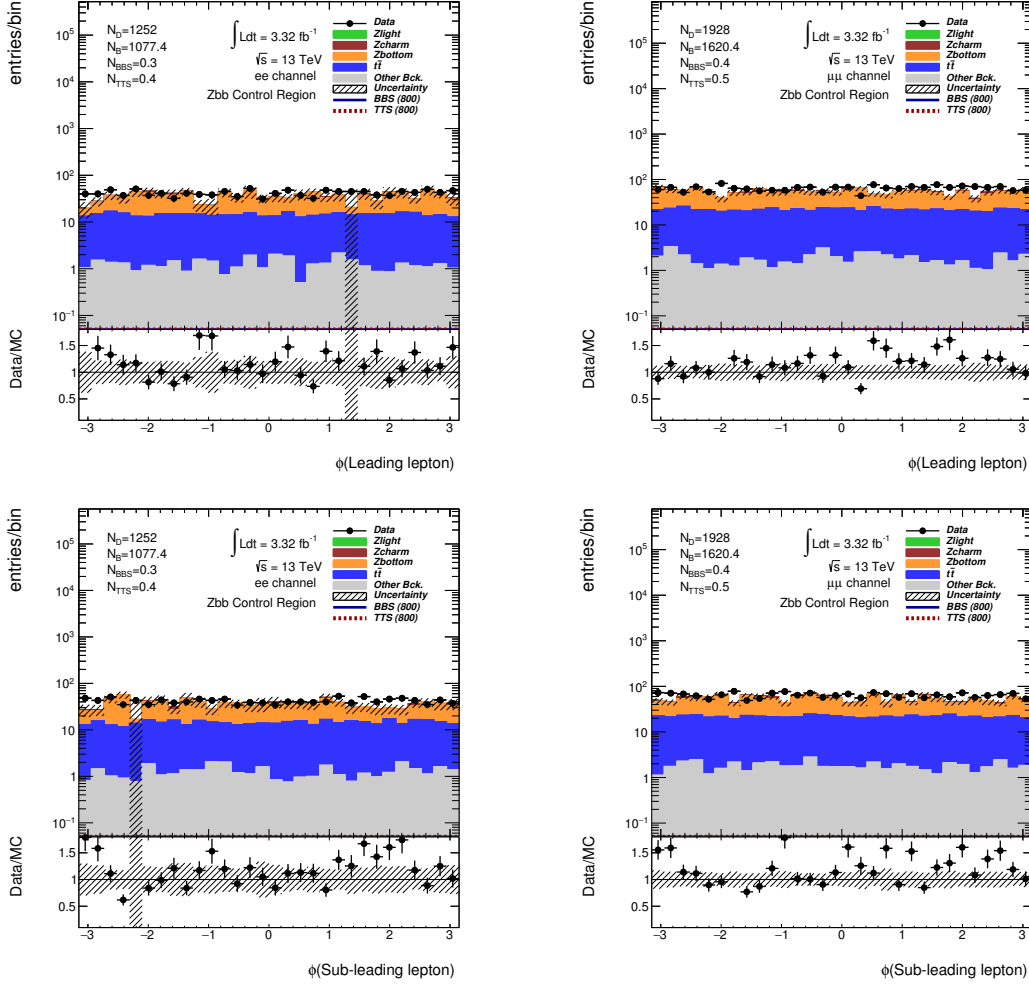


Figure 4.31: The distribution of the leading lepton ϕ is shown on top and sub-leading lepton ϕ on the bottom. The electron channel is on the left and muon channel on the right. At least 2 jets, a pair of OS-SF leptons, at least 2 b -tagged jets, $|m_{\ell\ell} - m_Z|$ lower than 10 GeV and p_T of the Z candidate lower than 200 GeV were required.

the (T, B) doublet is highly suppressed (this was discussed in Sub-section 2.2.2). The expected mass limits are summarized in Table 4.6.

From Table 4.6 we see the improvement from the first phase of LHC operation, as was expected by the increase in center of mass energy in the

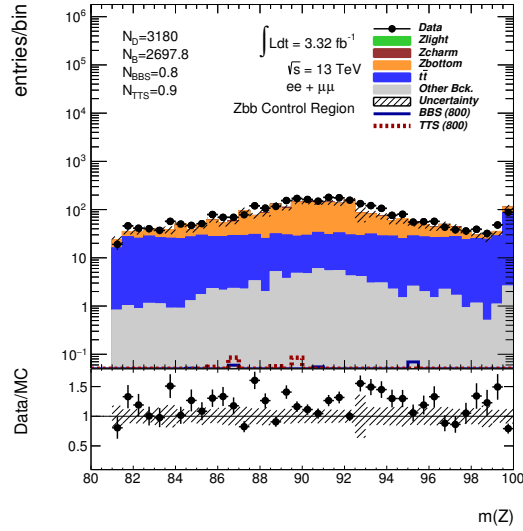


Figure 4.32: The mass of the Z candidate is shown. At least 2 jets, a pair of OS-SF leptons, at least 2 b -tagged jets, $|m_{\ell\ell} - m_Z|$ lower than 10 GeV and p_T of the Z candidate lower than 200 GeV were required.

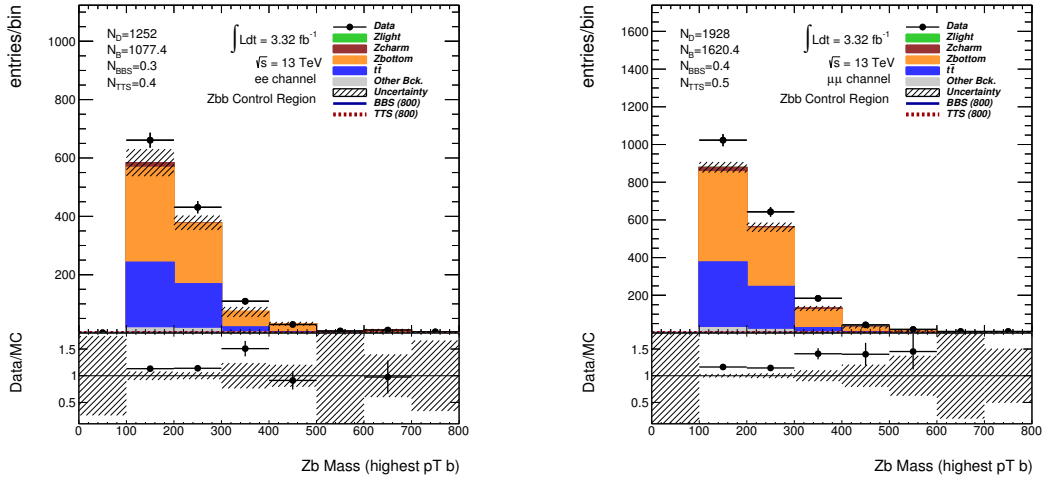


Figure 4.33: The mass of the Zb system in the electron channel is shown on the left, and muon channel on the right. At least 2 jets, a pair of OS-SF leptons, at least 2 b -tagged jets, $|m_{\ell\ell} - m_Z|$ lower than 10 GeV and p_T of the Z candidate lower than 200 GeV were required.

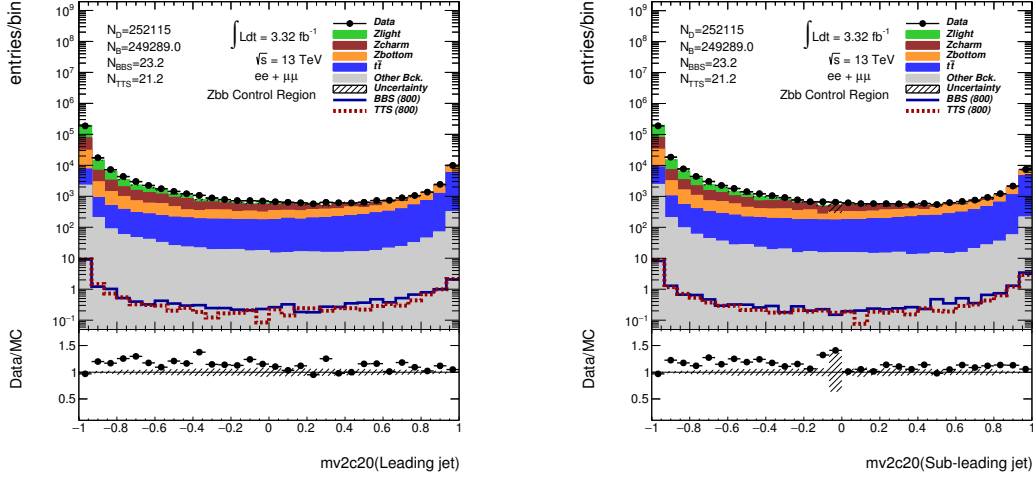


Figure 4.34: The distribution of the $mv2c20$ tagging algorithm for the leading jet is shown on the left, and sub-leading jet on the right. At least 2 jets and 1 OS-SF lepton pair is required.

Quark	Expected mass limits (GeV)			
	Singlet		Doublet	
	8 TeV	13 TeV	8 TeV	13 TeV
$B\bar{B}$	670	766	755	873
$T\bar{T}$	625	687	720	797

Table 4.6: Expected mass limits at 95% C.L. for vector-like T and B , for the singlet and doublet hypothesis, comparing current results with results from the first phase of operation of the LHC.

proton-proton collisions, and consequent increase in the signal cross-section. It should be noted that the current values only include statistical errors. The higher limits by the doublet hypothesis are expected, given that the doublet hypothesis has a bigger branching ratio of the Z decay than the singlet hypothesis, as can be seen in Figure 2.6. The difference between the B and T quarks is also expected, given that the difference in sensitivity by this

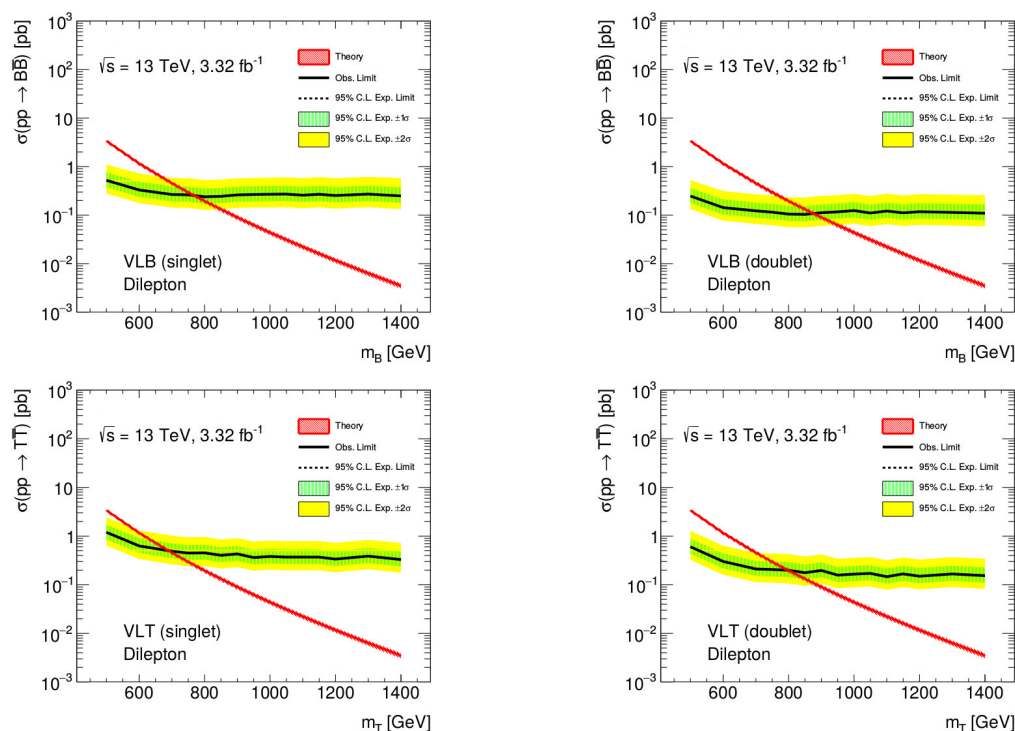


Figure 4.35: The expected upper cross-section limits at 95% CL for vector-like B are shown on top and vector-like T on the bottom. Singlet hypothesis on the left, doublet on the right.

analysis is already known. However, there is the expectation that the tripleton channel can have a better sensibility for the vector-like T , and therefore improve the final limits obtained after the combination of the three different analysis.

Besides upper mass limits, a scan was performed, shown in Figure 4.36, where all the decay modes are considered, and the expected mass limit for each BR is plotted. The plot is shaped as a triangle, with the BR of the decay to the W boson increasing in the x-axis and to the Higgs boson in the y-axis. That leaves the bottom left corner as the most sensible corner in this analysis, as it is the area in the triangle with the biggest BR to the Z boson.

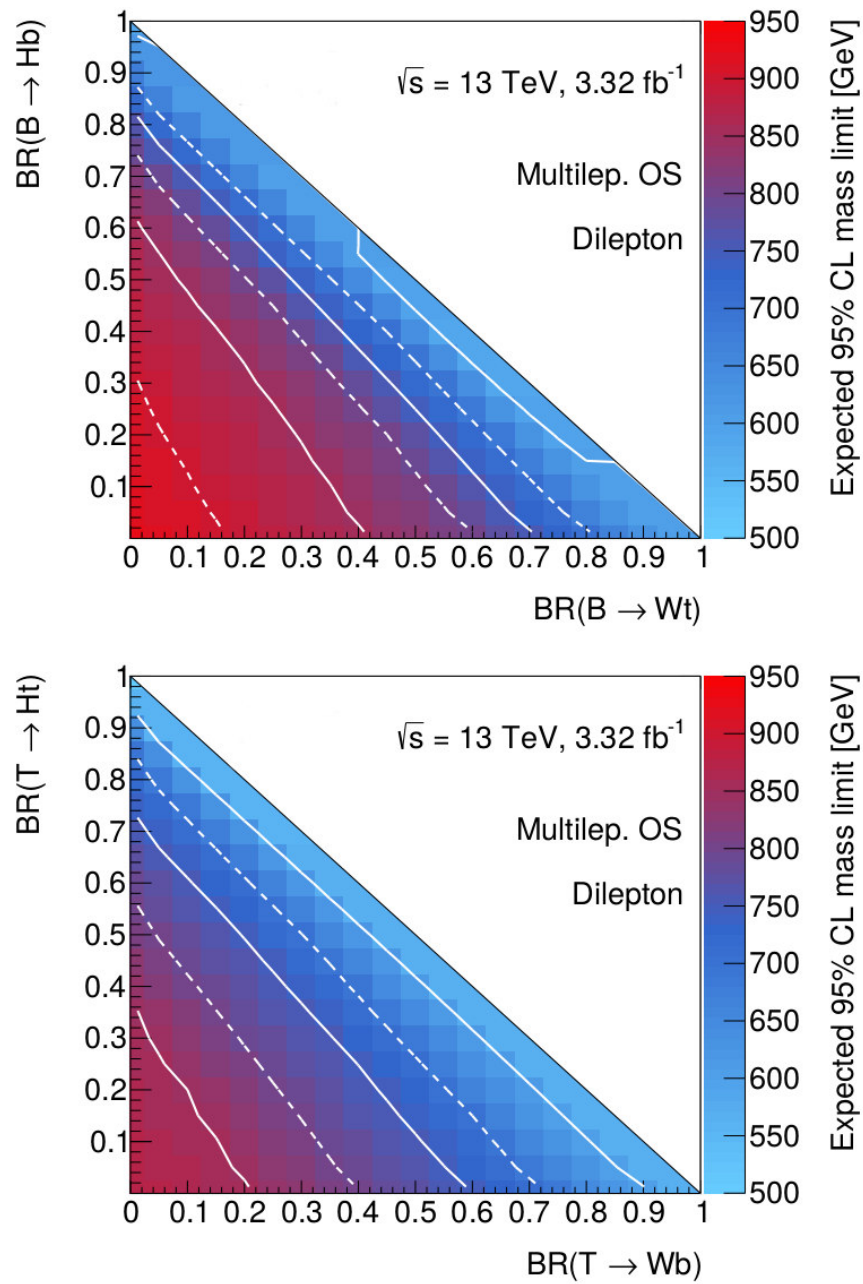


Figure 4.36: The expected mass limits as a function of the BR to the W and H bosons, for the vector-like B are shown on the top and the vector-like T on the bottom, at 95% CL.

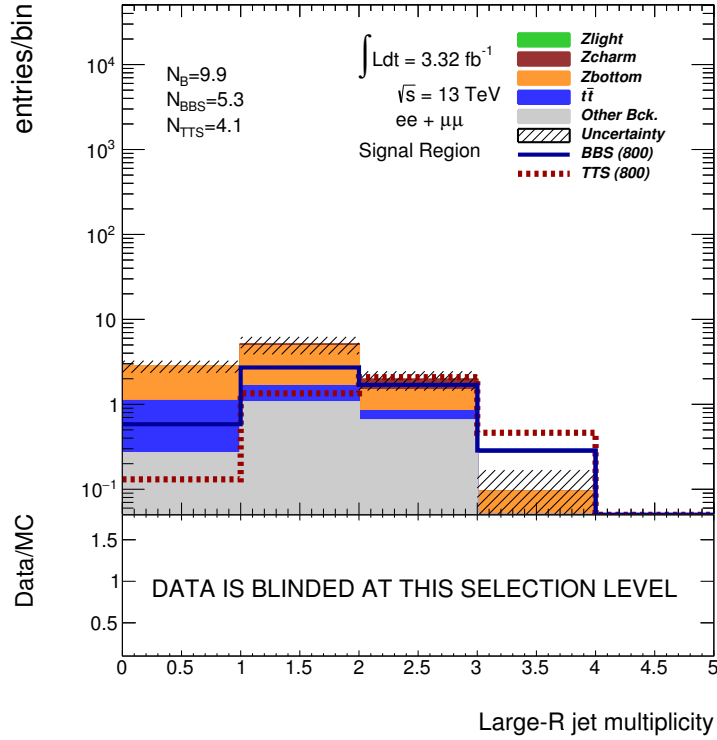


Figure 4.37: The multiplicity of large-R jets is shown, with p_T threshold of 200 GeV. At least 2 jets, 1 pair of OS-SF leptons, at least 2 b -tagged jets, p_T higher than 200 GeV and H_T of jets higher than 700 GeV is required.

4.4 Complementarity with boosted topologies and trilepton channel

VLQ have experimental features such as high jet multiplicity and boosted objects. In this search for pair-produced VLQ decaying through a Z boson, it was necessary to branch out to diverse analysis, with the goal of combining results in the end. The analysis for the pair-produced VLQ are the dilepton resolved analysis, which this text describes; the trilepton channel, that asks for at least three leptons in its final state and the boosted dilepton analysis, with which this analysis still needs to figure out the best way to orthogonal-

	$p_T = 200 \text{ GeV}$		$p_T = 250 \text{ GeV}$		$p_T = 300 \text{ GeV}$		$p_T = 350 \text{ GeV}$		$p_T = 400 \text{ GeV}$	
$B\bar{B}_S$	574.7	713.2	596.6	722.0	624.0	732.2	659.8	737.8	678.2	746.9
$T\bar{T}_S$	<500	614.8	521.1	630.3	570.0	643.2	601.9	654.9	613.3	664.8
$B\bar{B}_D$	708.8	828.2	726.7	832.8	751.0	839.0	764.1	848.5	780.4	855.4
$T\bar{T}_D$	<500	674.6	545.4	712.9	611.8	736.8	654.6	754.3	705.4	768.6

Table 4.7: Expected mass limits for the different large-R jet multiplicities and p_T thresholds. For each p_T threshold, limits with exactly 0 large-R jets is on the left and less than 2 on the right.

ize (note that the orthogonality with the trilepton analysis is immediately assured once exactly two leptons are required by this analysis). Multiplicity of large-R jets is probably the best way to start implementing the cuts necessary to orthogonalize the resolved and boosted dilepton analysis. In this text we define a large-R jet as a jet reconstructed with an anti- k_T algorithm with $R = 1.0$, mass higher than 50 GeV, $|\eta| < 2.0$ and p_T above a certain threshold that is yet to be defined. An overlap removal with electrons is also made. For this, it is required that if the Z boson candidate is reconstructed with electrons, the ΔR between the large-R jet and each electron must be higher than 1.0. So, to start defining the best way to split the multiplicity of large-R jets, the expected mass limits for different scenarios were calculated, and are displayed in Table 4.7.

Looking at Table 4.7 we see that a p_T threshold of 200 GeV brings the expected mass limits to low values, specially if we require only events without large-R jets. However, it is possible that, in compromising this analysis values, a final combination with higher mass limits overall is achieved. To obtain an agreement that is favorable to the final combination a combined study with the boosted topology analysis is required, and will be done in the next steps of the analysis.

The presence of an analysis dedicated to the trilepton final state also covers the slight lack of sensitivity to the vector-like T that the discriminant variable of the dilepton analysis has. In that regard, a trilepton channel is

more suited to define a discriminant variable sensitive to the vector-like T . The choice for the first phase of operation of the LHC was the H_T of jets and leptons, and so far it is the choice for the second phase of operation of the LHC.

Chapter 5

Conclusions

As was previously stated, the Standard Model of Particle Physics is able to describe fundamental particles and their interactions in agreement with experimental data. However, it does not provide answers to some questions. In order to tackle those problems various models were built, with vector-like quarks being a prediction made in some of these. The existence of these quarks can only be verified or excluded (at least up to some energy scale) with experimental results, and the goal of this analysis is to lay the basis for the data to be used and to obtain results. For that, data collected by the ATLAS experiment, from proton-proton collisions made in the LHC was used.

In the present thesis a strategy built upon the one defined at the first phase of operation of the LHC was implemented and optimized using expected mass limits and making the best to remove irreducible background while preserving statistics after all the cuts are applied and making a compromise between the vector-like B and T , due to the different sensitivity this analysis has to both quarks. Control regions of the main backgrounds were defined and studied, and a strategy to the fit was laid out. Expected mass limits were obtained, improving the ones previously established at a center of mass energy of 8 TeV. These limits, for vector-like T are 687 and 797 GeV, for the singlet and doublet hypothesis, respectively. As for the vector-like

B , the singlet hypothesis expected mass limit is 766 GeV, and the doublet hypothesis mass limit is 873 GeV. However, these limits are expected to change, once the systematic uncertainties are included, and the luminosity and Monte Carlo statistics are improved.

Studies to orthogonalize this analysis with the boosted topology analysis are being developed at the moment by the respective research groups, allowing for a combination between the two analyses, and, afterwards, with the trilepton channel as well. The combination of the different analyses and their different sensitivities should allow for better overall results than a more inclusive analysis would.

At the time this text is being written, the implementation of systematic uncertainties is underway. With such implementation, a fit with systematic uncertainties is in order, allowing to analyze their behavior and further study them individually, if needed, and derive mass limits with systematic uncertainties added to the statistical uncertainty. An upgrade to the 2016 data is also an important step, as luminosity is being recorded at a record rate by the ATLAS experiment, as illustrated by Figure 5.1. The increase in luminosity and the upgrade to the latest Monte Carlo samples, with higher statistics and improved scale factors, could improve the discriminant variable distributions, that present fluctuations due to the limited number of Monte Carlo events after each selection is applied. This fluctuations propagate to fluctuations in the mass limits, causing the risk of the analysis being optimized on them.

After the systematic uncertainties are implemented and all analysis are orthogonal, unblinding should be the next step, allowing to determine if an excess from the Standard Model expectation was found or, if that is not the case, derive observed mass limits, combining both dilepton and the trilepton analysis.

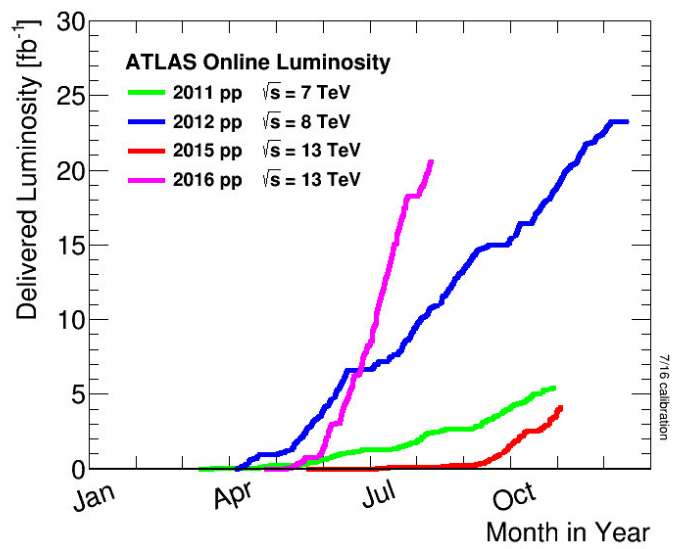


Figure 5.1: The cumulative luminosity versus day delivered to the ATLAS detector in proton-proton collisions is shown. [89]

Bibliography

- [1] K. A. Olive et al. Review of Particle Physics. *Chin. Phys.*, C38:090001, 2014.
- [2] David J. Gross and Frank Wilczek. Ultraviolet behavior of non-abelian gauge theories. *Phys. Rev. Lett.*, 30:1343–1346, Jun 1973.
- [3] H. Fritzsch, M. Gell-Mann, and H. Leutwyler. Advantages of the color octet gluon picture. *Physics Letters B*, 47(4):365 – 368, 1973.
- [4] H. David Politzer. Reliable Perturbative Results for Strong Interactions? *Phys. Rev. Lett.*, 30:1346–1349, Jun 1973.
- [5] Steven Weinberg. A Model of Leptons. *Phys. Rev. Lett.*, 19:1264–1266, Nov 1967.
- [6] Sheldon L. Glashow. Partial-symmetries of weak interactions. *Nuclear Physics*, 22(4):579 – 588, 1961.
- [7] Abdus Salam. Weak and Electromagnetic Interactions. *Conf. Proc.*, C680519:367–377, 1968.
- [8] F. Englert and R. Brout. Broken Symmetry and the Mass of Gauge Vector Mesons. *Phys. Rev. Lett.*, 13:321–323, Aug 1964.
- [9] P.W. Higgs. Broken symmetries, massless particles and gauge fields. *Physics Letters*, 12(2):132 – 133, 1964.

-
- [10] G. S. Guralnik, C. R. Hagen, and T. W. B. Kibble. Global Conservation Laws and Massless Particles. *Phys. Rev. Lett.*, 13:585–587, Nov 1964.
- [11] C. S. Wu, E. Ambler, R. W. Hayward, D. D. Hoppes, and R. P. Hudson. Experimental Test of Parity Conservation in Beta Decay. *Phys. Rev.*, 105:1413–1415, Feb 1957.
- [12] G. Arnison et al. Experimental Observation of Isolated Large Transverse Energy Electrons with Associated Missing Energy at $s^{**}(1/2) = 540\text{-GeV}$. *Phys. Lett.*, B122:103–116, 1983. [611(1983)].
- [13] M. Banner et al. Observation of Single Isolated Electrons of High Transverse Momentum in Events with Missing Transverse Energy at the CERN anti-p p Collider. *Phys. Lett.*, B122:476–485, 1983.
- [14] M. Altmann et al. Complete results for five years of GNO solar neutrino observations. *Phys. Lett.*, B616:174–190, 2005.
- [15] Bruce T. Cleveland et al. Measurement of the Solar Electron Neutrino Flux with the Homestake Chlorine Detector. *The Astrophysical Journal*, 496(1):505, 1998.
- [16] K. Eguchi et al. First results from KamLAND: Evidence for reactor anti-neutrino disappearance. *Phys. Rev. Lett.*, 90:021802, 2003.
- [17] Y. Fukuda et al. Evidence for oscillation of atmospheric neutrinos. *Phys. Rev. Lett.*, 81:1562–1567, 1998.
- [18] K. Abe et al. Evidence for the Appearance of Atmospheric Tau Neutrinos in Super-Kamiokande. *Phys. Rev. Lett.*, 110(18):181802, 2013.
- [19] Augustin et al. Discovery of a Narrow Resonance in e^+e^- Annihilation. *Phys. Rev. Lett.*, 33:1406–1408, Dec 1974.
- [20] Aubert et al. Experimental Observation of a Heavy Particle *J. Phys. Rev. Lett.*, 33:1404–1406, Dec 1974.

-
- [21] S. L. Glashow, J. Iliopoulos, and L. Maiani. Weak Interactions with Lepton-Hadron Symmetry. *Phys. Rev. D*, 2:1285–1292, Oct 1970.
- [22] Makoto Kobayashi and Toshihide Maskawa. CP-Violation in the Renormalizable Theory of Weak Interaction. 49(2):652–657, 1973.
- [23] S. W. Herb et al. Observation of a Dimuon Resonance at 9.5 GeV in 400-GeV Proton-Nucleus Collisions. *Phys. Rev. Lett.*, 39:252–255, Aug 1977.
- [24] M. L. Perl et al. Evidence for Anomalous Lepton Production in $e^+ - e^-$ Annihilation. *Phys. Rev. Lett.*, 35:1489–1492, Dec 1975.
- [25] K. Kodama et al. Observation of tau neutrino interactions. *Phys. Lett.*, B504:218–224, 2001.
- [26] S. Abachi et al. Search for high mass top quark production in $p\bar{p}$ collisions at $\sqrt{s} = 1.8$ TeV. *Phys. Rev. Lett.*, 74:2422–2426, 1995.
- [27] F. Abe et al. Observation of top quark production in $\bar{p}p$ collisions. *Phys. Rev. Lett.*, 74:2626–2631, 1995.
- [28] Georges Aad et al. Observation of a new particle in the search for the Standard Model Higgs boson with the ATLAS detector at the LHC. *Phys. Lett.*, B716:1–29, 2012.
- [29] Serguei Chatrchyan et al. Observation of a new boson at a mass of 125 GeV with the CMS experiment at the LHC. *Phys. Lett.*, B716:30–61, 2012.
- [30] P. A. R. Ade et al. Planck 2013 results. XVI. Cosmological parameters. *Astron. Astrophys.*, 571:A16, 2014.
- [31] Andrei D Sakharov. Violation of CP invariance, C asymmetry, and baryon asymmetry of the universe. *Soviet Physics Uspekhi*, 34(5):392, 1991.

- [32] Fred Jegerlehner. The hierarchy problem of the electroweak Standard Model revisited, 2013.
- [33] Summary plots from the ATLAS Standard Model physics group. https://atlas.web.cern.ch/Atlas/GROUPS/PHYSICS/CombinedSummaryPlots/SM/index.html#ATLAS_e_SMSummary_FiducialRatio. Accessed: 2016-07-07.
- [34] S. Schael et al. Precision electroweak measurements on the Z resonance. *Phys. Rept.*, 427:257–454, 2006.
- [35] Serguei Chatrchyan et al. Combined search for the quarks of a sequential fourth generation. *Phys. Rev.*, D86:112003, 2012.
- [36] Georges Aad et al. Constraints on non-Standard Model Higgs boson interactions in an effective Lagrangian using differential cross sections measured in the $H \rightarrow \gamma\gamma$ decay channel at $\sqrt{s} = 8\text{TeV}$ with the ATLAS detector. *Phys. Lett.*, B753:69–85, 2016.
- [37] Mathieu Buchkremer, Jean-Marc Gerard, and Fabio Maltoni. Closing in on a perturbative fourth generation. *JHEP*, 06:135, 2012.
- [38] Abdelhak Djouadi and Alexander Lenz. Sealing the fate of a fourth generation of fermions. *Phys. Lett.*, B715:310–314, 2012.
- [39] Otto Eberhardt, Geoffrey Herbert, Heiko Lacker, Alexander Lenz, Andreas Menzel, Ulrich Nierste, and Martin Wiebusch. Impact of a Higgs boson at a mass of 126 GeV on the standard model with three and four fermion generations. *Phys. Rev. Lett.*, 109:241802, 2012.
- [40] Kaustubh Agashe, Roberto Contino, and Alex Pomarol. The Minimal composite Higgs model. *Nucl. Phys.*, B719:165–187, 2005.
- [41] David B. Kaplan, Howard Georgi, and Savas Dimopoulos. Composite higgs scalars. *Physics Letters B*, 136(3):187 – 190, 1984.

- [42] N. Arkani-Hamed, A. G. Cohen, E. Katz, and A. E. Nelson. The Littlest Higgs. *JHEP*, 07:034, 2002.
- [43] Martin Schmaltz and David Tucker-Smith. Little Higgs review. *Ann. Rev. Nucl. Part. Sci.*, 55:229–270, 2005.
- [44] F. del Aguila, L1. Ametller, G.L. Kane, and J. Vidal. Vector-like fermion and standard higgs production at hadron colliders. *Nuclear Physics B*, 334(1):1 – 23, 1990.
- [45] F. del Aguila, M. Perez-Victoria, and Jose Santiago. Effective description of quark mixing. *Phys. Lett.*, B492:98–106, 2000.
- [46] F. Del Aguila and M.J. Bowick. The possibility of new fermions with $\hat{I} = 0$ mass. *Nuclear Physics B*, 224(1):107 – 136, 1983.
- [47] J. A. Aguilar-Saavedra, R. Benbrik, S. Heinemeyer, and M. Pérez-Victoria. Handbook of vectorlike quarks: Mixing and single production. *Phys. Rev.*, D88(9):094010, 2013.
- [48] Georges Aad et al. Search for pair and single production of new heavy quarks that decay to a Z boson and a third-generation quark in pp collisions at $\sqrt{s} = 8$ TeV with the ATLAS detector. *JHEP*, 11:104, 2014.
- [49] J. A. Aguilar-Saavedra. Identifying top partners at LHC. *JHEP*, 11:030, 2009.
- [50] Search for production of vector-like top quark pairs and of four top quarks in the lepton-plus-jets final state in pp collisions at $\sqrt{s} = 13$ TeV with the ATLAS detector. Technical Report ATLAS-CONF-2016-013, CERN, Geneva, Mar 2016.
- [51] Search for pair production of vector-like T quarks in the lepton plus jets final state. Technical Report CMS-PAS-B2G-16-002, CERN, Geneva, 2016.

-
- [52] Georges Aad et al. Search for vectorlike B quarks in events with one isolated lepton, missing transverse momentum, and jets at $\sqrt{s} = 8$ TeV with the ATLAS detector. *Phys. Rev. D*, 91:112011, Jun 2015.
- [53] Georges Aad et al. Analysis of events with b -jets and a pair of leptons of the same charge in pp collisions at $\sqrt{s} = 8$ TeV with the ATLAS detector. *JHEP*, 10:150, 2015.
- [54] Georges Aad et al. Search for production of vector-like quark pairs and of four top quarks in the lepton-plus-jets final state in pp collisions at $\sqrt{s} = 8$ TeV with the ATLAS detector. *JHEP*, 08:105, 2015.
- [55] Juan Pedro Araque Espinosa. *Search for heavy fermions with the ATLAS experiment at the LHC collider*. PhD thesis, Minho U., Oct 2015. Presented 20 Apr 2016.
- [56] Juan Pedro Araque, Nuno Filipe Castro, and Jose Santiago. Interpretation of Vector-like Quark Searches: Heavy Gluons in Composite Higgs Models. Technical Report arXiv:1507.05628, Jul 2015.
- [57] Merve Sahinsoy. Searches for vector-like quarks with the ATLAS detector at the LHC. Aug 2015.
- [58] CMS Collaboration. Search for Single Production of a Vector Like T Quark Decaying to a Higgs Boson and a Leptonically Decaying Top Quark. 2016.
- [59] Search for single production of vector-like quarks decaying into final states with a Z boson and a top or a bottom quark. Technical Report CMS-PAS-B2G-16-001, CERN, Geneva, 2016.
- [60] Georges Aad et al. Search for single production of vector-like quarks decaying into Wb in pp collisions at $\sqrt{s} = 8$ TeV with the ATLAS detector. 2016.

-
- [61] Lyndon Evans and Philip Bryant. LHC Machine. *Journal of Instrumentation*, 3(08):S08001, 2008.
- [62] V Baglin, G Bregliozzi, J M Jimenez, and G Lanza. Synchrotron Radiation in the LHC Vacuum System. (CERN-ATS-2011-245), Dec 2011.
- [63] The ALICE Collaboration. The ALICE experiment at the CERN LHC. *Journal of Instrumentation*, 3(08):S08002, 2008.
- [64] The LHCb Collaboration. The LHCb Detector at the LHC. *Journal of Instrumentation*, 3(08):S08005, 2008.
- [65] G. Aad et al. The ATLAS Experiment at the CERN Large Hadron Collider. *JINST*, 3:S08003, 2008.
- [66] The CMS Collaboration. The CMS experiment at the CERN LHC. *Journal of Instrumentation*, 3(08):S08004, 2008.
- [67] Cinzia De Melis. The CERN accelerator complex. Complexe des accélérateurs du CERN. Jan 2016. General Photo.
- [68] Laura Barranco Navarro. Alignment of the ATLAS Inner Detector in the LHC Run II. Technical Report ATL-PHYS-PROC-2015-190, CERN, Geneva, Dec 2015.
- [69] João Pequenão. Computer Generated image of the ATLAS calorimeter. <https://cds.cern.ch/record/1095927>. Accessed: 2016-07-07.
- [70] João Pequenão. Computer generated image of the ATLAS Muons subsystem. <https://cds.cern.ch/record/1095929>. Accessed: 2016-07-07.
- [71] ATLAS first level trigger: Technical design report. 1998.
- [72] Peter Jenni, Marzio Nessi, Markus Nordberg, and Kenway Smith. *ATLAS high-level trigger, data-acquisition and controls: Technical Design Report*. Technical Design Report ATLAS. CERN, Geneva, 2003.

- [73] https://twiki.cern.ch/twiki/bin/view/AtlasPublic/LuminosityPublicResultsRun2#Luminosity_summary_plots_for_AN1. [Accessed: 07-07-2016].
- [74] Protos - program for top simulations. <http://jaguilar.web.cern.ch/jaguilar/protos/>. Accessed: 2016-07-07.
- [75] Torbjorn Sjostrand, Stephen Mrenna, and Peter Z. Skands. PYTHIA 6.4 Physics and Manual. *JHEP*, 05:026, 2006.
- [76] S. Agostinelli et al. Geant4 simulation toolkit. *Nuclear Instruments and Methods in Physics Research Section A: Accelerators, Spectrometers, Detectors and Associated Equipment*, 506(3):250 – 303, 2003.
- [77] T. Gleisberg, Stefan. Hoeche, F. Krauss, M. Schonherr, S. Schumann, F. Siegert, and J. Winter. Event generation with SHERPA 1.1. *JHEP*, 02:007, 2009.
- [78] Stefano Frixione, Paolo Nason, and Carlo Oleari. Matching NLO QCD computations with parton shower simulations: the POWHEG method. *Journal of High Energy Physics*, 2007(11):070, 2007.
- [79] Johan Alwall, Michel Herquet, Fabio Maltoni, Olivier Mattelaer, and Tim Stelzer. MadGraph 5 : Going Beyond. *JHEP*, 06:128, 2011.
- [80] Matteo Cacciari, Gavin P. Salam, and Gregory Soyez. The Anti-k(t) jet clustering algorithm. *JHEP*, 04:063, 2008.
- [81] Valerio Dao et al. Expected performance of the ATLAS b -tagging algorithms in Run-2. Technical Report ATL-PHYS-PUB-2015-022, CERN, Geneva, Jul 2015.
- [82] W Lampl, S Laplace, D Lelas, P Loch, H Ma, S Menke, S Rajagopalan, D Rousseau, S Snyder, and G Unal. Calorimeter Clustering Algorithms: Description and Performance. Technical Report ATL-LARG-PUB-2008-002. ATL-COM-LARG-2008-003, CERN, Geneva, Apr 2008.

-
- [83] Electron efficiency measurements with the ATLAS detector using the 2015 LHC proton-proton collision data. (ATLAS-CONF-2016-024), Jun 2016.
- [84] Muon reconstruction performance of the ATLAS detector in proton-proton collision data at 13 TeV. *Eur. Phys. J. C*, 76(arXiv:1603.05598. CERN-EP-2016-033):292, Mar 2016.
- [85] Kyle Cranmer, George Lewis, Lorenzo Moneta, Akira Shibata, and Wouter Verkerke. HistFactory: A tool for creating statistical models for use with RooFit and RooStats. Technical Report CERN-OPEN-2012-016, New York U., New York, Jan 2012.
- [86] Estimation of non-prompt and fake lepton backgrounds in final states with top quarks produced in proton-proton collisions at $\sqrt{s}=8$ TeV with the ATLAS detector. Technical Report ATLAS-CONF-2014-058, CERN, Geneva, Oct 2014.
- [87] Thomas Junk. Confidence level computation for combining searches with small statistics. *Nucl. Instrum. Meth.*, A434:435–443, 1999.
- [88] Alexander L. Read. Presentation of search results: The CL(s) technique. *J. Phys.*, G28:2693–2704, 2002. [11(2002)].
- [89] <https://twiki.cern.ch/twiki/bin/view/AtlasPublic/LuminosityPublicResultsRun2>. [Accessed: 20-07-2016].